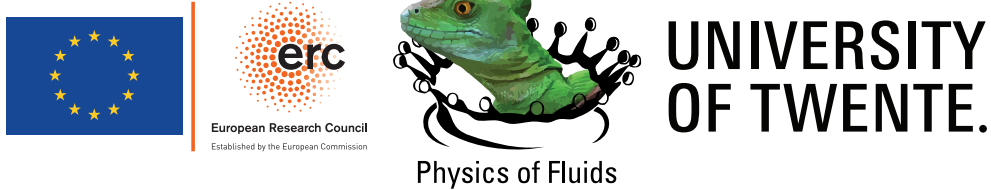


# Viscous Free-Surface Flows

Vatsal Sanjay

## **Graduation committee members:**

Prof. Dr. Jennifer L. Herek (chairperson)	University of Twente
Prof. Dr. rer. nat. Dr. h. c. Detlef Lohse (promotor)	University of Twente
Prof. Dr. David Quéré	ESPCI & Ladhyyx
Prof. Dr. Ir. E. Harald van Brummelen Eindhoven	University of Technology
Prof. Dr. Ir. Wilko Rohlfs	University of Twente
Prof. Dr. Marjolein van der Linden	University of Twente
Assist. Prof. Dr. Maziyar Jalaal	University of Amsterdam



The work in this thesis was carried out at the Physics of Fluids group of the Faculty of Science and Technology of the University of Twente. This thesis was financially supported by the ERC Advanced Grant No. 740479-DDD.

Dutch title:

*Viskeuze Stromingen bij Vrije-Oppervlakken*

Publisher:

Vatsal Sanjay, Physics of Fluids, University of Twente,  
P.O. Box 217, 7500 AE Enschede, The Netherlands

<https://www.vatsalsanjay.com>

Printed by: Gildeprint

Copyright © 2022 Vatsal Sanjay. All rights reserved.

No part of this work may be reproduced or transmitted for commercial purposes, in any form or by any means, electronic or mechanical, including photocopying and recording, or by any information storage or retrieval system, except as expressly permitted by the author.

ISBN: 978-90-365-5407-7

DOI: 10.3990/1.9789036554077

# VISCOUS FREE-SURFACE FLOWS

## DISSERTATION

to obtain  
the degree of doctor at the Universiteit Twente,  
on the authority of the rector magnificus,  
prof. dr. ir. A. Veldkamp,  
on account of the decision of the Doctorate Board,  
to be publicly defended  
on Friday the 15th of July 2022 at 12:45

by

Vatsal Sanjay  
Born on the 5th of February 1996  
in RS Tank Laheriasarai, Bihar, India

This dissertation has been approved by the promotor:

Prof. Dr. rer. nat. Dr. h. c. Detlef Lohse

To Anjali,  
the one constant of my life.



Scan me for a soft copy of  
this Ph.D. thesis

# Contents

<b>Introduction</b>	<b>1</b>
<b>I Drop Impact</b>	<b>15</b>
<b>1 Impact forces of water drops falling on superhydrophobic surfaces</b>	<b>17</b>
1.1 Introduction . . . . .	18
1.2 Setup . . . . .	19
1.3 Formation of a second peak in the force . . . . .	21
1.4 Weber number dependence of the characteristics times . . . . .	23
1.5 Influence of Weber number on the first peak . . . . .	23
1.6 Influence of Weber number on the second peak . . . . .	25
1.7 Conclusions and outlook . . . . .	27
<b>Appendices</b>	<b>29</b>
1.A Experimental method . . . . .	29
1.B Numerical method . . . . .	31
1.C Superhydrophobic vs. hydrophilic surfaces . . . . .	36
1.D Some notes on the different regimes of drop impact . . . . .	38
1.E Calculation of the jet and retraction characteristics . . . . .	46
1.F Code availability . . . . .	52
1.G Supplemental movies . . . . .	52
<b>2 When does a drop stop bouncing?</b>	<b>55</b>
2.1 Introduction . . . . .	56
2.2 Governing equations . . . . .	57
2.3 Bouncing inhibition . . . . .	59

2.4 Limiting cases . . . . .	64
2.5 Conclusions and outlook . . . . .	74
<b>Appendices</b>	<b>77</b>
2.A Measuring the restitution coefficient . . . . .	77
2.B Influence of Weber number . . . . .	77
2.C Code availability . . . . .	79
2.D Supplemental movies . . . . .	80
<b>3 Drop impact on viscous liquid films</b>	<b>81</b>
3.1 Introduction . . . . .	82
3.2 Methods . . . . .	84
3.3 Phenomenology . . . . .	87
3.4 Phenomenological model . . . . .	92
3.5 Influence of drop and film parameters . . . . .	95
3.6 Bouncing inhibition on low Ohnesorge number films . . . . .	100
3.7 Conclusions and outlook . . . . .	104
<b>Appendices</b>	<b>109</b>
3.A Air layer rupture . . . . .	109
3.B Substrate independent bouncing . . . . .	109
3.C Influence of the impact Weber number on bouncing drops . . . . .	114
3.D Measuring film thickness . . . . .	114
3.E Measuring the restitution coefficient . . . . .	115
3.F Code availability . . . . .	115
3.G Supplemental movies . . . . .	115
<b>4 Lifting a sessile oil drop with an impacting one</b>	<b>117</b>
4.1 Introduction . . . . .	118
4.2 Method . . . . .	120
4.3 Experimental observations . . . . .	122
4.4 Direct numerical simulations . . . . .	126
4.5 Conclusions and outlook . . . . .	133
<b>Appendices</b>	<b>135</b>
4.A Contact angle measurements . . . . .	135
4.B Water-on-water drop impact . . . . .	135
4.C Simulation methodology . . . . .	137
4.D Energy budget calculations . . . . .	139

4.E Code availability . . . . .	140
4.F Supplemental movies . . . . .	140



# Introduction

Liquids rule our lives in more ways than usually perceived. In one of his popular-science books, [? ] delineates the fickle nature of the life-sustaining, delightful, and yet at times, potentially dangerous fluid flow processes. To cite a few examples, the blood flow in our body sustains life, whereas nitroglycerin-based explosives hold the inherent amplitude to cause severe damage. Nonetheless, aesthetically pleasing waterfalls are a relief to sore eyes for everyone. What is even more intriguing is how many of the examples discussed in [? ] and our everyday encounter with liquids for cooking, drinking, and cleaning involve flows at the interface between two fluids, one of which offers negligible tangential shear stress. Such flows are categorized as free-surface flows [? ] and are the subject of this thesis.

From the atomization chamber that fuels an aircraft to the Moka pot that fueled the author while finishing this thesis, all involve intricate free-surface flows. Such processes often span over multi-scales, for example, from slamming of ocean waves onto ships and sloshing of liquid cargo to that of coffee or tea in a cup [? ], and can involve multi-physics from self-propelled drops on a superheated surface (the so-called Leidenfrost drops, [? ? ? ]) to disintegration of liquids in strong electric fields (for example, electrospray from Taylor cones, [? ? ]). Yet another example of free-surface flows involves a glass of wine where a liquid film climbs along the wall, evaporates, and drips tiny droplets (known as “tears” of wine owing to the Marangoni stresses, [? ? ]). It is, therefore, safe to claim that free-surface flows are omnipresent.

This thesis elucidates two classes of the above-mentioned free-surface phenomena, namely, the impact of liquid drops on non-wetting substrates (part I) and capillary driven retraction and bursting of films and free-surface bubbles, respectively (part ??). In all the cases, we pay special attention to viscous stresses and how they dictate the fate of such free-surface flows.

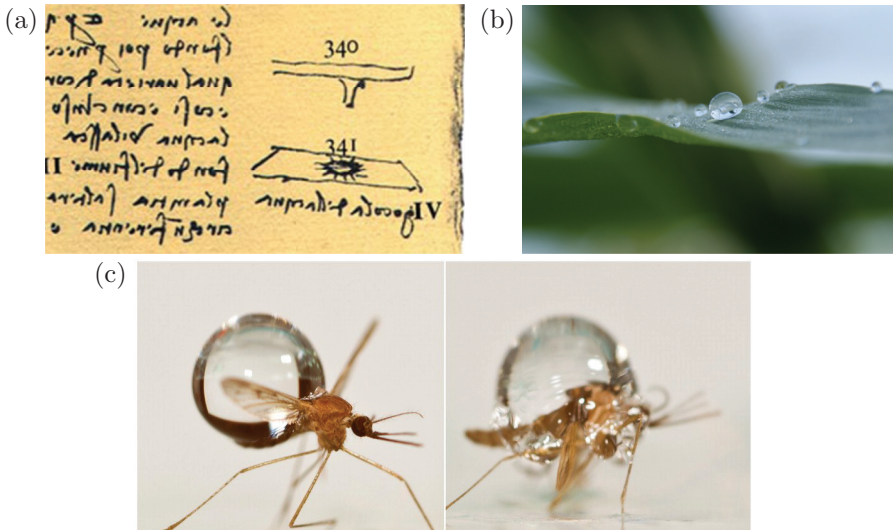


Figure 1: (a) Sketch of a water drop falling on a rigid immobile substrate by [? ]. (b) A drop of dew sitting on a non-wetting leaf, nature’s way of keeping flora dry (adapted with permission from [? ]). (c) A water drop impacting a mosquito [? ].

## Part I: Drop Impact

It is fascinating to watch raindrops hitting a solid surface [? ? ]. This phenomenon has piqued the interest of scientists for over five centuries, ever since Leonardo da Vinci sketched a water drop impacting a rigid immobile substrate (see figure 1a, reproduced from the margin of folio 33r in Codex Hammer/Leicester (1506 – 1510), [? ]), who also noted the axisymmetry of drop impact and rebound. However, it was only in 1876-77 (still over one-and-a-half century ago) when Arthur Mason Worthington [? ? ] published the first photographs of the drop impact process, stimulating artists, scientists, and engineers alike ever since. Indeed, drop impact processes are not only interesting from a point of view of fundamental research but also find relevance in inkjet printing [? ], cooling applications [? ? ? ], pesticides application [? ? ], and criminal forensics [? ].

Upon impact [? ], the liquid first spreads [? ? ] until it reaches its maximal extent [? ? ? ? ]. For a perfectly wetting substrate, for example, glass or paper [? ], the drop sticks to it. However, for a non-wetting substrate, for example, plant leaves (see figure 1b, [? ? ? ]), the drops can ricochet off following rich dynamics: from the maximum spreading extent, it recoils,

following a capillary-driven Taylor-Culick type retraction parallel to the substrate to minimize its surface energy [? ? ? ? ? ? ], and ultimately bounces off in an elongated shape perpendicular to the substrate [? ? ? ]. Following the first observations by [? ? ], these elongated shapes are called Worthington jets, and are formed by the flow-focusing due to capillary waves [? ? ] and drop retraction [? ].

Such drop impact and bouncing behavior abound in nature as non-wetting surfaces provide plants and animals with a natural way to keep dry [? ? ? ]. Such rebound behaviors are also important in various industrial processes [? ] such as self-cleaning [? ], keeping clothes dry [? ], and anti-fogging surfaces [? ]. However, the repellent behavior of these non-wetting substrates is volatile and can fail due to external disturbances such as pressure [? ? ? ? ], evaporation [? ? ? ], mechanical vibration [? ], or the impact forces of prior droplets [? ]. Hence, for most of these applications, the drop impact forces can lead to severe unwanted consequences, such as soil erosion [? ] or the damage to engineered surfaces [? ? ? ]. A thorough understanding of the drop impact forces is thus needed to develop countermeasures against these damages [? ]. Consequently, it is natural to ask how much force the substrate (plant leaves or insects) experiences during such impact and takeoff events (see figure 1c, [? ? ] and chapter 1).

In most of the applications mentioned above, such as self-cleaning [? ] and anti-fogging [? ], it is pertinent that the drops bounce off the surface. On the other hand, bouncing must be suppressed for various other applications, such as inkjet printing [? ] or pesticide deposition [? ? ? ]. Therefore, one often wonders when will a drop stop bouncing? We will answer this question in chapter 2 by studying the role of viscosity and gravity on bouncing inhibition of impacting drops. Furthermore, in chapter 3, we extend this work to cases where the substrate is coated with a viscous oil film and an air layer is trapped between it and the impacting drop, delaying their contact.

In fact, in 1881, [? ] noticed a delay in coalescence between an impacting drop and a pool of the same liquid, owing to an air layer between them. Interfacial processes such as Marangoni flow [? ], Leidenfrost effect [? ? ? ? ? ? ], inverse Leidenfrost effect [? ? ? ], or electromagnetic forces [? ? ] can further stabilize the sandwiched air/vapor layer to facilitate levitation. Moreover, even drops impacting on rigid substrates encounter such air layers that can delay coalescence [? ]. In 2012, [? ] used direct interferometry measurements to quantify these air-layers [also see [? ? ? ? ]].

Furthermore, they also facilitate superamphiphobic-like bouncing [? ]. We

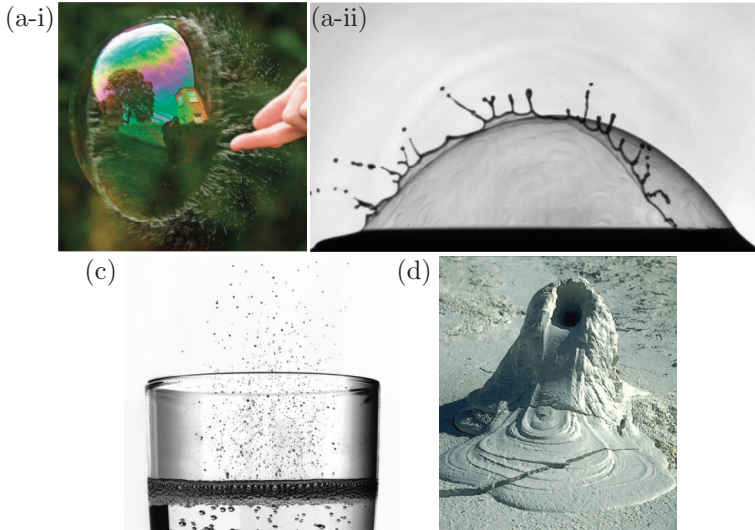


Figure 2: (a-i) Playing with soap bubbles (reprinted with permission from [?]) as a pierced soap bubble shrinks (and vanishes) to minimize its surface area and (a-ii) a controlled experiment of the same process [?]. (b) Bubbles bursting at the free-surface of champagne [?]. (c) A mud volcano (reprinted with permission from [?]).

also address such behaviors in chapter 3. A further extension of bouncing off viscous liquid films is the collision between an impacting drop and a sessile one sitting on a non-wetting substrate. A better understanding of such impacts is crucial in the emerging field of additive manufacturing. For example, in 3D printing, which is one of the widely used additive manufacturing techniques, the relative precision of the drop deposition and its shape evolution may decide the success or failure of a printed device. Although it has been shown that the collision of two freely flying droplets offers much richer dynamics than the impact of a single drop [? ?], the collision between an impacting drop and a sessile one is still not well explored. So, in chapter 4, we demystify such collision scenarios.

## Part ??: Retraction & Bursting

Ever since the seminal works of [? ? ?], fluid dynamicists have been intrigued by liquid films, sheets, and soap bubbles for over two centuries. It is particularly bewitching to watch these sheets shrink and vanish to minimize their surface area once a hole nucleates on them (see figure 2a; also notice the

liquid filaments that rapidly break up to generate a myriad of tiny droplets.). Consequently, such bursting of liquid (e.g., soap) films in the air is perhaps the most widely studied example of sheet destabilization and retraction – an area of active research since the pioneering works of [? ? ? ], [? ? ? ] in the late nineteenth and mid-twentieth century to the more recent investigations of [? ? ? ? ? ].

Such retraction processes involve the release of excess surface energy as the interfacial area of the film decreases. Indeed, [? ? ] wrongly assumed that the ‘entire’ surface energy released during such retractions manifests as the kinetic energy of the film [? ] and calculated a retraction velocity that was off by a factor of  $\sqrt{2}$  when compared to the experiments, leading to the famous Dupré-Rayleigh paradox [? ]. [? ] circumvented this paradox by using force/momentum balance to calculate the retraction velocity, which agreed with experiments. However, it was only when [? ] realized that the missing link was viscous dissipation that the paradox was solved [? ]. The correct energy balance requires that the rate of surface energy released should be distributed equally into an increase in kinetic energy of the rim and the viscous dissipation inside the film. Consequently, such retractions are now referred to as Taylor-Culick retractions. More recently, [? ? ? ] have further enhanced the understanding of the role of internal viscous stresses in such retraction processes. In chapter ??, we focus on the role of external viscous stresses on the retraction of liquid films.

Common realizations of Taylor-Culick retractions include bursting of bubbles at a liquid-gas free-surface (figure 2a-ii, [? ]). Once the liquid film separating the gas bubble from the gaseous surrounding disappears, an open cavity is formed [? ] whose collapse leads to a series of rich dynamical processes that involve flow-focusing owing to capillary waves [? ? ] and may lead to the formation of a Worthington jet [? ]. Perfect flow-focusing can also result in an ultra-thin and fast singular jet. Such free-surface bubble bursting is seen in a glass of champagne or other sparkling wine (figure 3c) and is often credited for enhancing the mouthfeel of the taster [? ? ? ? ].

For Newtonian liquids like champagne (figure 2b), [? ? ? ? ] have extensively studied the bursting bubble process, resulting in a profound understanding of the physics of bubble bursting in Newtonian fluids. Surprisingly, very little is known about some other common realizations of bursting bubbles: in geophysics, for example, bubbles bursting at the free surface of mud volcanoes (figure 2c) and in the food industry, where the rheological properties of the medium influence the collapse of bubble cavities. These materials behave

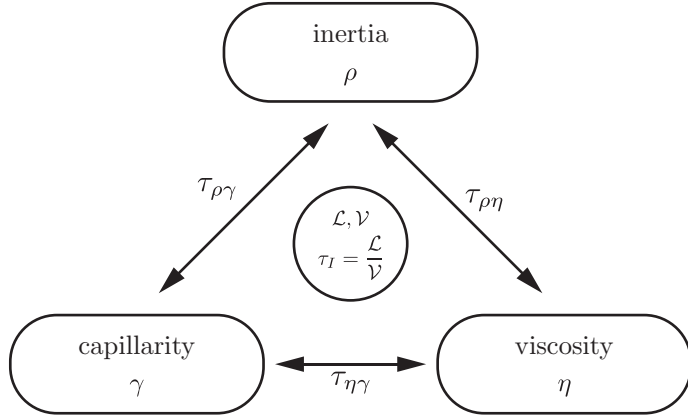


Figure 3: Important scales for viscous free-surface flows. Here,  $\mathcal{V}$  and  $\mathcal{L}$  are the relevant velocity and length scales associated with the flow, whereas  $\rho$ ,  $\gamma$ , and  $\eta$  are the material properties of the fluid, namely, density, surface tension coefficient, and viscosity, respectively.  $\tau_{ij}$  denote several timescales, which are used throughout this thesis: the inertial timescale,  $\tau_I = \mathcal{L}/\mathcal{V}$ , inertio-capillary timescale,  $\tau_{\rho\gamma} = \sqrt{\rho\mathcal{L}^3/\gamma}$ , inertio-viscous timescale,  $\tau_{\rho\eta} = \rho\mathcal{L}^2/\eta$ , and the visco-capillary time scale,  $\tau_{\eta\gamma} = \eta\mathcal{L}/\gamma$ .

more like an elastic solid below critical stress (yield stress); however, they flow above this critical stress. Readers can find detailed reviews on yield stress fluids in [? ? ? ? ]. In such cases, the viscous stresses are enhanced by this non-zero yield stress enabling the free surface to sustain finite deformations. In chapter ??, we elucidate the physics of a bursting bubble in a viscoplastic medium by analyzing the role of yield stress on the free-surface phenomenon of the collapse of a bubble cavity driven by capillarity to approach minimum surface area configuration.

## Relevant timescales and dimensionless numbers

Ever since the pioneering ideas of [? ? ], fluid dynamicists highly value dimensionless numbers as they give a convenient way to express the control and output parameters of a process. It is common to express these numbers as ratios of different force, time, or length scales [? ]. Figure 3 illustrates the relevant forces (inertia, capillarity, and viscosity) that we will discuss throughout this thesis and the associated timescales: visco-capillary ( $\tau_{\eta\gamma}$ ), inertio-capillary ( $\tau_{\rho\gamma}$ ), inertio-viscous ( $\tau_{\rho\eta}$ ), and inertial ( $\tau_I$ ), defined as

$$\tau_{\eta\gamma} = \frac{\eta\mathcal{L}}{\gamma}, \quad \tau_{\rho\gamma} = \sqrt{\frac{\rho\mathcal{L}^3}{\gamma}}, \quad \tau_{\rho\eta} = \frac{\rho\mathcal{L}^2}{\eta}, \quad \tau_I = \frac{\mathcal{L}}{V}. \quad (1)$$

Here,  $V$  and  $\mathcal{L}$  are the relevant velocity and length scales associated with the flow, whereas  $\rho$ ,  $\gamma$ , and  $\eta$  are the material properties of the fluid, namely, density, surface tension coefficient, and viscosity, respectively. The visco-capillary timescale ( $\tau_{\eta\gamma}$ ) is associated with capillary driving and viscous resistance, for example, thinning of a viscous liquid thread [? ]. The inertio-capillary timescale ( $\tau_{\rho\gamma}$ ) measures the duration of processes driven by capillary and resisted by inertia, for example, it is the Rayleigh timescale for the breakup of an inviscid fluid jet or that of capillary oscillations of a freely suspended liquid drop [? ]. Furthermore, the inertio-viscous timescale ( $\tau_{\rho\eta}$ ) estimates the duration of processes involving inertia and viscous stresses, for example, the development of boundary layers during drop impact [? ]. Lastly, the inertial timescale ( $\tau_I$ ) is associated with flows involving only inertia, for example, inertial shock that follows the impact of an inviscid drop [? ].

Using the above-mentioned timescales, we define several dimensionless numbers and use them throughout this thesis. The square of the ratio of the inertio-capillary to inertial timescales gives the Weber number (chapters 1–??),

$$We = \left( \frac{\tau_{\rho\gamma}}{\tau_I} \right)^2 = \frac{\rho V^2 \mathcal{L}}{\gamma}, \quad (2)$$

that compares the inertia and capillary stresses. Furthermore, the ratio of inertio-viscous to inertial timescale defines the Reynolds number,

$$Re = \frac{\tau_{\rho\eta}}{\tau_I} = \frac{\rho V \mathcal{L}}{\eta}, \quad (3)$$

that compares the inertial and viscous stresses. Moreover, taking the ratio of visco-capillary and inertial timescales gives the capillary number (chapter ??),

$$Ca = \frac{\tau_{\eta\gamma}}{\tau_I} = \frac{\eta V}{\gamma}. \quad (4)$$

Next, we can also take the ratios of the compound timescales (inertio-capillary to inertio-viscous or visco-capillary to inertio-capillary) to define the Ohnesorge number (used in all chapters),

$$Oh = \frac{\tau_{\rho\gamma}}{\tau_{\rho\eta}} = \frac{\tau_{\eta\gamma}}{\tau_{\rho\gamma}} = \frac{\eta}{\sqrt{\rho\gamma\mathcal{L}}}, \quad (5)$$

named after the German fluid dynamicist, Wolfgang von Ohnesorge. We refer the readers to [? ] to learn more about this less-known “numberman” of fluid dynamics. The Ohnesorge number requires special mention because it entails a convenient way of involving all the three relevant forces (inertia, capillary, and viscous) in any free-surface fluid dynamics problem (see figure 3). Furthermore, we use it as a proxy to estimate the importance of viscous dissipation throughout this thesis. Indeed, in all the capillary-driven processes (drop oscillation, retraction, and take-off in chapters 1–4, and rupture and bursting in chapters ??–??), a large Ohnesorge number ( $Oh \gg 1$ ) implies dominance of viscous stresses.

It is also common to use the Laplace number,  $La$ , defined as

$$La = \frac{\rho\gamma\mathcal{L}}{\eta^2} = \frac{1}{Oh^2} \quad (6)$$

which is conceptually similar to the Ohnesorge number [? ].

Of course, introducing forces other than the ones mentioned in figure 3 will add more dimensionless numbers to the list mentioned above. For example, the Bond number (chapter 2), given by,

$$Bo = \frac{\rho g \mathcal{L}^2}{\gamma} \quad (7)$$

compares gravity to the capillary forces, where  $g$  is the acceleration due to gravity. Furthermore, yield stress ( $\sigma_y$ ) of viscoplastic fluids is often characterized using the plastocapillary number (chapter ??), defined as,

$$\mathcal{J} = \frac{\sigma_y \mathcal{L}}{\gamma} \quad (8)$$

that compares the yield and capillary stresses.

Lastly, geometric features and constraints can also enrich the number of dimensionless numbers. For example, for the case of binary drop impact [? ], the offset  $d$  between the two droplets can be non-dimensionalized using the relevant length scale (for example, drop's radius), giving the dimensionless offset parameter as (chapter 4)

$$\chi = \frac{d}{\mathcal{L}}. \quad (9)$$

Another example can be found for the case of drop impact on liquid films (chapter 3 and ? ]) where the dimensionless film thickness can be given as

$$\Gamma = \frac{h_f}{\mathcal{L}}, \quad (10)$$

where  $h_f$  is the thickness of the film.

We can use the dimensionless numbers described above to illustrate the region of interest in different fluid dynamics processes. Figure 4 exemplifies one such operating parameter space for drop-on-demand inkjet printing in terms of the Ohnesorge number  $Oh$  (that involves only material properties, equation (5)) and Reynolds number  $Re$  (that involves both flow and material properties, equation (3)). Readers are referred to ? ] for a detailed review and the state-of-the-art of inkjet printing process.

## A guide through the thesis

In this thesis, we will investigate the role of viscous stresses on several free-surface processes. Here, we provide a guide through the thesis and the key questions that we ask in each chapter.

In **chapter 1**, we study the normal force profile of water drops (fixed Ohnesorge number  $Oh$ ) impacting superhydrophobic surfaces. We vary  $We$  (equation (2)) and  $Bo$  (equation (7)), see figure 5, to answer the following questions:

### Chapter 1

1. What sets the magnitude of the normal reaction force between the impacting drop and the non-wetting substrate?
2. What sets the timescales associated with the normal reaction force?

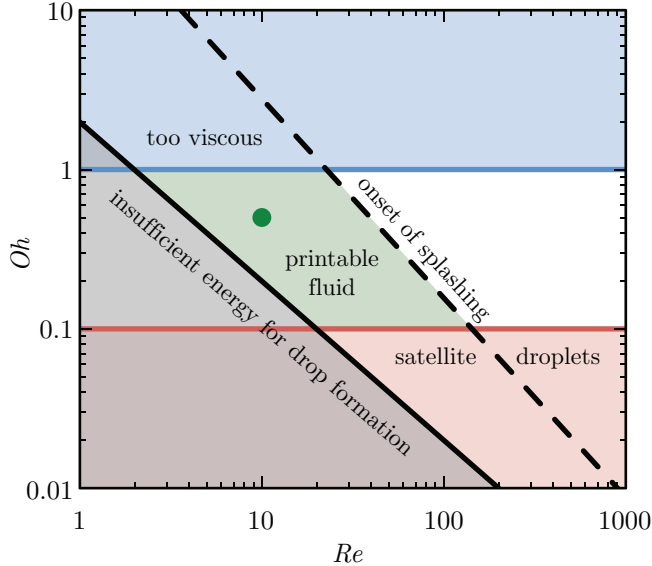


Figure 4: Parameter space in terms of Ohnesorge number  $Oh$  and Reynolds number  $Re$  showing the operating regime for stable drop-on-demand inkjet printing (green shaded area). The green dot corresponds to the material properties of a typical ink under standard operating conditions. The drop needs sufficient kinetic energy to eject out of the nozzle requiring that  $We > 4$  or  $Re \geq 2/Oh$  [? ]. In terms of the material properties of the ink, printing will fail if the ink is too viscous ( $Oh \geq 10$ ) or if satellite drops form ( $Oh \leq 1/10$ ) [? ? ? ]. Lastly, the criterion for the onset of splashing is given by  $OhRe^{5/4} \geq 50$  following the work of [? , also see chapter 1] and further restricts the printable region for inkjet printers. Similar parameter space for inkjet printing is also available in [? ? ? ? ]. This figure is reproduced from [? ] with permission from the author.

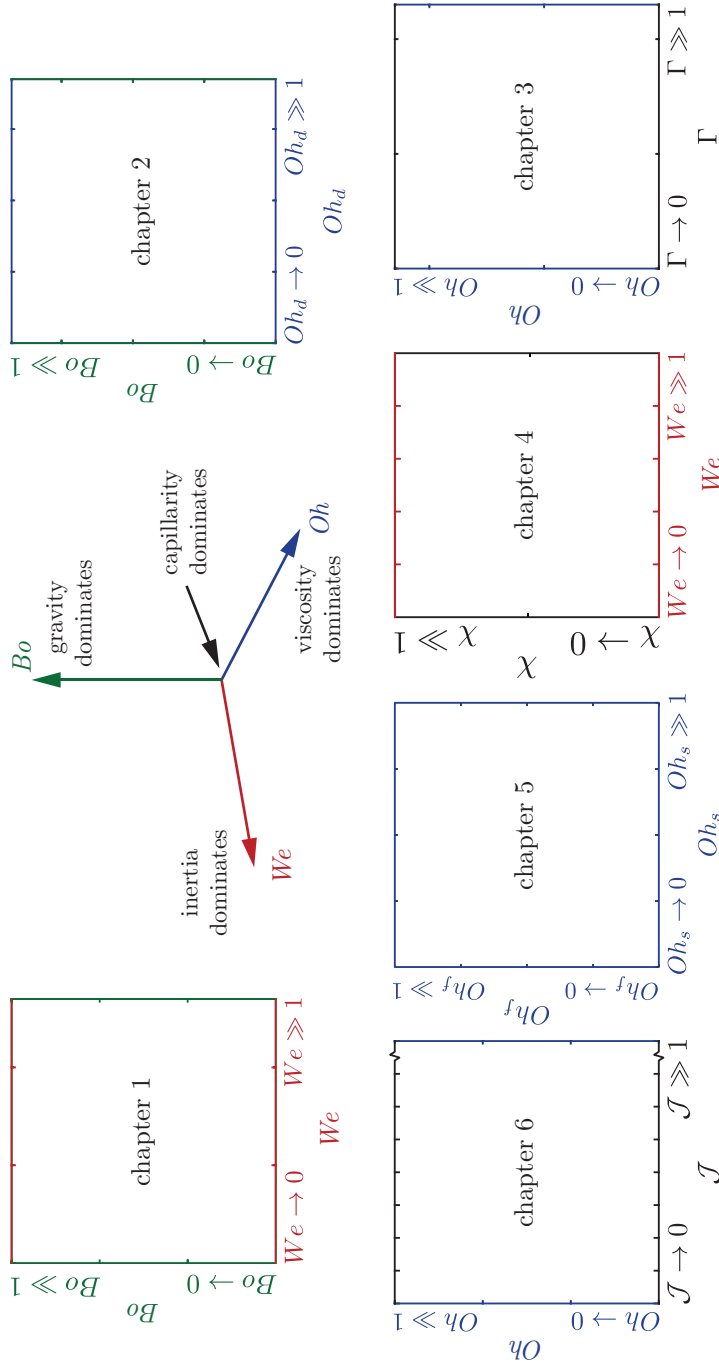


Figure 5: Dimensionless numbers used in the present thesis. The Weber number  $We$  (equation (2)), the Bond number  $Bo$  (equation (7)), and the Ohnesorge number  $Oh$  (equation (5)) are the three central dimensionless numbers that respectively compare inertial, gravity, and viscous and inertial to capillary stresses. In the subsequent chapters, we will keep at least one of these numbers as a control parameter. We also stress that we use the  $Oh$  as a proxy for viscous dissipation throughout the thesis. Additionally, we use the dimensionless film thickness  $\Gamma$  (equation (10)) in chapter 3, dimensionless offset  $\chi$  (equation (9)) between the two drops in chapter 4, and the plasto-capillary number  $\mathcal{J}$  (equation (8)) in chapter ???. In conclusion to this thesis (figure ??), we redraw this figure with the filled-in regime maps for each chapter.

In **chapter 2**, we investigate how viscous stresses and gravity conspire against capillarity to inhibit drop bouncing off non-wetting substrates by varying  $Oh$  (equation (5)) and  $Bo$  (equation (7)), see figure 5. We ask the following questions:

### Chapter 2

1. When does a drop stop bouncing?
2. How does a viscous drop stop bouncing?
3. How does a heavy drop stop bouncing?

In this chapter, we also vary the  $We$  (equation (2)) to study its effect on the bouncing to non-bouncing transition in the  $Bo$ - $Oh$  parameter space.

In **chapter 3**, we investigate drops bouncing off viscous liquid films that mimic atomically smooth substrates. The repellent behavior of such substrates requires the presence of an air layer trapped between it and an impacting drop. This work varies the  $Oh$  (equation (5)) of both the drop and the film and  $\Gamma$  (equation (10)) to answer the following questions (figure 5):

### Chapter 3

1. What happens when a liquid drop bounces off an atomically smooth deformable substrate?
2. How does the presence of a viscous film affect the bouncing inhibition discussed in chapter 2?

In **chapter 4**, we probe how to lift a sessile oil drop with an impacting one. This chapter is a natural extension to chapter 3 where we studied drop impact on flat (zero curvature) films. In this chapter, we study similar impacts on a finite curvature sessile drop at different  $We$  (equation (2)). We also vary the offset  $\chi$  (equation (9)) between the impacting and sessile drops to comprehensively study the drop-on-drop impact process and focus on the following key questions (figure 5):

## Chapter 4

1. What is the energy transfer between the two drops when an impacting drop hits a sessile one?
2. Can a moving-impact drop lift a lazy sessile drop sitting on a non-wetting substrate?

In **chapter ??**, we elucidate the influence of the surroundings on Taylor-Culick retractions by exploring three canonical configurations: the classical Taylor-Culick retractions and the generalized ones, namely those fully submerged in an oil bath, and those occurring at an oil-air interface. We vary the  $Oh$  (equation (5)) associated with both the film and the surroundings (figure 5) and seek answers to the following questions:

## Chapter ??

1. Does the inertia of the surrounding medium matter during capillary driven retraction of liquid films?
2. How does viscous dissipation influence film retraction?
3. Where does the bulk of viscous dissipation occur during the Taylor-Culick retraction of films?

In **chapter ??**, we study how viscoplasticity controls the fate of a bubble bursting at a free surface by varying  $Oh$  (equation (5)) and  $\mathcal{J}$  (equation (8)), see figure 5. The chapter answers the following questions:

## Chapter ??

1. How do viscosity and viscoplasticity influence the capillary-driven bursting of the bubble at a liquid-gas free-surface?
2. Can a liquid-gas free surface sustain non-zero surface energies in the presence of yield stress?

The thesis ends with a conclusion and outlook section where we redraw figure 5 with the filled-in regime maps for each chapter and summarize the answers to all the questions posed above.



# Part I

# Drop Impact



## Chapter 1

# Impact forces of water drops falling on superhydrophobic surfaces<sup>o</sup>

A falling liquid drop, after impact on a rigid substrate, deforms and spreads, owing to the normal reaction force. Subsequently, if the substrate is non-wetting, the drop retracts and then jumps off. As we show here, not only is the impact itself associated with a distinct peak in the temporal evolution of the normal force, but also the jump-off, which was hitherto unknown. We characterize both peaks and elucidate how they relate to the different stages of the drop impact process. The time at which the second peak appears coincides with the formation of a Worthington jet, emerging through flow-focusing. Even low-velocity impacts can lead to a surprisingly high second peak in the normal force, even larger than the first one, namely when the Worthington jet becomes singular due to the collapse of an air cavity in the drop.

---

<sup>o</sup>Submitted as: Bin Zhang, **Vatsal Sanjay**, Songlin Shi, Yinggang Zhao, Cunjing Lv, Xi-Qiao Feng, and Detlef Lohse, *Impact forces of water drops falling on superhydrophobic surfaces*, Phys. Rev. Let. (2022). Experiments are done by Zhang and Lv; simulations by Sanjay; analysis and writing by Zhang, Sanjay, Lv, and Lohse; and supervision by Lv and Lohse. Proofread by everyone.

## 1.1 Introduction

In 1876-77, Arthur Mason Worthington [? ? ] published the first photographs of the drop impact process, stimulating artists and researchers alike for an almost one-and-a-half century. Such drop impacts on solid surfaces are highly relevant from an application point of view, namely in inkjet printing [? ], spray coating [? ], criminal forensics [? ], and many other industrial and natural processes [? ? ? ]. For most of these applications, the drop impact forces, which are the subject of this chapter, can lead to serious unwanted consequences, such as soil erosion [? ] or the damage of engineered surfaces [? ? ? ]. A thorough understanding of the drop impact forces is thus needed to develop countermeasures against these damages [? ]. Consequently, recent studies have analyzed the temporal evolution of these forces [? ? ? ? ? ? ].

These studies were, however, up to now limited to wetting scenarios. Then, not surprisingly, the moment of the drop touch-down [? ? ] manifests itself in a pronounced peak in the temporal evolution of the drop impact force, whereas this force is much smaller during droplet spreading [? ? ]. For the non-wetting case, i.e., for superhydrophobic surfaces, the drop impact dynamics is much richer: then, after reaching its maximal diameter, the drop recoils [? ] and can generate an upward, so-called Worthington jet [? ? ]. Ultimately, the drop can even ricochet off the superhydrophobic surface [? ]. Such spectacular water repellency can occur in nature [? ? ? ], and has various technological applications [? ? ? ? ? ], including on moving substrates [? ], where the droplet dynamics is even richer. This feature of superhydrophobicity however is volatile and can fail due to external disturbance such as pressure [? ? ? ? ], evaporation [? ? ? ], mechanical vibration [? ], or the impact forces of prior droplets [? ].

This chapter extends the studies on drop impact forces to the impact on superhydrophobic surfaces. Our key result is that then, next to the first above-mentioned peak in the drop impact force at drop touch-down, a *second peak* in the drop impact force occurs, which under certain conditions can be even more pronounced than the first peak. The physical origin of the second peak lies in momentum conservation: when at the final phase of droplet recoil, the above-mentioned upward Worthington jet forms, momentum conservation also leads to a downward jet inside the drop [? ? ? ? ]. It manifests itself in the second peak in the temporal evolution of the force on the substrate. Using both experiments and direct numerical simulations (DNS) with the volume-

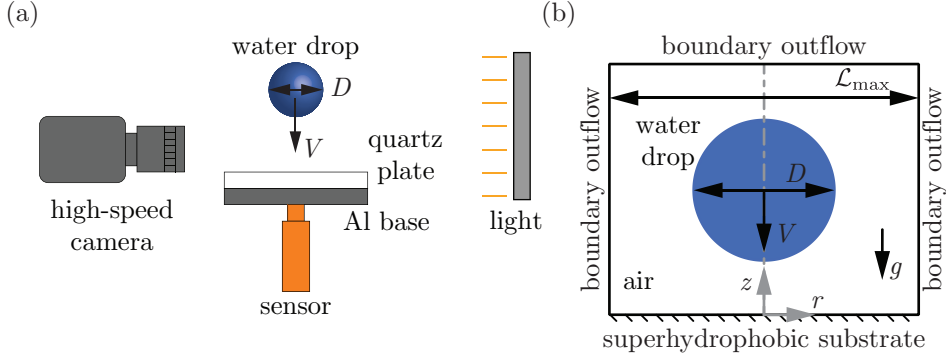


Figure 1.1: (a) Experimental setup: a water drop of diameter  $D$  impacts a superhydrophobic quartz plate at velocity  $V$ . (b) Axi-symmetric simulation domain with the appropriate boundary conditions and relevant material and flow properties. The boundaries are kept far away from the drop to avoid feedback ( $\mathcal{L}_{\max} \gg D$ ).

of-fluid method [? ], we will elucidate the physics of this very rich dynamical process and study its dependence on the control parameters.

This chapter is organized as follow: § 1.2 briefly describes the experimental and numerical setups followed by § 1.3 that correlates the temporal variation of the normal reaction with different stages of the drop impact process. We then elucidate the dependence of Weber number on the characteristic times (§ 1.4) and the two peaks in the transient normal reaction force (§ 1.5 and 1.6). The chapter culminates in conclusions and an outlook in § 1.7.

## 1.2 Setup

The experimental setup is sketched in figure 1.1(a). A water drop impacts a quartz plate whose upper surface is coated with silanized silica nanobeads with diameter of 20 nm (Glaco Mirror Coat Zero; Soft99) [? ? ] to attain superhydrophobicity. We directly measure the impact force  $F(t)$  by synchronizing high-speed photography with fast force sensing (also see § 1.A for details of the experimental setup).

In DNS (figure 1.1b), ideal superhydrophobicity is maintained by assuming that a thin air layer is present between the drop and the substrate [? , also see chapters 2, and 4], and forces are calculated by integrating the pressure field ( $p$ ) at the substrate,

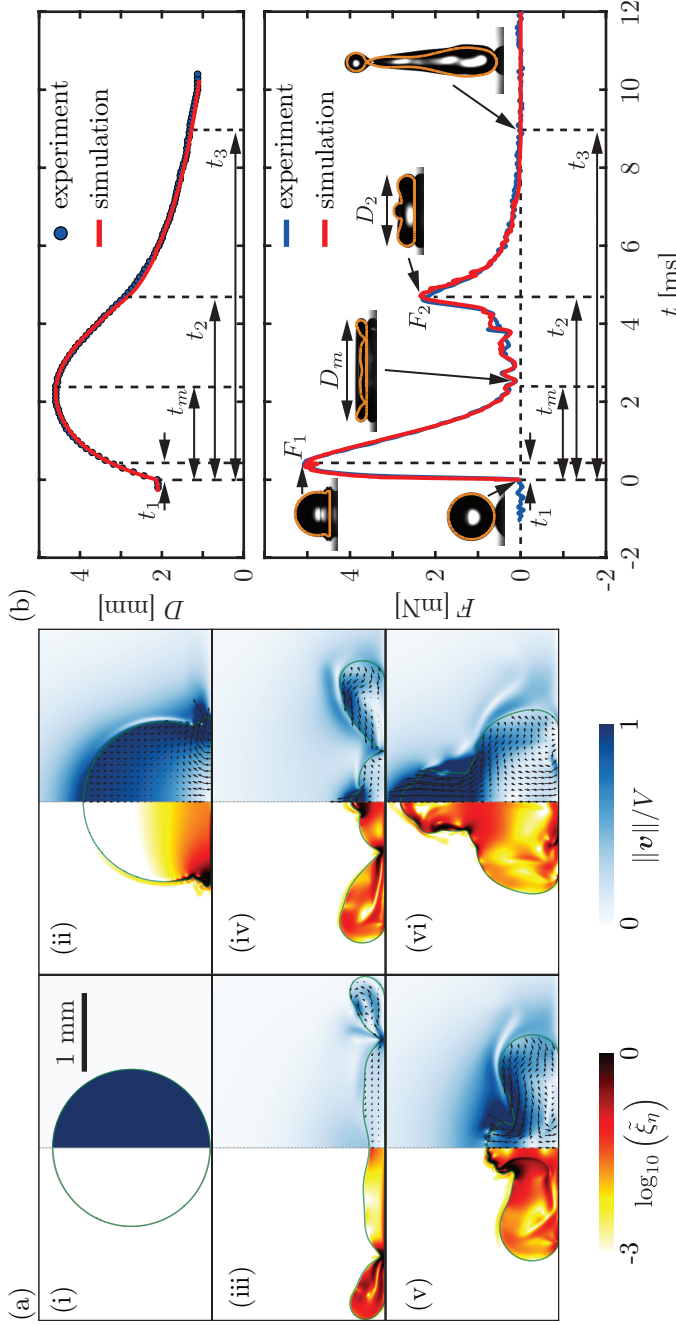


Figure 1.2: (a) Numerical results for a drop impact dynamics for a  $D = 2.05$  mm diameter water drop falling at a speed of  $V = 1.20$  m/s:  $t =$  (i) 0 ms (touch-down), (ii) 0 ms, (iii) 0.37 ms, (iv) 2.5 ms, (v) 3.93 ms, (vi) 4.63 ms, and (vi) 5.25 ms. The left part of each numerical snapshot shows the dimensionless viscous dissipation function,  $\xi$  on a  $\log_{10}$  scale and the right part the velocity field magnitude normalized with the impact velocity. The black velocity vectors are plotted in the center of mass reference frame of the drop to elucidate the internal flow. (b) Spreading diameter  $D(t)$  and impact force  $F(t)$  on the substrate as function of time: comparison between experiments and simulations ( $W\epsilon = 40$ ). The insets show representative snapshots at specific time instants overlaid with the drop boundaries from simulations in orange, revealing good agreement.  $F_1 \approx 5.1$  mN and  $F_2 \approx 2.3$  mN are the two peaks of the normal force  $F(t)$  at  $t_1 \approx 0.37$  ms and  $t_2 \approx 4.63$  ms, respectively.  $t_m$  is the moment corresponding to the maximum spreading of the drop and  $t_3$  represents the end of contact ( $F = 0$ ).  $D_m$  and  $D_2$  are the spreading diameters of the drop at  $t_m$  and  $t_2$ , respectively. Also see supplemental movie 1.

$$\mathbf{F}(t) = F(t)\hat{\mathbf{z}} = \left( \int_{\mathcal{A}} (p - p_0) d\mathcal{A} \right) \hat{\mathbf{z}}, \quad (1.1)$$

where  $p_0$  is the ambient pressure. Furthermore,  $\mathcal{A}$  and  $\hat{\mathbf{z}}$  are the area of the superhydrophobic substrate and a unit vector perpendicular to it, respectively (also see appendix 1.B for details of the simulation setups).

The initial drop diameter  $D$  ( $2.05 \text{ mm} \leq D \leq 2.76 \text{ mm}$ )<sup>①</sup> and the impact velocity  $V$  ( $0.38 \text{ m/s} \leq V \leq 2.96 \text{ m/s}$ ) are independently controlled. The drop material properties are kept constant (density  $\rho_d = 998 \text{ kg/m}^3$ , surface tension coefficient  $\gamma = 73 \text{ mN/m}$ , and dynamic viscosity  $\eta_d = 1.0 \text{ mPas}$ ). All experiments were carried out at ambient air pressure and temperature. The Weber number (ratio of drop inertia to capillary pressure)  $We \equiv \rho_d V^2 D / \gamma$  ranges between  $1 - 400$  and the Reynolds number (ratio of inertial to viscous stresses)  $Re \equiv \rho_d V D / \eta_d \approx 800$  to  $10^5$ . Note that for our simulations, we keep the drop Ohnesorge number (ratio of inertio-capillary to inertio-viscous timescales)  $Oh \equiv \eta_d / (\rho_d \gamma D)^{1/2}$  constant at  $0.0025$  to mimic  $2 \text{ mm}$  diameter water drops.

### 1.3 Formation of a second peak in the force

In this section, we elucidate the temporal variation of the normal reaction force and the corresponding drop impact dynamics. Figure 1.2(a) illustrates the different stages of the drop impact process for  $We = 40$ , and figure 1.2(b) quantifies the spreading diameter  $D(t)$  (maximum width of the drop at time  $t$ ) and the normal force  $F(t)$  (also see supplemental movie 1). Note the remarkable quantitative agreement between the experimental and the numerical data for both  $D(t)$  and  $F(t)$ , giving credibility to both. As the drop touches the surface (figure 1.2a-i), the normal force  $F(t)$  increases sharply to reach the first peak with amplitude  $F_1 \approx 5.1 \text{ mN}$  in a very short time  $t_1 \approx 0.37 \text{ ms}$  (figure 1.2a-ii). At this instant, the spreading diameter  $D(t)$  is equal to the initial drop diameter  $D$ ,  $D(t_1) \approx D$  [? ? ? ? ?]. Subsequently, the normal force reduces at a relatively slow rate to a minimum ( $\approx 0 \text{ mN}$ ) at  $t_m \approx 2.5 \text{ ms}$ . Meanwhile the drop reaches a maximum spreading diameter  $D(t_m) = D_m$  (figure 1.2a-iii). The force profile  $F(t)$ , until this instant, is very close to that on a hydrophilic surface (see § 1.C). However, contrary to the wetting

<sup>①</sup>Note that we use diameter of the drop as the length scale in this chapter contrary to its radius that we use throughout this thesis. We do so for ease of comparison with the earlier work of ? ], see figures 1.3 and 1.4.

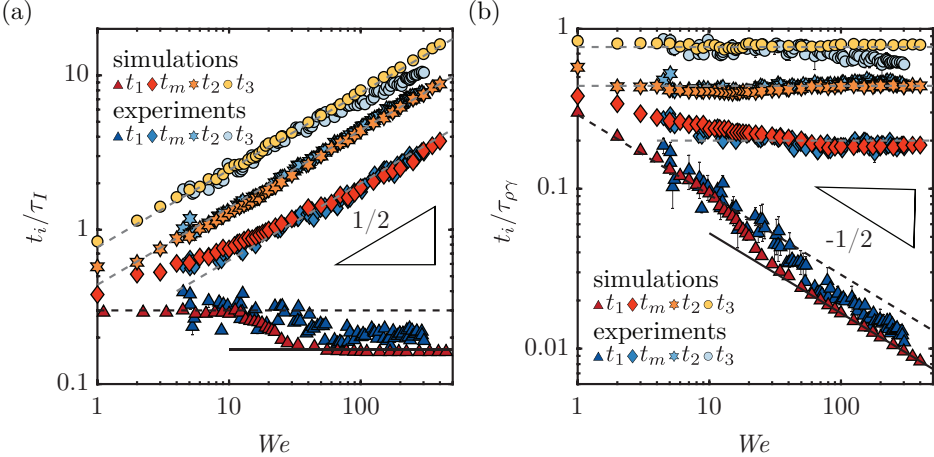


Figure 1.3: Characteristic times as functions of the Weber number  $We$ . The times  $t_1$ ,  $t_m$ ,  $t_2$ , and  $t_3$  are normalized by the inertial timescale  $\tau_I = D/V$  in panel (a), or by the inertia-capillary timescale  $\tau_{\rho\gamma} = (\rho_d D^3 / \gamma)^{1/2}$  in panel (b). The black dashed and solid lines represent  $t_1 \sim \tau_I$ . The black dashed and solid lines represent  $t_1 \approx 0.3\tau_I$  and  $t_1 \approx 1/6\tau_I$ , respectively. The gray dashed lines show the best straight line fits to the experimental data,  $t_m \approx 0.20\tau_{\rho\gamma}$ ,  $t_2 \approx 0.44\tau_{\rho\gamma}$ , and  $t_3 \approx 0.78\tau_{\rho\gamma}$ .

scenario, on superhydrophobic substrates, the drop starts to retract, creating high local viscous dissipation in the neck region connecting the drop with its rim (figure 1.2a-iii,iv). Through this phase of retraction, the normal reaction force is small, but shows several oscillations owing to traveling capillary waves for  $2.5 \text{ ms} < t < 3.8 \text{ ms}$  (figure 1.2b). The drop retraction and the traveling capillary waves lead to flow focusing at the axis of symmetry, creating the Worthington jet (figure 1.2a-iv,v) and hence also the opposite momentum jet that results in an increase in the normal force  $F(t)$ . Consequently, the hitherto unknown second peak appears, here with an amplitude  $F_2 \approx 2.3 \text{ mN}$  and at time  $t_2 \approx 4.63 \text{ ms}$ . Lastly, the normal force  $F(t)$  decays slowly (figure 1.2a-v,vi) to zero, finally vanishing at  $t_3 \approx 8.84 \text{ ms}$ . This time instant  $t_3$  is a much better estimate for the drop contact time as compared to the one observed at complete detachment from side view images which is about 2 ms longer in this case [? ? ]. Therefore, in summary, here we have identified the mechanism for the formation of the second peak in the normal force and four different characteristic times,  $t_1$ ,  $t_m$ ,  $t_2$ , and  $t_3$  (figure 1.2b).

## 1.4 Weber number dependence of the characteristics times

Next, we look into the dependence of the four different characteristic times on the impact Weber number  $We$ . The instant  $t_1$  of the first peak of the force  $F(t)$  scales with the inertial timescale (figure 1.3a), i.e.,  $t_1 \sim \tau_I = D/V$  with different  $We$ -dependent prefactors ( $\approx 0.3$  at low and  $\approx 0.167$  at high  $We$ , respectively). The solid black line in figure 1.3(a) is the theoretical inertial prediction by [?],  $t_1/\tau_I = 1/6$ , and matches our experimental and in particular numerical data. As seen from figure 1.3, the other three characteristic times scale differently with  $We$  than  $t_1$ . Specifically,  $t_2$  and  $t_3$  become independent of  $We$  when rescaled with the inertio-capillary time  $\tau_\gamma = (\rho_d D_0^3 / \gamma)^{1/2}$  while  $t_m$  has a weak  $We$ -dependence at low  $We$ , and becomes  $We$ -independent only for  $We \gtrsim 10$ , see figure 1.3(b). The reason for this  $We$ -independent behavior is that the impact process is analogous to one complete drop oscillation [?] which is determined by the inertio-capillary time  $\tau_{\rho\gamma}$  [?]. Maximum spreading ( $t_m$ ) occurs at almost one-quarter of a full oscillation (consistent with our result  $t_m \approx 0.20\tau_{\rho\gamma}$ ) whereas the complete contact time  $t_3$  takes about one full oscillation (consistent with our result  $t_3 \approx 0.78\tau_{\rho\gamma}$ ). Finally, the time instant  $t_2 \approx 0.44\tau_{\rho\gamma}$  of the second peak in the impact force coincides with the time when the drop's motion changes from being predominantly radial to being vertical, as this moment is associated with the formation of the Worthington jet [?, p. 18-20]. Note that here for the impact on the superhydrophobic substrate, the duration of non-zero forces (e.g., for  $We = 40$  we find  $t_3/\tau_I \approx 5.2$ , figure 1.2c) is much longer than that for the impact on a hydrophilic surfaces [?, ?], where for the same  $We = 40$  one has  $t_3/\tau_I \approx 2.0$  (also see § 1.C).

## 1.5 Influence of Weber number on the first peak

As the drop falls on a substrate, momentum conservation implies  $F_1 \sim V(dm/dt)$ , where the mass flux  $dm/dt$  can be calculated as  $dm/dt \sim \rho_d V D^2$  [? ]. As a result,  $F_1 \sim \rho_d V^2 D^2$ , as shown in figure 1.4(a) for high Weber numbers ( $We > 30$ ,  $F_1 \approx 0.81\rho_d V^2 D^2$ ). This asymptote also matches the experimental and theoretical results of similar studies conducted on hydrophilic substrates [?, ?]. Indeed, the first peak force originates from an inertial shock following the impact of drops onto an immobile substrate and is independent of the wettability. Further, the minimum Reynolds number for the current work is 800, which is well above the criterion ( $Re > 200$ ) for viscosity-independent results

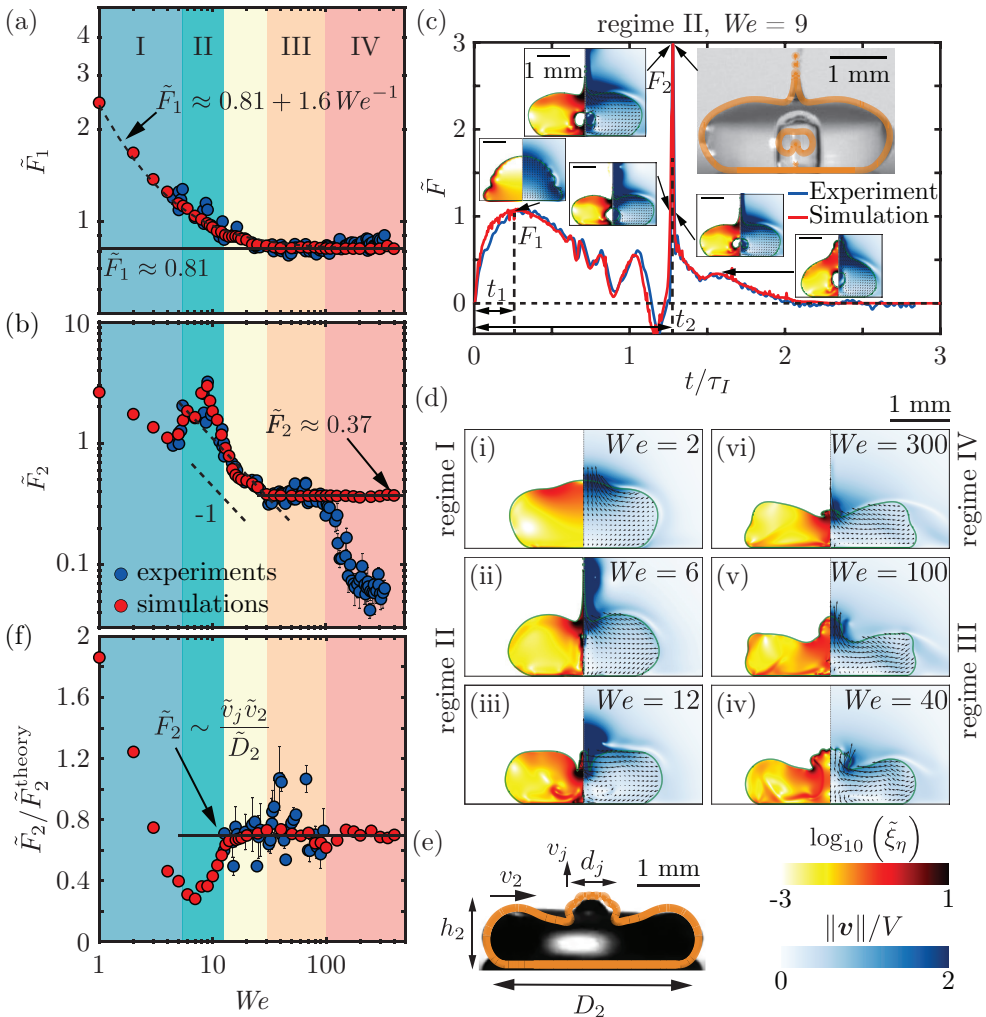


Figure 1.4: Dimensionless peak forces  $\tilde{F}_i \equiv F_i / (\rho_d V^2 D^2)$ , (a)  $\tilde{F}_1$ , (b)  $\tilde{F}_2$  as functions of  $We$ . For  $\tilde{F}_1$ , the black dashed and solid lines represent  $\tilde{F}_1 \approx 0.81 + 1.6 We^{-1}$  and  $\tilde{F}_1 \approx 0.81$ , respectively. Using  $\tilde{F}_2$ , we identify four regimes, I. Capillary ( $We < 5.3$ ), II. Singular jet ( $5.3 < We < 12.6$ ), III. Inertial ( $30 < We < 100$ ), and IV. Splashing ( $We > 100$ ). The black dotted and solid lines represent  $\tilde{F}_2 \sim We^{-1}$  and  $\tilde{F}_2 \sim We^0$ , respectively. (c) Evolution of the normal force  $F(t)$  of an impacting drop for the case with highest  $\tilde{F}_2$  ( $We = 9$ ). Note again the outstanding agreement between the experimental and the numerical results, including the various wiggles in the curve, which originate from capillary oscillations. Insets show drop morphology at specific time instants. (d) Snapshots at the instants of the second peak force ( $t_2$ ) for  $We =$  (i) 6, (ii) 12, (iii) 40, (iv) 100, and (v) 300. (e) Drop geometry at  $t_2$  for  $We = 40$  (along with the orange drop contour from numerics) to mark its spreading diameter  $D_2$ , height  $h_2$ , retraction velocity  $v_2$ , jet diameter  $d_j$  and jet velocity  $v_j$ . (f) Comparison of the second peak force  $\tilde{F}_2$  with its theoretical prediction  $\tilde{F}_2^{\text{theory}} = \tilde{v}_j \tilde{v}_2 / \tilde{D}_2$  (equation. (1.3)).

[? ? ]. One would expect  $\tilde{F}_1 \equiv F_1/\rho_d V^2 D^2$  to be constant throughout the range of our parameter space. Nonetheless, when  $We < 30$ , the data deviates from the inertial asymptote. Such deviations have been reported previously on hydrophilic surfaces as well [? ]. Here, inertia is not the sole governing force, and it competes with surface tension. We propose a generalization of the first peak of the impact force to  $F_1 = \alpha_1 \rho_d V^2 D^2 + \alpha_2 (\gamma/D) D^2$ , based on dimensional analysis, with  $\alpha_1$  and  $\alpha_2$  as free parameters. From the best fit to all the experimental and numerical data, we obtain  $\tilde{F}_1 \approx 0.81 + 1.6 We^{-1}$ , which well describes the data, see figure 1.4(a).

## 1.6 Influence of Weber number on the second peak

We now focus on the second peak  $F_2$  of the impact force  $F(t)$ . In figure 1.4(b), we show the  $We$ -dependence of the non-dimensional version thereof,  $\tilde{F}_2 \equiv F_2/(\rho_d V^2 D^2)$ . We identify four main regimes, namely I. Capillary ( $We < 5.3$ ), II. Singular jet ( $5.3 < We < 12.6$ ), III. Inertial ( $30 < We < 100$ ), and IV. Splashing ( $We > 100$ ). The range  $12.6 < We < 30$  marks the transition from the singular jet to the inertial regime.

In regime I ( $We < 4.5$ ), the amplitude  $F_2$  of the second peak is smaller than the resolution (0.5 mN) of our force transducer, so we cannot distinguish it in experiments. Capillary oscillations dominate the flow in this regime [? ], leading to more than two peak forces, remarkably perfectly identical to what is observed in our simulations (see figure 1.4d-i and supplemental movie 2).

In regime II, with increasing  $We$ , there is a sharp increase in the amplitude  $\tilde{F}_2$  of the second peak. A striking feature of this regime is that the magnitude of the second peak force exceeds that of the first one,  $\tilde{F}_2 > \tilde{F}_1$ , see figure 1.4(c) which illustrates the case with the highest second peak force ( $\tilde{F}_2 = 2.98$ , occurring for  $We = 9$ , supplemental movie 3). The large force amplitude in this regime correlates to the formation of an ultra-thin and high-velocity singular Worthington jet [? ]. Here, the Worthington jet is most pronounced as it results from the collapse of an air-cavity as well as the converging capillary waves (see insets of figures 1.4c and 1.4d-ii, iii). It is reminiscent of the hydrodynamic singularity that accompanies the bursting of bubbles at liquid-gas interfaces [see § chap:BurstingBubbleVP and ? ? ]. Outside regime II such bubbles do not form, see figure 1.4(d-iii – d-v). Consistent with this view, the case with maximum peak force ( $We = 9$ , figure 1.4b) entrains the largest bubble. Another characteristic feature of this converging flow is that, despite having a small Ohnesorge number (= 0.0025) that is often associated with

inviscid potential flow inside the drop [?], it still shows high rates of local viscous dissipation near the axis of symmetry (figures 1.4c insets and 1.4(d-i – d-iii)), due to the singular character of the flow (also see supplemental movie 4).

When  $We$  is further increased, we (locally) find  $\tilde{F}_2 \sim We^{-1}$  in the transition regime ( $12.6 < We < 30$ ), followed by  $\tilde{F}_2 \sim We^0$  in the inertial regime III ( $30 < We < 100$ ). Specifically, by employing best fits, we obtain

$$\tilde{F}_2 = \frac{F_2}{\rho_d V^2 D^2} \approx \begin{cases} 11 We^{-1} & (12.6 < We < 30), \\ 0.37 & (30 < We < 100). \end{cases} \quad (1.2)$$

We will now rationalize this experimentally and numerically observed scaling behavior of the amplitude  $F_2$  of the second peak using scaling arguments. As already mentioned, figure 1.4(d) shows that the second peak in the force at  $t_2$  coincides with an upwards jet, which has typical velocity  $v_j$  (see § 1E for calculation details) and typical diameter  $d_j$ , figure 1.4(e). Figure 1.4(d) also illustrates strong radially symmetric flow focusing due to the retracting drop in regimes II and III. We define the recoiling velocity of the drop at time  $t_2$  as  $v_2$ , the droplet height at that moment as  $h_2$ , and the droplet diameter at that moment as  $D_2 = D(t_2)$ , see again figure 1.4(e). Note that regime II also includes stronger converging capillary waves and the collapsing air cavity (figure 1.4c insets and Fig. 1.4d-i,ii). The presence of the substrate breaks the symmetry in vertical direction, directing the flow into the Worthington jet. Using continuity and balancing the volume flux at this instant  $t_2$ , we obtain  $v_2 D_2 h_2 \sim v_j d_j^2$ . Of course,  $D_2$  and  $h_2$  are also related by volume conservation. Assuming a pancake-type shape at  $t_2$ , we obtain  $D_2^2 h_2 \sim D^3$  [?] and therefore,  $v_j d_j^2 \sim v_2 D^3 / D_2$ . As the drop retracts, the velocity of the flow field far away from the jet is parallel to the base (figure 1.4d). So, the occurrence and strength of the second peak  $F_2$  is mainly a result of the flow opposite to the vertical Worthington jet (figure 1.4c-iii – c-v), which naturally leads to  $F_2 \sim \rho_d v_j^2 d_j^2$  (momentum flux balance in the vertical direction). Combining the above arguments, we get  $F_2 \sim \rho_d v_j v_2 D^3 / D_2$  which can be non-dimensionalized with the inertial pressure force  $\rho_d V^2 D^2$  to obtain

$$\tilde{F}_2 = \frac{F_2}{\rho_d V^2 D^2} \sim \frac{\tilde{v}_j \tilde{v}_2}{\tilde{D}_2}, \quad (1.3)$$

where,  $\tilde{v}_j = v_j/V$ ,  $\tilde{v}_2 = v_2/V$ , and  $\tilde{D}_2 = D_2/D$  are the dimensionless jet velocity, drop retraction velocity, and spreading diameter, respectively, all at  $t_2$ .

Figure 1.4(f) compares the amplitude of the second peak as obtained from the experiments and simulations with the theoretical prediction of equation (1.3) (also see § 1.E). Indeed, this scaling relation reasonably well describes the transitional regime II-III and regime III data. Obviously, in regime I, the theoretical prediction is invalid because the hypothesis of flow focusing breaks down, and capillary oscillations dominate the flow, with no Worthington jet occurring. Further, equation (1.3) over-predicts the forces in regime II because efficient capillary waves focusing and air cavity collapse lead to extremely high-velocity singular jets. The entrained air bubble also shields momentum transfer from the singular Worthington jet to the substrate (insets of figure 1.4c).

We finally come to the very large impact velocities of regime IV. Then, when  $We \gtrsim 100$ , in the experiments splashing occurs [?], see supplemental movie 5. At such high  $We$ , the surrounding gas atmosphere destabilizes the rim [? ?]. Therefore, in regime IV, kinetic and surface energies are lost due to the formation of satellite droplets, resulting in diminishing  $\tilde{F}_2$  in the experiments (figure 1.4b). In contrast, for our axisymmetric (by definition) simulations, the above-mentioned azimuthal instability is absent [?] and the plateau  $\tilde{F}_2 \approx 0.37$  continues in this regime. Consequently, equation (1.3) holds only for the simulations in regime IV (figure 1.4f), and not for the experiments. Further analysis of the experimentally observed fragmentation scenario is beyond the scope of the present work. For future work, we suggest that one could also experimentally probe  $F_2$  in this regime by suppressing the azimuthal instability (for instance, by reducing the atmospheric pressure [?]).

## 1.7 Conclusions and outlook

In this chapter, we have experimentally obtained the normal force profile of water drops impacting superhydrophobic surfaces. To elucidate the physics and study the internal flow, we used direct numerical simulations, which perfectly match the experimental results without any fitting parameter. In the force profile, we identified two prominent peaks. The first peak arises from an inertial shock following the impact of the impacting drop onto the immobile substrate. The hitherto unknown second peak occurs before the drop rebounds. The variation of the amplitude of this peak with Weber number results in four distinct regimes, namely the capillary, singular jet, inertial, and splashing regime. This peak in the force occurs due to the momentum

balance when the Worthington jet is created by flow focusing, owing either to capillary waves (singular jet regime) or drop retraction (inertial regime). Surprisingly, even a low Weber number impact (singular jet regime) can lead to a highly enhanced peak in the force profile, triggered by the collapse of an air cavity. Lastly, we have derived scaling relations for these peak forces. Our results thus give a fundamental understanding of the drop impact dynamics on a non-wetting surface and the forces associated with it. Such insight is crucial to develop countermeasures to the failure of superhydrophobicity in technological applications (for e.g., by avoiding the regime  $5.3 < We < 12.6$  or reducing the spacing of the textures [? ]). Interesting and relevant extensions of our work include the study of impact forces of viscous drops, which will show quite different scaling behavior [? ], and of Leidenfrost drops [? ].

## Acknowledgments

We thank Marie-Jean Thoraval, Uddalok Sen, and Pierre Chantelot for stimulating discussions.

# Appendix

## 1.A Experimental method

Figure 1.A.1a illustrates the experimental setup that consists of four main units: a drop generation unit, a superhydrophobic substrate, a force measurement unit and a high-speed photography unit (also see figure 1.1a).

### 1.A.1 Drop generation unit

The drop generation unit is used to create drops of different sizes and impact velocities independently (initial drop diameter  $D$  ( $2.05\text{ mm} \leq D \leq 2.76\text{ mm}$ ) and the impact velocity  $V$  ( $0.38\text{ m/s} \leq V \leq 2.96\text{ m/s}$ )). Deionized water drops are created by employing suspended needles that are connected to a syringe pump. To suppress disturbances, the drop is created at a very smooth flow rate, i.e.,  $0.5\text{ mL/min}$ . The drop diameter is varied by employing needles of different sizes, and the impact velocity is controlled by changing the distance between the needle and the sample by employing a vertical translation stage.

### 1.A.2 Superhydrophobic substrate

A water drop impacts a quartz plate whose upper surface is coated with silanized silica nanobeads with diameter of  $20\text{ nm}$  (Glaco Mirror Coat Zero; Soft99) [? ?] to attain superhydrophobicity (figure 1.A.1b). The advancing and receding contact angles of water drops are  $167^\circ \pm 2^\circ$  and  $154^\circ \pm 2^\circ$ , respectively.

### 1.A.3 Force measurement unit

The core apparatuses of the force measurement unit include a sample, a high-precision transducer, a charge amplifier and a data acquisition system. The

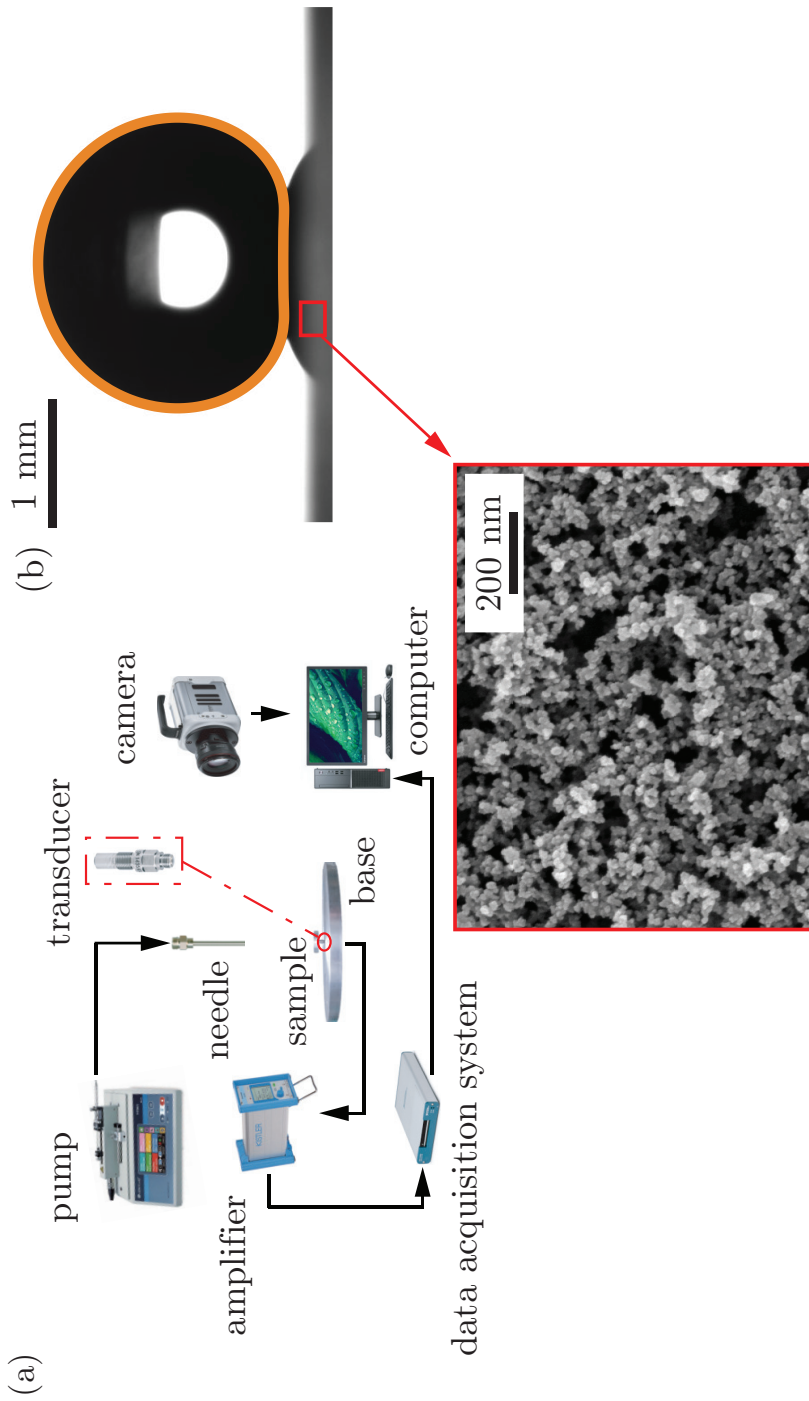


Figure 1.A.1: (a) Experimental setup, consisting of four main units: a drop generation unit, a superhydrophobic substrate, a force measurement unit, and a high-speed photography unit. Relevant appurtenant devices are shown. Also see figure 1.1(a). (b) Snapshot of a water drop sitting on a superhydrophobic substrate with overlaid orange boundary from simulation. The inset shows the scanning electron microscopy (SEM) image of the superhydrophobic surface covered by hydrophobic nanoparticles.

lower surface of the quartz plate is glued to an aluminum base, which is screwed vertically into a high-precision piezoelectric force transducer (Kistler 9215A) with a resolution of 0.5 mN. The impact force between the drop and the sample is measured by the collection of the charge generated by the transducer, and the charge is immediately converted into a voltage by employing an amplifier (Kistler 5018A). Comparing to the weak charge signal that is sensitive to the environment noise (such as triboelectricity due to the movement of the cable, or magnetic fields in the environment, etc.), the amplified voltage signal is more robust for transmitting and processing. After that, the amplified analog signals are converted into the digital signals by employing a data acquisition system (NI USB-6361 driven by Labview) at a sampling rate of 100 kHz. Finally, the unit of the measured signal is changed from Voltage (V) to Newton (N) via the calibration coefficient of the force transducer.

In our experiment, high-frequency vibrations of the experimental setup are inevitably induced by the drop impact, and they will superimpose on the temporal evolution of the impact force. Based on a well-designed method [?], the influences resulting from these high-frequency vibrations have been successfully removed by employing a low pass filter (with a cut-off frequency of 5 kHz).

#### 1.A.4 High-speed photography

Lastly, the fast force sensing technique described above is synchronized with the high-speed photography unit containing a high-speed camera (Photron Fastcam Nova S12) and a micro Nikkor 105 mm f/2.8 imaging lens. To realize a synchronization of the evolution of the drop morphology and the transient force, the high-speed camera is triggered by the data acquisition system when the impact force is larger than 1 mN. A LED light (CLL-1600TDX) of adjustable output power is used to illuminate the scene of the impingement. We efficiently record the drop impact phenomenon at 10,000 fps with a shutter speed 1/20,000 s.

## 1.B Numerical method

This section elucidates the direct numerical simulation framework used to study the drop impact process (figure 1.1b) using the free software program, Basilisk C [?].

### 1.B.1 Governing equations

For an incompressible flow, the mass conservation requires the velocity field to be divergence-free ( $\nabla \cdot \mathbf{v} = 0$ ). Furthermore, the momentum conservation reads

$$\frac{\partial(\rho\mathbf{v})}{\partial t} + \nabla \cdot (\rho\mathbf{v}\mathbf{v}) = -\nabla p' - [\rho](\mathbf{g} \cdot \mathbf{z}) \hat{\mathbf{n}}\delta_s + \nabla \cdot (2\eta\mathcal{D}) + \mathbf{f}_\gamma. \quad (1.4)$$

Here, the terms on the left hand side represent momentum advection. On the right hand side, the deformation tensor,  $\mathcal{D}$  is the symmetric part of the velocity gradient tensor ( $\mathcal{D} = (\nabla\mathbf{v} + (\nabla\mathbf{v})^T)/2$ ). Further,  $p'$  denotes reduced pressure field,  $p' = p - \rho\mathbf{g} \cdot \mathbf{z}$ , where,  $p$  and  $\rho\mathbf{g} \cdot \mathbf{z}$  represent the mechanical and the hydrostatic pressures, respectively, with  $\mathbf{g}$  and  $\mathbf{z} = z\hat{\mathbf{z}}$  representing the gravitational acceleration and the vertical coordinate vectors, respectively ( $z$  is the distance away from the superhydrophobic substrate and  $\hat{\mathbf{z}}$  is a unit vector, see figure 1.1b). Using this reduced pressure approach ensures an exact hydrostatic balance as described in [? ?]. We also use this reduced pressure approach in chapter 2. Note that this formulation requires an additional singular body force ( $[\rho](\mathbf{g} \cdot \mathbf{z}) \hat{\mathbf{n}}\delta_s$ ) at the interface. Here,  $[\rho]$  is the density jump across the interface,  $\hat{\mathbf{n}}$  is the interfacial normal vector,  $\hat{\mathbf{n}} = \nabla H/\|\nabla H\|$ , and  $\delta_s$  is the Dirac-delta function,  $\delta_s = \|\nabla H\|$ , where  $H$  is the Heaviside function. Consequently,  $\delta_s$  is non-zero only at the liquid-air interface and has units of 1/length [? ]. Furthermore, we employ one-fluid approximation [? ?] to solve these equations employing volume of fluid (VoF) method for interface tracking, whereby the Heaviside function can be approximated by the VoF marker function  $\Psi$  ( $\Psi = 1$  inside the liquid drop, and  $\Psi = 0$  in the air). Subsequently, the material properties (such as density  $\rho$  and viscosity  $\eta$ ) change depending on which fluid is present at a given spatial location,

$$\rho = \Psi\rho_d + (1 - \Psi)\rho_a, \quad (1.5)$$

$$\eta = \Psi\eta_d + (1 - \Psi)\eta_a, \quad (1.6)$$

where, the subscripts  $d$  and  $a$  denote drop and air, respectively. The VoF marker function ( $\Psi$ ) follows the advection equation [? ?],

$$\left( \frac{\partial}{\partial t} + \mathbf{v} \cdot \nabla \right) \Psi = 0. \quad (1.7)$$

Lastly, a singular body force  $\mathbf{f}_\gamma$  is applied at the interfaces to respect the dynamic boundary condition. The approximate forms of this force follows [? ]

$$\mathbf{f}_\gamma = \gamma \kappa \delta_s \hat{\mathbf{n}} \approx \gamma \kappa \nabla \Psi. \quad (1.8)$$

Here,  $\gamma$  is the drop-air surface tension coefficient and  $\kappa$  is the curvature calculated using the height-function method. During the simulations, the maximum time-step needs to be less than the oscillation period of the smallest wave-length capillary wave because the surface-tension scheme is explicit in time [? ? ].

In our simulations, ideal superhydrophobicity is maintained by assuming that a thin air layer is present between the drop and the substrate [? ]. The normal force on this substrate can be calculated using [? ]

$$\mathbf{F}(t) = \int_{\mathcal{A}} ((p - p_0) (\mathbf{I} \cdot \hat{\mathbf{z}}) - 2\eta_a (\mathbf{D} \cdot \hat{\mathbf{z}})) d\mathcal{A}, \quad (1.9)$$

where,  $p$  and  $p_0$  are the dynamic pressure distribution at the substrate and the ambient pressure, respectively. Here,  $\mathbf{I}$  is the second-order identity tensor. Further,  $\hat{\mathbf{z}}$  is the unit vector normal to the substrate (figure 1.1b) and  $\mathcal{A}$  represents substrate's area. Note that the contribution from the second term on the right-hand side of equation (1.9) is the normal viscous force due to the air layer between the drop and the substrate and is negligible as compared to the pressure integral. Therefore, we can calculate the normal impact force simply by integrating the pressure field at the substrate (see equation (1.1)).

Despite a low viscosity associated with the water drops, the viscous dissipation can still be significant in some cases, especially during flow focusing and capillary waves resonance (see figures 1.4c,d). To identify these regions of high viscous dissipation, we also measure the viscous dissipation function, given by [? ]

$$\xi_\eta = 2\eta (\mathbf{D} : \mathbf{D}), \quad (1.10)$$

which on non-dimensionalization using the drop diameter ( $D$ ), density ( $\rho_d$ ), and impact velocity ( $V$ ) gives

$$\tilde{\xi}_\eta \equiv \frac{\xi_\eta}{\rho_d V^3 / D} = \frac{2}{Re} \left( \Psi + \frac{\eta_a}{\eta_d} (1 - \Psi) \right) (\tilde{\mathbf{D}} : \tilde{\mathbf{D}}), \quad (1.11)$$

where, the Reynolds number ( $Re = \rho_d V D / \eta_d$ ) is the ratio of inertial to viscous stresses, and  $\tilde{\mathbf{D}} = \mathbf{D} / (V/D)$ .

### 1.B.2 Relevant dimensionless numbers

In the experiments, the initial drop diameter  $D$  ( $2.05 \text{ mm} \leq D \leq 2.76 \text{ mm}$ ) and the impact velocity  $V$  ( $0.38 \text{ m/s} \leq V \leq 2.96 \text{ m/s}$ ) are independently controlled. The drop material properties are kept constant (density  $\rho_d = 998 \text{ kg/m}^3$ , surface tension coefficient  $\gamma = 73 \text{ mN/m}$ , and dynamic viscosity  $\eta_d = 1.0 \text{ mPas}$ ). As a result, we identify the following dimensionless numbers,

$$We = \frac{\rho_d V^2 D}{\gamma} \quad (1.12)$$

$$Oh = \frac{\eta_d}{\sqrt{\rho_d \gamma D}} \quad (1.13)$$

$$Bo = \frac{\rho_d g D^2}{\gamma} \quad (1.14)$$

where,  $We$  is the impact Weber number which is a ratio of the inertial to capillary pressures. The Ohnesorge number ( $Oh$ ) is the ratio between the inertia-capillary to the inertia-viscous time scales and is kept constant at 0.0025 to mimic 2 mm diameter water drops. Furthermore, the Bond number ( $Bo$ ) is the ratio of the gravitational to the capillary pressure, which is also fixed at 0.5 for the same reason. To test the sensitivity of our results on  $Bo$ , we also varied its value as  $0.0005 \leq Bo \leq 0.5$  with no effect on the magnitude of the forces or the four regimes reported in figure 1.4. Lastly, to minimize the influence of the surrounding medium,  $\rho_a/\rho_d$  and  $\eta_a/\eta_d$  are fixed at  $10^{-3}$  and  $3 \times 10^{-3}$ , respectively.

### 1.B.3 Domain description

Figure 1.1(b) represents the axi-symmetric computational domain where  $r = 0$  denotes the axis of symmetry. A no-slip and non-penetrable boundary condition is applied on the substrate along with zero pressure gradient. Here, we also use  $\Psi = 0$  to maintain a thin air layer between the drop and the substrate. Physically, it implies that the minimum thickness of this air layer is  $\Delta/2$  throughout the whole simulation duration (where  $\Delta$  is the minimum grid size). Further, boundary outflow is applied at the top and side boundaries (tangential stresses, normal velocity gradient, and ambient pressure are set to zero).

Furthermore, the domain boundaries are far enough not to influence the drop impact process ( $L_{\max} \gg D$ ). Basilisk C [? ] also allows for adaptive

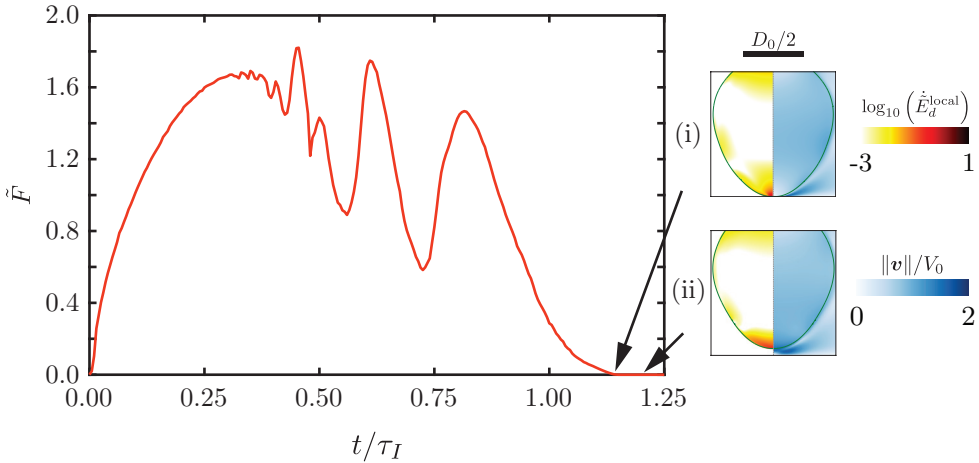


Figure 1.B.1: Temporal variation of the normal contact force for  $We = 2$ . The insets show two key instances: (i) time  $t_3 = 1.14\tau_I$  when  $F$  vanishes which marks the contact time of the drop at the substrate and (ii) detachment time ( $1.2\tau_I$ ) as seen from the side view image. Also see supplemental movie S2.

mesh refinement (AMR) with maximum refinement in the regions of high velocity gradients and at the drop-air interface. With such an adaptive mesh refinement, we can resolve the length scales pertinent to capture the bouncing process, i.e., the flow inside the drop and the region near the substrate. The adaption is based on minimizing the error estimated using the wavelet algorithm [? ] in the volume of fluid tracers, interfacial curvatures, velocity field, vorticity field and rate of viscous dissipation with tolerances of  $10^{-3}$ ,  $10^{-4}$ ,  $10^{-2}$ ,  $10^{-2}$ , and  $10^{-3}$ , respectively [? ]. We also undertook a mesh independence study to ensure that the results are independent of this mesh resolution. We use a minimum grid size  $\Delta = D/1024$  for this study. Note that the cases in regime II (singular jet) requires a refinement of  $\Delta \approx D/4098$  near the axis of symmetry. The simulation source codes, as well as the post-processing codes used in the numerical simulations, are permanently available at author's GitHub repository [? ].

#### 1.B.4 Calculating the time of contact

In the main text, we emphasize that the time instant  $t_3$  at which the normal contact force between the drop and the substrate vanishes is a much better estimate for the drop contact time as compared to the one observed at complete

detachment from side view images. This observation is consistent with the literature [? ? ? ?] and is elucidated in Fig. 1.B.1 for  $We = 2$ . In this case,  $t_3 = 1.14\tau_I$  whereas the side view images show complete detachment at  $t = 1.2\tau_I$ . The effect is further enhanced for higher  $We$ , see for comparisons, supplemental movies S1 ( $We = 40$ ) and S2 ( $We = 2$ ).

## 1.C Superhydrophobic vs. hydrophilic surfaces

To differentiate between impact forces on superhydrophobic surfaces to that of hydrophilic ones [? ? ? ? ? ? ?], we carry out test impacts on hydrophilic surfaces. The hydrophilic sample is a quartz plate, cleaned by surfactant, deionized water, alcohol and deionized water in sequence before the experiment. The advancing and receding contact angles of the deionized water drops on the quartz surface are  $47^\circ \pm 2^\circ$  and  $13^\circ \pm 2^\circ$ , respectively (figure 1.C.1a). The superhydrophobic surface is a Glaco-coated quartz plate [? ?] as described in § 1.A.2, on which the advancing and receding contact angles are  $167^\circ \pm 2^\circ$  and  $154^\circ \pm 2^\circ$ , respectively (figure 1.C.1b).

Figure 1.C.1c compares the impact on superhydrophobic and hydrophilic substrates for impact corresponding to  $We = 40.4$  ( $D = 2.05$  mm and  $V = 1.20$  m/s). The comparison shows that in the spreading stage ( $0 < t < 2$  ms), the transient force profiles overlap. In the time span  $2\text{ ms} < t < 9\text{ ms}$ , the transient force profile of the drop impact on the hydrophilic surface only has slight fluctuations around zero. In contrast to the hydrophilic one, there is an obvious peak force (i.e.  $F_2$ , corresponding to  $t \approx 4.63$  ms) in the retraction stage of the drop impact on the superhydrophobic surface.

Furthermore, the impact force  $F_1$  on the superhydrophobic surface is equal to the maximum impact force on the hydrophilic surface. To obtain a comprehensive understanding, we extracted experimental data (the maximum impact force) from previous literature performed on hydrophilic surfaces [? ? ? ? ? ?]. Moreover, we carried out experiments on hydrophilic quartz surfaces with an apparent contact angle of  $40 \pm 4^\circ$ . Then, as shown in Fig. 1.C.1(d), we make a comparison of  $F_1$  between previous work (on hydrophilic surfaces) and our work (on both hydrophilic and superhydrophobic surfaces). As shown in Fig. 1.C.1(d), the data on both superhydrophobic and hydrophilic surfaces in our study are consistent with each other. Furthermore, when  $We > 30$ , the data in the present work and previous literature are consistent with each other. Therefore,  $F_1$  only depends on the Weber number, rather than the wettability of the surface.

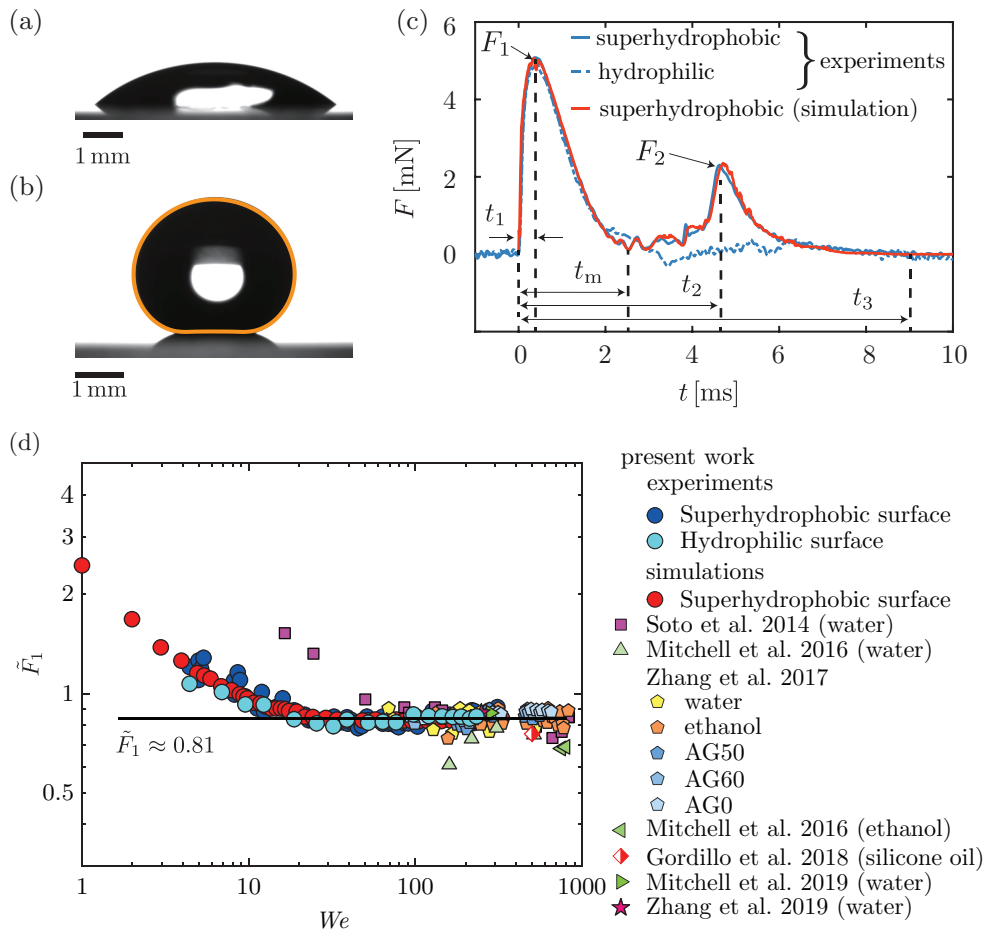


Figure 1.C.1: Wettability of the surfaces and the corresponding transient force profiles. Water drops depositing on (a) hydrophilic and (b) superhydrophobic surfaces with apparent contact angles of  $40^\circ \pm 4^\circ$  and  $165^\circ \pm 1^\circ$ , respectively. For the superhydrophobic case, the drop boundary from simulation is overlaid in orange. (c) Transient force profiles on the hydrophilic and superhydrophobic surfaces. The initial diameter of the drops is 2.05 mm, and the impact velocity is 1.20 m/s, corresponding to  $We = 40$ . (d) Variation of the first dimensionless peak force  $\tilde{F}_1$  as a function of  $We$ . Also see figures 1.2(b) and 1.4(a).

## 1.D Some notes on the different regimes of drop impact

### 1.D.1 Regime II: singular Worthington jet

In the main text, we discussed several features of regime II. In this appendix, we further elucidate this regime using the three representative cases, and look at the transient force profile (figure 1.D.1) and the anatomy of flow inside the drops (figure 1.D.2). We replot the data for  $We = 9$  (figures 1.D.1a and 1.D.2a) which shows the maximum force amplitude, and choose  $We = 5$  (figures 1.D.1b and 1.D.2b) and  $We = 12$  (figures 1.D.1c and 1.D.2c) near the boundaries of regime II (also see supplemental movie 4). The transient force profiles show similar features for these three different Weber numbers. After the impact at  $t = 0$ , there is a sharp increase in the force which reaches the maximum at  $t = t_1$ . As the drops spread further, their morphology feature distinct pyramidal structures owing to the capillary waves [? ] that manifest as oscillations in the temporal evolution of the forces. Then, the drop spreads to a maximum radial extent at  $t = t_m$  followed by the retraction phase as the surface tension pulls the drop radially inwards, further enhancing the capillary waves. These traveling capillary waves interact to form an air-cavity, for instance, see  $t = 0.9t_2$ . The cavity collapses to create high-velocity singular Worthington jets. Subsequently, a bubble is entrained. Comparing the force profile for  $We = 9$  with that of  $We = 5$  and  $We = 12$  reveal differences owing to the corresponding air cavities and bubble entrainment. The flow focusing is the most efficient for  $We = 9$ , as evidence from the sharp peak in the transient force evolution. This capillary resonance leads to a strong downward momentum jet and hence the maximum amplitude  $F_2$  at time  $t = t_2$ . Bubble entrainment does not occur for either  $We = 5$  or  $We = 12$  (see  $t_2 < t < 1.2t_2$ ). Consequently, the maximum force amplitude diminishes for these two cases.

Another characteristic feature of this regime is the occurrence of negative contact force between the drop and the substrate immediately before the formation of a singular Worthington jet and the second peak in normal contact force. Fig. 1.D.3 illustrates one such case for  $We = 9$  where the contact force is negative for  $1.1\tau_I \lesssim t \lesssim 1.2\tau_I$  implying that the drop is pulling on the substrate instead of pushing it (Fig. 1.D.3(a)). Earlier works [? ? ? ] have attributed this negative force to the wetting properties of the substrates, particularly adhesion between the drop and the substrate [? ? ], viscoelastic effects or deformation of the substrate [? ]. However, none of these effects are present in our work. To demystify the occurrence of this negative force, we monitor the pressure field inside the drop (side view, Fig. 1.D.3(b)) and on the

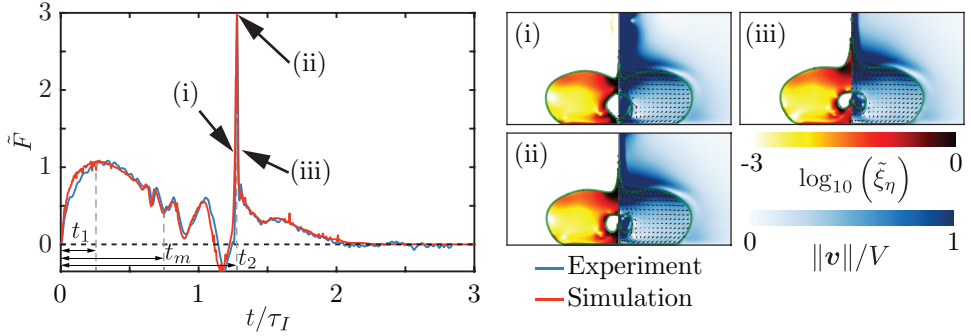
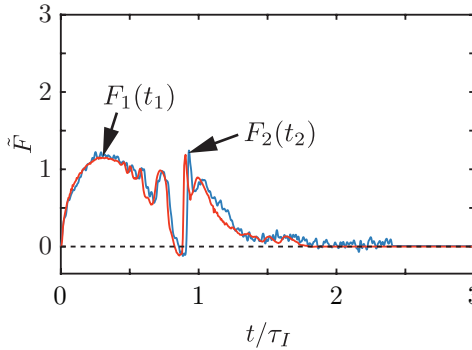
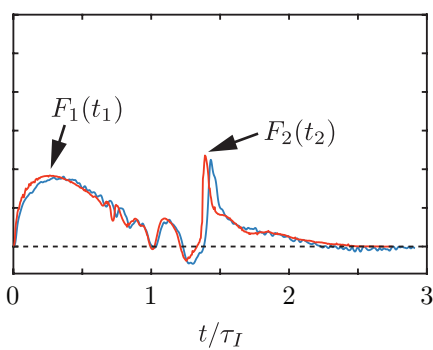
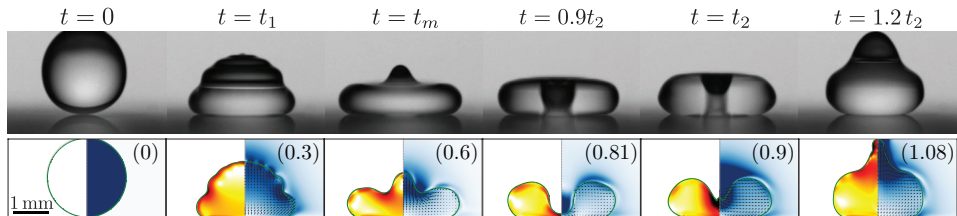
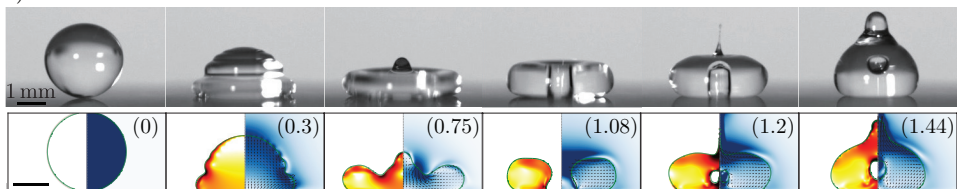
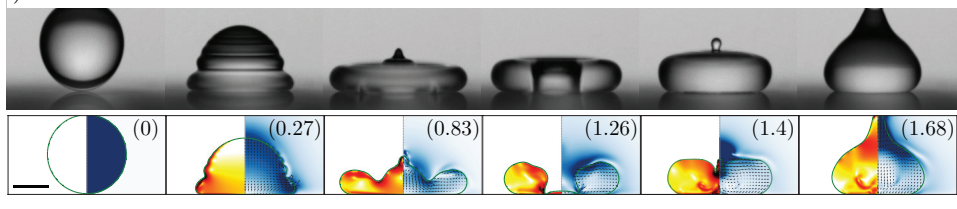
(a)  $We = 9$ (b)  $We = 5$ (c)  $We = 12$ 

Figure 1.D.1: Evolution of the normal force  $\tilde{F}(t) = F(t)/\rho_d V^2 D^2$  of a drop impacting on the superhydrophobic surface in the singular Worthington jet regime for  $We =$  (a) 9, (b) 5, and (c) 12. Insets in panel (a) show the drop morphology and flow anatomy close to the capillary resonance that leads to a hydrodynamic singularity. Note the outstanding agreement between the experimental (blue line) and the numerical (red line) results, including the various wiggles in the curve, which originate from capillary oscillations for panel (a). The left part of each numerical snapshot shows the dimensionless viscous dissipation function  $\tilde{\xi}_\eta$  on a log<sub>10</sub> scale and the right part shows the velocity field magnitude normalized with the impact velocity. The black velocity vectors are plotted in the center of mass reference frame of the drop to clearly elucidate the internal flow.

(a)  $We = 5$ (b)  $We = 9$ (c)  $We = 12$ 

regime II: singular Worthington jet



Figure 1.D.2: Drop impact on the superhydrophobic surface in the singular Worthington jet regime for  $We =$  (a) 9, (ii) 5, and (iii) 12. The left part of each numerical snapshot shows the dimensionless viscous dissipation function  $\tilde{\xi}_\eta$  on a  $\log_{10}$  scale and the right part shows the velocity field magnitude normalized with the impact velocity. The black velocity vectors are plotted in the center of mass reference frame of the drop to clearly elucidate the internal flow. The numbers in the top right of each numerical snapshot mentions the dimensionless time  $t/\tau_I$ .

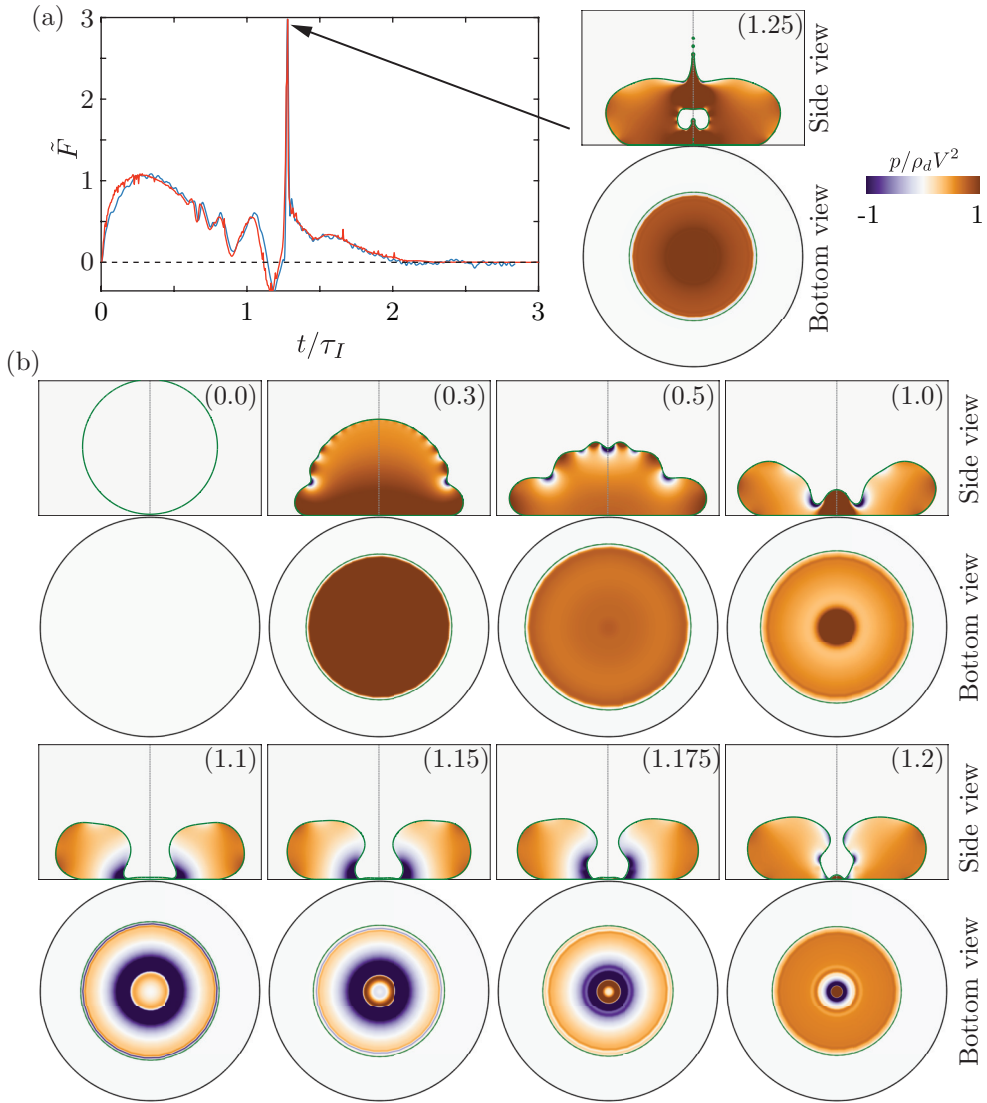


Figure 1.D.3: Contact force and pressure field during drop impact on the superhydrophobic surface in the singular Worthington jet regime,  $We = 9$ . (a) Temporal variation of the contact force. Notice that the contact force is negative for  $1.1\tau_I \lesssim t \lesssim 1.2\tau_I$ . (b) Simulation snapshots showing the pressure field  $p$  normalized by the inertial pressure  $\rho_d V^2$  in the side and bottom view images. The numbers in the top right of each numerical snapshot mentions the dimensionless time  $t/\tau_I$ .

substrate (bottom view, Fig. 1.D.3(b)). We observe large negative pressures (purple regions in the pressure field) on the substrate immediately prior to the formation of a singular Worthington jet and the second peak in normal contact force owing to the negative curvature on the surface of the drop as the air-cavity forms due to focusing of the capillary waves. Consequently, negative capillary pressure causes a pressure deficit inside the drop, and the drop pulls on the substrate instead of pushing it (brown regions in the pressure field).

### 1.D.2 Transitional regime II-III and inertial regime III

In the main text, we used the flow focusing due to drop retraction to find an expression for the amplitude  $F_2$  (see, equation (1.3)) that entails two scaling behaviors depending on the  $We$  (see equation (1.2)). To address the crossover of these two scaling relations, (i.e.,  $We = 30$ ), we check the deformation of the drop at the moment of maximum spreading and the corresponding position of the drop apex.

To make a comparison, we exemplary choose  $We = 20$  ( $D = 2.05\text{ mm}$ ,  $V = 0.83\text{ m/s}$ ) and  $We = 80$  ( $D = 2.05\text{ mm}$ ,  $V = 1.69\text{ m/s}$ ), and show their impact behaviors in figures 1.D.4(a) and (b), respectively. By simulations, the anatomy of the inner flow field of the drop are discernible (see the right panels). For the case  $We = 20$ , the solid-liquid contact region is close to the initial drop diameter when  $F_1$  is attained at  $t_1 = 0.6\text{ ms}$ . Meanwhile, the excited capillary wave propagates along the drop surface and then deforms the drop into a pyramidal shape at  $1.5\text{ ms}$ . Then, the drop reaches its maximum spreading diameter  $D_m$  at  $t_m = 2.3\text{ ms}$ . Notice that at this moment, the drop apex is higher than the height of the rim and is still moving downwards. After that, the drop starts to recoil, and the drop apex descends to its lowest level after  $t_m$ . During the recoil, the retreating drop deforms into a pancake shape with air in the center, as shown at  $4.0\text{ ms}$ . As time progresses, the retracting flow fills the cavity and creates an upward jet at  $t_2 = 4.5\text{ ms}$ , which results in  $F_2$ .

On the other hand, for the case with  $We = 80$ , a thin liquid film appears, and the solid-liquid contact area is close to the initial drop diameter when  $F_1$  is attained, similar to the case with  $We = 20$ . However, unlike the previous case,  $t_1 = 0.2\text{ ms}$  (see § 1.4). Moreover, there is no obvious capillary wave propagating on the drop surface, as shown at  $1.0\text{ ms}$ . Then, the drop apex continuously moves downwards, and its height reaches the height of the rim, and this moment happens before the drop reaches its maximum spreading diameter  $D_m$  at  $t_m = 2.0\text{ ms}$ . Shortly after  $t_m$ , the drop recoils, while the film

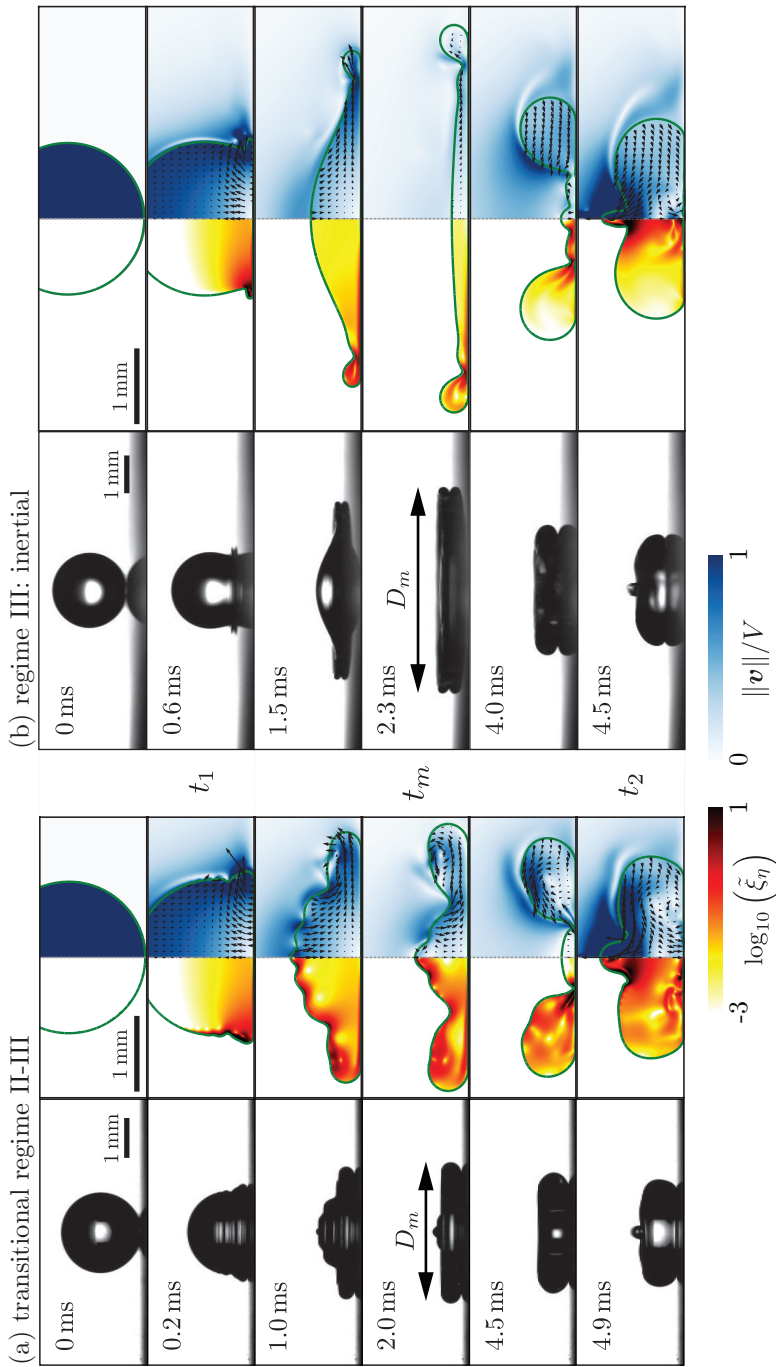


Figure 1.D.4: Snapshots of drop shape with time at different Weber numbers,  $We = (a) 20 (b) 80$ .

thickness in the central region remains the same (see 4.5 ms, [? ]). Then, the thickening retracting flow converges and collides at the film center to form an upward jet to result in  $F_2$ , as shown at 4.9 ms.

Based on the above results, we gain the following insight. For small  $We$  (figure 1.D.4a,  $We = 20$ ), the drop attains  $D_m$  (at time  $t_m$ ) before its apex descends to its lowest level (at time  $\sim D/V$ ), leading to a puddle-shaped drop [? ]. This observation indicates that at  $t_2$ , a competition exists between two flows in the central region of the drop, respectively, coming from the rim and the drop apex. However, for large  $We$  (figure 1.D.4b,  $We = 80$ ), the drop apex attains its lowest level before  $t_m$ , so the drop has a pizza shape [? ? ]. Equating the two timescales together, one obtains a crossover Weber number  $We^* = 25$ , which is close to the value 30 observed in our work. Alternatively, equating the two scaling relations in equation (1.2) gives a more accurate estimate of the crossover Weber number as  $We^* = 29.7$ .

### 1.D.3 Regime IV: drop splashing

The main text reported differences between the experimental and numerical observations in regime IV. Here, we further delve into this discrepancy to identify the reasons behind it (figure 1.D.5). At high impact velocities ( $We = 225$  in figure 1.D.5), splashing occurs in the experiments [? ]. At such high  $We$ , the surrounding gas atmosphere destabilizes the rim, breaking it [? ? ]. The limit for splashing observed in this work ( $We \geq 100$ , see figure 1.4) is in agreement with the predictions in previously predicted works of [? ? ? ] (see figure 4).

In regime IV, a part of kinetic and surface energies are lost due to the formation of satellite drops (figure 1.D.5b), resulting in diminishing  $\tilde{F}_2$  in the experiments (Fig 1.D.5(a)). Obviously, such azimuthal instability is absent in the simulations (axisymmetric by definition), which leads to a better flow-focusing at the center. Indeed, [? ] were able to simulate cases with  $We$  as high as 1000 without breakup. Consequently, equation (1.3) holds only for the simulations in regime IV and not for the experiments. Notice that the experimental and numerical  $F(t)$  magnitudes only disagree near  $t = t_2$ . Further, the time at which the second peak is reached is still at  $t_2 \approx 0.44\tau_{p\gamma}$ , as explained in the main text. For future work, we suggest that one could also experimentally probe  $F_2$  in this regime by suppressing the azimuthal instability (for instance, by reducing the atmospheric pressure [? ]).

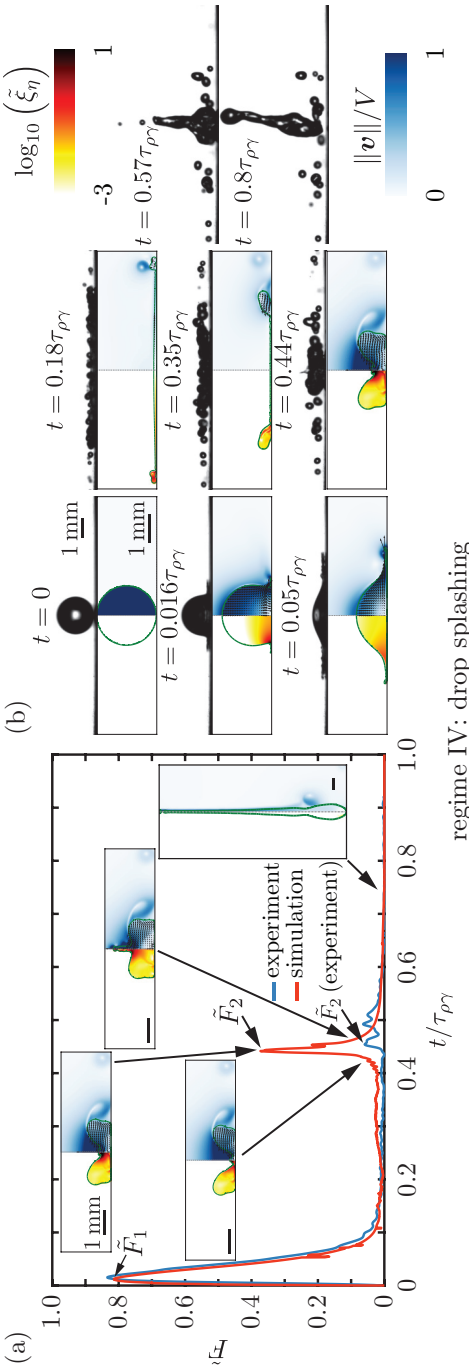


Figure 1.D.5: Drop impact on the superhydrophobic surface at a high Weber number,  $We = 225$ . (a) Evolution of the transient impact force. (b) Snapshots of the corresponding drop geometry in the spreading and recoiling stages. Notice that the experimental and numerical  $F(t)$  magnitudes only disagree near  $t = t_2$ . Further, the time at which the second peak is reached is still at  $t_2 \approx 0.44\tau_{\rho\gamma}$ , as explained in the main text. The left part of each numerical snapshot shows the dimensionless viscous dissipation function,  $\tilde{\xi}_\eta$  on a  $\log_{10}$  scale and the right part shows the velocity field magnitude normalized with the impact velocity,  $\|\mathbf{v}\|/V$ . The black velocity vectors are plotted in the center of mass reference frame of the drop to clearly elucidate the internal flow.

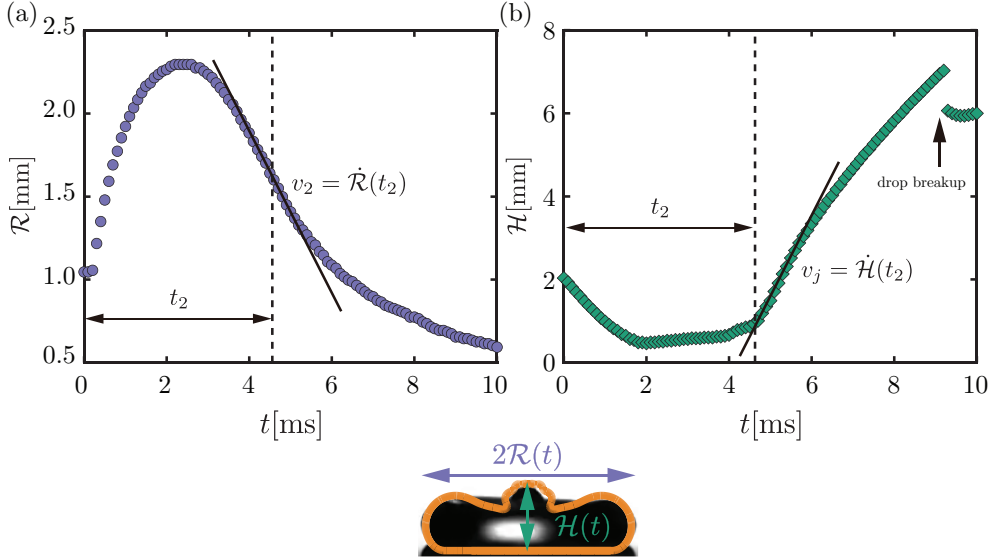


Figure 1.E.1: Experimental time evolution of (a) spread radius  $\mathcal{R}(t)$  and (b) the drop height  $\mathcal{H}(t)$ . Inset illustrates the drop geometry. The retraction velocity  $v_2 = \dot{\mathcal{R}}(t_2)$  and the jet velocity  $v_j = \dot{\mathcal{H}}(t_2)$  are represented by the slopes of the solid lines at  $t_2$  in (a) and (b), respectively. Here,  $We = 40$ .

## 1.E Calculation of the jet and retraction characteristics

### 1.E.1 Experiments

In this section, we illustrate how to extract  $v_2$  and  $v_j$  from the experiments. As an example, we choose  $We = 40$ . As shown in figure 1.E.1, we first track the instantaneous values of the width  $2\mathcal{R}(t)$  (figure 1.E.1a) and the height  $\mathcal{H}(t)$  (figure 1.E.1b) of the drop. We observe that just after the impingement, the drop height decreases with a constant velocity [? ? ] until the inertial shock propagates throughout the drop. As time progresses,  $\mathcal{R}(t)$  and  $\mathcal{H}(t)$  respectively reach their maximum and minimum values simultaneously (at  $t_m \approx 2.5$  ms). Moving forward in time,  $\mathcal{R}(t)$  decreases, whereas  $\mathcal{H}(t)$  increases linearly until  $t_2$ . After this moment, we observed a sharp increase of  $\mathcal{H}(t)$  until the drop breaks into the base drop and a small droplet (see the insets in figure 1.2a of the main text). We define the recoiling velocity  $v_2$  of the drop and the jet velocity  $v_j$  as:

$$v_2 = \dot{\mathcal{R}}(t_2) = \left. \frac{d\mathcal{R}(t)}{dt} \right|_{t_2}, \quad (1.15)$$

$$v_j = \dot{\mathcal{H}}(t_2) = \left. \frac{d\mathcal{H}(t)}{dt} \right|_{t_2}. \quad (1.16)$$

As shown in figure 1.E.1(a),  $v_2 = \dot{\mathcal{R}}(t_2)$  is obtained by a linear fitting (black line) to the experimental data around  $(t_2, \mathcal{R}(t_2))$ . Similarly, as shown in figure 1.E.1(b),  $v_j = \dot{\mathcal{H}}(t_2)$  is obtained by a linear fitting (black line) to the experimental data around  $(t_2, \mathcal{H}(t_2))$ . Note that in the experiments, we can only measure the maximum height of the drop. Consequently, when the rim thickness exceeds the drop's height,  $\mathcal{H}$  identifies the height of the rim (particularly for  $t < t_m$ ). So, we use the datapoints after  $t = t_2$  to calculate the jet velocity. Nonetheless, the jet velocity  $v_j$  extracted at  $t = t_2^+$  from the experiments are consistent very well with our simulation (where we can precisely calculate the jet velocity, see § 1.E.2), as well as the results obtained by [?], as discussed in § 1.E.3.

## 1.E.2 Simulations

To characterize the jet, we track the interfacial location (or height of the drop,  $\mathcal{H}(t)$ ) at the axis of symmetry ( $r = 0$ ). Similarly, to characterize retraction, we track the radial extent of the drop ( $2\mathcal{R}(t)$ ). Further,  $\dot{\mathcal{H}} = d\mathcal{H}/dt$  measures the velocity of this jet, and  $\dot{\mathcal{R}} = d\mathcal{R}/dt$  accounts for the retraction velocity. Figure 1.E.2 shows the temporal variation of  $\dot{\mathcal{H}}$  (panel i) and  $\dot{\mathcal{R}}$  (panel ii) for two representative Weber numbers,  $We = 9$  (panel a) and 100 (panel b). As the drop impacts, the top of the drop keeps moving with a constant velocity ( $\dot{\mathcal{H}} \approx V$ ) [? ?], consistent with our experiments. However, during this period, the radial velocity magnitude increases to a maximum and then decreases to zero at the instant of maximum spreading.

For low to moderate Weber number impacts ( $We = 9$  in figure 1.E.2a), the pyramidal morphology result in capillary oscillations aiding the flow focusing in the retraction phase. Consequently, both the normal force ( $F$ ) and the jet velocity ( $\dot{\mathcal{H}}$ , figure 1.E.2a-i) reach the maxima simultaneously at  $t = t_2$ . Further, the retraction velocity (figure 1.E.2a-ii) show oscillations due to capillary waves.

On the other hand, for high Weber number impacts ( $We = 100$  in figure 1.E.2b), the jet velocity is minimum at the instant of maximum spreading.

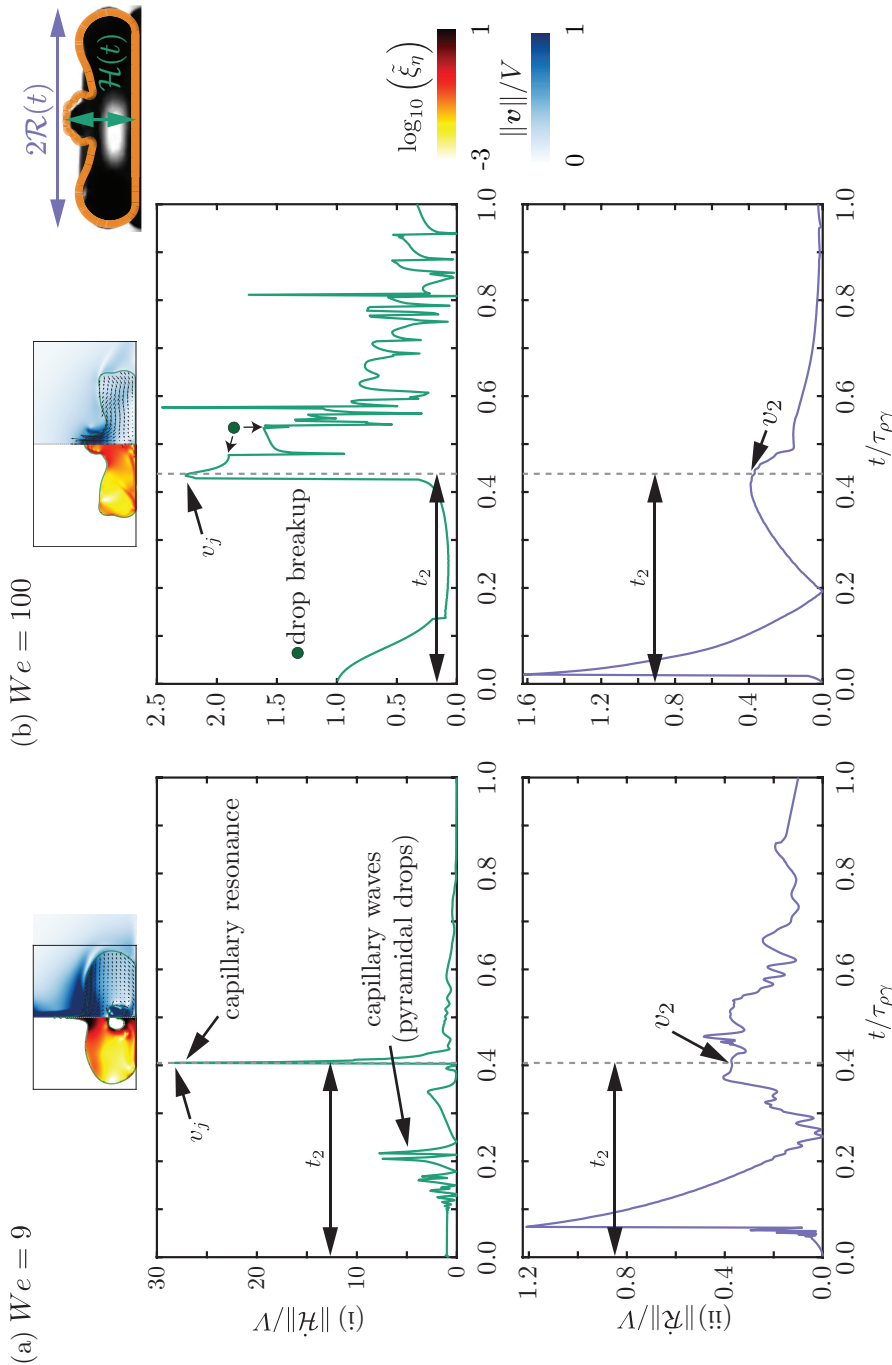


Figure 1.E.2: Calculation of the (i) jet velocity ( $v_j$ ) and (ii) retraction velocity ( $v_2$ ) for Eq. (2) of the main manuscript for two representative cases:  $We = (a) 9$  and (b) 100. Inset illustrates the drop geometry where  $\mathcal{H}$  is the height of the drop at the axis of symmetry and  $2R$  is its radial extent. The jet velocity is  $v_j = \dot{\mathcal{H}}(t_2)$  and the retraction velocity is  $v_2 = \dot{R}(t_2)$ . Notice that the time at which second peak is reached still scales with the inertia-capillary timescale  $t_2 \sim \tau_{\rho\gamma}$ , as described in the main text, irrespective of the  $We$  ( $t_2 = 0.405\tau_{\rho\gamma}$  for  $We = 9$ , and  $t_2 = 0.437\tau_{\rho\gamma}$  for  $We = 100$ ).

Then, Taylor-Culick type retraction occurs increasing the retraction velocity to a maximum which then decreases due to finite size of the drop [? ? ? ]. During this retraction phase, flow focusing and asymmetry provided by the substrate lead to a sudden increase in the jet velocity (figure 1.E.2b-i) that is immediately followed by occurrence of the second peak in the transient force profile (at  $t_2$ ). The retraction velocity at this instant is very close to its maximum temporal value (figure 1.E.2b-ii).

For both cases, notice that the time at which second peak is reached still scales with the inertio-capillary timescale  $t_2 \sim \tau_{\rho\gamma}$ , as described in the main text, irrespective of the  $We$  ( $t_2 = 0.405\tau_{\rho\gamma}$  for  $We = 9$ , and  $t_2 = 0.437\tau_{\rho\gamma}$  for  $We = 100$ ).

In summary,

$$v_j = \dot{\mathcal{H}}(t_2) \quad (1.17)$$

$$v_2 = \dot{\mathcal{R}}(t_2). \quad (1.18)$$

Lastly, we can also characterize the maximum lateral extent  $D_2$  of the drop at the instant  $t_2$  of second peak in the normal reaction force  $F_2$  as

$$D_2 = 2\mathcal{R}(t_2), \quad (1.19)$$

in both experiments as well as simulations.

### 1.E.3 Results

We will devote the rest of this appendix to relate the different flow properties in equation (1.3) (also see figure 1.E.3a) to the control parameter, i.e., the impact Weber number  $We$ . For the transitional regime II-III ( $12.6 < We < 30$ ), at the moment of second peak, the dimensionless diameter ( $\tilde{D}_2$ ) and the dimensionless drop retraction velocity ( $\tilde{v}_2$ ) are independent of the impact Weber number  $We$  (figures 1.E.3b, c). Further, the jet velocity decreases with increasing Weber number following  $\tilde{v}_j = v_j/V \sim 1/We$  (figure 1.E.3d). This decrease is consistent with the data extracted from ? ]. Substituting these in equation (1.3), one obtains  $\tilde{F}_2 \sim 1/We$ . However, the prefactor that best fits the experimental and numerical data in equation (1.2) is much larger than order 1, which may be caused by the enhanced flow and momentum focusing due to both capillary waves and drop retraction.

For regime III ( $30 < We < 100$ ), there is a slight increase in  $\tilde{D}_2$  (figure 1.E.3b) but it is still best represented by a plateau. Furthermore, with

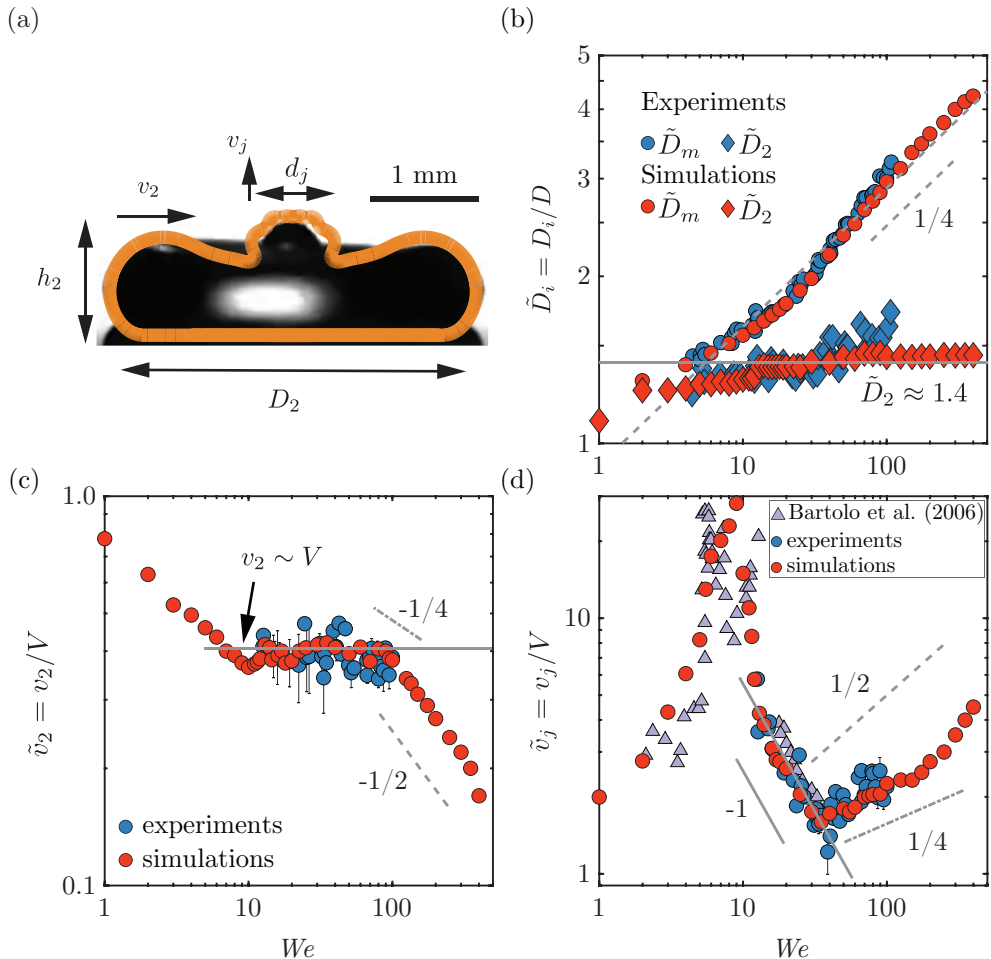


Figure 1.E.3: (a) Drop geometry at  $t_2$  for  $We = 40$  (along with the drop contour from numerics in orange) to illustrate the drop spreading diameter  $D_2$ , drop height  $h_2$ , retraction velocity  $v_2$ , jet diameter  $d_j$  and jet velocity  $v_j$ . (b) Variation of the dimensionless spreading diameter at  $t_m$  and  $t_2$  (given by  $\tilde{D}_{max} = \tilde{D}(t_m)$  and  $\tilde{D}_2 = \tilde{D}(t_2)$ , respectively). The gray dotted and solid lines represent  $\tilde{D}_{max} \sim We^{1/4}$  and  $\tilde{D}_2 \approx 1.4$ , respectively. (c) Variation of drop retraction velocity  $\tilde{v}_2$  at  $t_2$  with  $We$ . The gray solid line represents  $v_2 \sim V$ . The gray dotted and dashed-dotted lines correspond to  $We^{-1/2}$  and  $We^{-1/4}$ , respectively, and are meant only as guides to the eye. (d) Variation of the (non-dimensionalized) jet velocity  $\tilde{v}_j = v_j/V$  with  $We$ . The data from [Bartolo et al. (2006)] are also shown in the same panel. The gray solid line represents  $\tilde{v}_j \sim We^{-1}$ . The gray dotted and dashed-dotted lines correspond to  $We^{1/2}$  and  $We^{1/4}$ , respectively, and are meant only as guides for the eye.

increasing  $We$ ,  $\tilde{v}_2$  decreases whereas  $\tilde{v}_j$  increases (figures 1.E.3c,d). We have shown gray lines as guides to the eye to represent these trends. However, due to limited range of  $We$ , we refrain from claiming any scaling relations here. Coincidentally, these changes in  $\tilde{D}_2$ ,  $\tilde{v}_2$ , and  $\tilde{v}_j$  compensate each other such that equation (1.3) still holds. Consequently, the second peak force scales with the inertial pressure force  $F_2 \sim \rho_d V^2 D^2$  (equation (1.2)).

Alternatively, we can use the expressions for the amplitude of the second peak of force between the drop and the substrate to predict the velocity of the Worthington jet. For  $We \gg 1$ , the drop forms a thin sheet at the instant of maximum spreading ( $t = t_m$ , see figures 1.D.4b and 1.D.5). This sheet retracts following Taylor-Culick type retraction at low Ohnesorge numbers ( $Oh \ll 1$ ). As a result, the retraction velocity scale can be given as [? ? ]:

$$v_2 \sim \sqrt{\frac{\gamma}{\rho_d h_2}}, \quad (1.20)$$

where,  $\gamma$  and  $\rho_d$  are the surface tension coefficient and density of the liquid drop, respectively. Further,  $v_2$  is the retraction velocity at  $t = t_2$  and  $h_2$  is the height of the drop at that instant which is related to the spreading diameter following volume conservation as  $h_2 \sim D^3/D_2^2$ . Substituting this expression in equation (1.20) and normalizing with  $V$ , we get

$$\tilde{v}_2 \sim D_2 \sqrt{\frac{\gamma}{\rho_d V^2 D^3}} = \frac{\tilde{D}_2}{\sqrt{We}}. \quad (1.21)$$

The finite size of the retracting drop may account for the deviations from equation (1.21) in figures 1.E.3(b,c) [? ? ]. Further, using  $\tilde{F}_2 \sim \tilde{v}_2 \tilde{v}_j / \tilde{D}_2 \sim \mathcal{O}(1)$  for  $We \gg 1$ , we obtain

$$\tilde{v}_j \sim \sqrt{We}. \quad (1.22)$$

Unfortunately, we cannot confirm the validity of this scaling behavior in figure 1.E.3(d) due to a limited range of  $We$  as mentioned above. For completeness, in figure 1.E.3(b), we also show the maximum spreading diameter from our experiments and simulations are in a remarkable agreement. We refer the readers to [? ? ? ] for further discussions on the influence of  $We$  on the maximum spreading diameter.

### 1.E.4 Outlook on the scaling relations

In this section and figure 1.E.3, we probe several scaling behaviors in an attempt to relate the internal flow characteristics, i.e., the jet and retraction velocities, to the impact Weber number. However, verifying the predicted scaling behaviors requires a larger range of Weber numbers that we do not study due to experimental and numerical limitations. For example, at very high-velocity impacts, the drop splashes and breaks into many satellite droplets in the experiments [? ]. For future work, we suggest that one could experimentally probe this regime by suppressing the azimuthal instability (for instance, by reducing the atmospheric pressure [? ]). However, even in such a scenario, at very high impact velocities ( $We \gg 1$ ), the substrate roughness may play a role in both drop spreading and retraction [? ]. In numerical simulations, one can probe this regime by using drops that are slightly more viscous than water, as done by [? ]. However, such a study is numerically costly for water drops impacting at very large  $We$  due to the separation of length scales between the initial diameter of the drop and the very thin lamella during spreading. Furthermore, the interfacial undulations (traveling capillary waves) further restrict both the spatial and temporal resolutions.

## 1.F Code availability

All codes used in this chapter are permanently available at [? ].

## 1.G Supplemental movies

These supplemental movies are available at [? ].

SM1: The evolution of the transient force of a water drop impacting on the superhydrophobic surface at a moderate Weber number  $We = 40$  (corresponding to  $D = 2.05$  mm and  $V = 1.20$  m/s), with simultaneous drop geometry recorded experimentally at 10,000 fps with the exposure time of 1/20,000 s. The left part of the numerical video shows the dimensionless viscous dissipation function on a  $\log_{10}$  scale and the right part shows the velocity field magnitude normalized with the impact velocity.

SM2: The evolution of the transient force of a water drop impacting on the superhydrophobic surface at a low Weber number  $We = 2$  (Regime I: capillary), with simultaneous drop geometry evolution. The left part of

the numerical video shows the dimensionless viscous dissipation function on a  $\log_{10}$  scale and the right part shows the velocity field magnitude normalized with the impact velocity.

- SM3: The evolution of the transient force of a water drop impacting on the superhydrophobic surface at Weber number  $We = 9$  (corresponding to  $D = 2.76\text{ mm}$  and  $V = 0.49\text{ m/s}$ ), with simultaneous drop geometry recorded experimentally at 10,000 fps with the exposure time of 1/50,000 s. The ultra-thin and fast singular jet is reminiscent of the hydrodynamic singularity. The left part of the numerical video shows the dimensionless viscous dissipation function on a  $\log_{10}$  scale and the right part shows the velocity field magnitude normalized with the impact velocity.
- SM4: Boundaries of the singular jet regime: the evolution of the transient force of a water drop impacting on the superhydrophobic surface at three representative Weber numbers in regime II,  $We = 5$ ,  $We = 9$ , and  $We = 12$ , with simultaneous drop geometry evolution. The left part of the numerical video shows the dimensionless viscous dissipation function on a  $\log_{10}$  scale and the right part shows the velocity field magnitude normalized with the impact velocity.
- SM5: Contact force and pressure field during drop impact on the superhydrophobic surface in the singular Worthington jet regime,  $We = 9$ . Simulation shows the pressure field  $p$  normalized by the inertial pressure  $\rho_d V^2$  on the left and the magnitude of velocity field  $\|\mathbf{v}\|$  normalized by the impact velocity  $V$  on the right in the side view images and pressure field in the bottom view images.
- SM6: The evolution of the transient force of a water drop impacting on the superhydrophobic surface at a high Weber number  $We = 225$  (drop splashing regime, corresponding to  $D = 2.05\text{ mm}$  and  $V = 2.83\text{ m/s}$ ), with simultaneous drop geometry recorded experimentally at 10,000 fps with the exposure time of 1/20,000 s. The left part of the numerical video shows the dimensionless viscous dissipation function on a  $\log_{10}$  scale and the right part shows the velocity field magnitude normalized with the impact velocity.
- Bonus: Conference (Physics@Veldhoven 2022) talk titled “How much force is required to play ping-pong with water droplets?” presenting the results from this chapter.

chapter 1: impact forces of water drops falling  
on superhydrophobic surfaces



source code



supplemental movies

## Chapter 2

# When does a drop stop bouncing?<sup>o</sup>

2

As a liquid drop impacts a non-wetting substrate in presence of a gravitational field, it spreads while converting the initial kinetic energy into surface energy to reach a maximum extent which only weakly depends on the initial impact velocity. At this stage, the drop stops and then recoils following a capillary-driven Taylor-Culick type retraction, gaining kinetic energy as its surface area decreases. This drop recoil creates a radially symmetric flow inside the drop. The presence of the substrate creates an asymmetry and directs this flow in the upward direction against gravity. Throughout these stages, viscous dissipation enervate the internal momentum of the flow. Eventually, at the end of the retraction stage, if the upward flow is strong enough to overcome gravity, the drop bounces off the non-wetting substrate. In this article, we investigate how viscous stresses and gravity conspire against capillarity to inhibit the drop to bounce off non-wetting substrates. Drawing an analogy with the case of coalescence-induced jumping of two identical drops, we propose the criterion  $Oh_{d,c} + Bo_c = 1$  (i.e., sum of the critical drop Ohnesorge and Bond numbers being one), for this bouncing to non-bouncing transition and check its validity by employing axially symmetric direct numerical simulations. We also delve into the two asymptotes ( $Oh_{d,c} = 1$  for  $Bo \ll 1$ , and  $Bo_c = 1$  for  $Oh_d \ll 1$ ) to demystify the mechanisms associated to this transition and analyze the salient characteristics of the drop impact process, including the contact time, coefficient of restitution, and energy budgets.

---

<sup>o</sup>In preparation as: **Vatsal Sanjay**, Pierre Chantelot, and Detlef Lohse, *When does a drop stop bouncing?*, J. Fluid Mech. Simulations are done by Sanjay; analysis and writing by Sanjay and Chantelot; and supervision by Lohse. Proofread by everyone.

## 2.1 Introduction

Drop impacts have intrigued scientists ever since Leonardo da Vinci sketched a water drop splashing onto a sheet of paper in the margin of folio 33r in Codex Hammer/Leicester (1506 – 1510) [? ]. In particular, the striking patterns created by drop fragmentation, at high impact velocity, have attracted attention [? ? ? ? ]. Lower velocity impacts, although they do not cause drops to shatter, also give rise to a rich variety of phenomena [? ? ? ? ? ? ]. The rebound of drops on non-wetting substrates may be one of the most fascinating of such interactions [? ? ? ].

Upon impact, the liquid first spreads [? ? ] until it reaches its maximal extent [? ? ? ? ]. It then recoils, following a Taylor-Culick type retraction parallel to the substrate [? ? ? ? ? ? ], and ultimately bounces off in an elongated shape perpendicular to the substrate [? ? ? ]. Furthermore, throughout these stages, viscous dissipation enervate the internal momentum of the flow and can even suppress bouncing [? ? ? ].

Such rebounds abound in nature, as non-wetting surfaces provide plants and animals a natural way to keep dry [? ? ], and are relevant in many industrial processes [? ], such as inkjet printing [? ], cooling applications [? ? ? ], pesticides application [? ? ], and criminal forensics [? ]. In some applications, it is pertinent that drops ricochet off the surface, such as self-cleaning [? ], keeping clothes dry [? ], and anti-fogging surfaces [? ]. However, in most applications, bouncing must be suppressed, for example in inkjet printing [? ], cooling applications [? ? ? ], pesticides application [? ], and criminal forensics [? ].

Therefore, it is natural to wonder when does a drop stop bouncing? On one hand, ? ] found that heavy drops, i.e., drops larger than their gravito-capillary length  $l_c = \sqrt{\gamma/\rho_d g}$ , where  $\gamma$  is the drop-air surface tension coefficient,  $\rho_d$  is the density of the drop and  $g$  is the acceleration due to gravity, cannot bounce. On the other hand, ? ] showed that there exists a critical viscosity, two orders of magnitude higher than that of water, beyond which aqueous drops do not bounce either, irrespective of their impact velocity. I.e., both gravity and viscosity counteract the bouncing. In this chapter, we investigate and quantify how exactly gravity and viscous stresses conspire against capillarity to prevent drops from bouncing off non-wetting substrates, using direct numerical simulations. We focus on evidencing the mechanisms of bouncing inhibition, and exhibit a simple criterion delineating the bouncing to non-bouncing transition through an analogy with coalescence-induced drop jumping [? ? ? ].

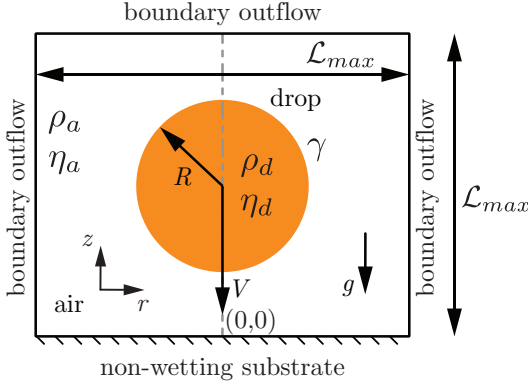


Figure 2.2.1: Axi-symmetric computational domain used to study impact of a drop with radius  $R$  and velocity  $V$  on an ideal non-wetting substrate. The subscripts  $d$  and  $a$  denote the drop and air, respectively, to distinguish their material properties, namely, density  $\rho$  and viscosity  $\eta$ . The drop-air surface tension coefficient is  $\gamma$  and  $g$  denotes the acceleration due to gravity. The gray dashed-dotted line represents the axis of symmetry,  $r = 0$ . Boundary outflow is applied at the top and side boundaries (tangential stresses, normal velocity gradient, and ambient pressure are set to zero). The domain boundaries are far enough not to influence the drop impact process ( $\mathcal{L}_{max} \gg R$ ).

The chapter is organized as follows: § 2.2 discusses the governing equations employed in this work. § 2.3 explores the bouncing to non-bouncing transition and formulates a criterion for the inhibition of bouncing based on first principles followed by § 2.4 which delves into the limiting cases of this criterion. The paper ends with conclusions and an outlook on future work in § 2.5.

## 2.2 Governing equations

We employ direct numerical simulations to study the drop impact process (figure 2.2.1), using the free software program Basilisk C [? ] that employs the geometric volume of fluid (VoF) method for interface reconstruction [? ]. For an incompressible flow, the mass conservation requires the velocity field to be divergence-free (tildes denote dimensionless quantities throughout this manuscript),

$$\tilde{\nabla} \cdot \tilde{v} = 0, \quad (2.1)$$

where we non-dimensionalize the velocity field with the inertio-capillary velocity  $V_{\rho\gamma} = \sqrt{\gamma/\rho_d R}$ , where  $\gamma$ ,  $\rho_d$  and  $R$  are the surface tension coefficient between the drop and air, density of the drop, and its radius, respectively, see figure 2.2.1). We can further non-dimensionalize all lengths with the radius of the drop  $R$ , time with the inertio-capillary timescale  $\tau_{\rho\gamma} = R/V_{\rho\gamma} = \sqrt{\rho_d R^3/\gamma}$ , and pressure with the capillary pressure,  $p_\gamma = \gamma/R$ , to write the momentum equation as

$$\frac{\partial(\tilde{\rho}\tilde{\mathbf{v}})}{\partial\tilde{t}} + \nabla(\tilde{\rho}\tilde{\mathbf{v}}\tilde{\mathbf{v}}) = -\tilde{\nabla}\tilde{p}' + \tilde{\nabla}\cdot(2Oh\tilde{\mathcal{D}}) + \tilde{\mathbf{f}}, \quad (2.2)$$

where the deformation tensor,  $\mathcal{D}$  is the symmetric part of the velocity gradient tensor ( $= (\nabla\mathbf{v} + (\nabla\mathbf{v})^\text{T})/2$ ). Note that axial symmetry is assumed throughout this chapter. The Ohnesorge number  $Oh$  (ratio of inertio-capillary to inertio-viscous time scales) and the dimensionless density  $\tilde{\rho}$  are written using the one-fluid approximation [? ?] as

$$Oh = \Psi Oh_d + (1 - \Psi) Oh_a, \quad (2.3)$$

$$\tilde{\rho} = \Psi + (1 - \Psi) \frac{\rho_a}{\rho_d}, \quad (2.4)$$

where  $\Psi$  is the VoF tracer ( $= 1$  for drop and  $0$  otherwise), and  $\rho_a/\rho_d$  is the air–drop density ratio. Here,

$$Oh_d = \frac{\eta_d}{\sqrt{\rho_d\gamma R}} \quad \text{and} \quad Oh_a = \frac{\eta_a}{\sqrt{\rho_d\gamma R}} \quad (2.5)$$

are the Ohnesorge numbers based on the viscosities of the liquid drop and of air, respectively.

To minimize the influence of the surrounding medium, we keep  $\rho_a/\rho_d$  and  $Oh_a$  fixed at  $10^{-3}$  and  $10^{-5}$ , respectively. Lastly,  $\tilde{p}'$  denotes the reduced pressure field,  $\tilde{p}' = \tilde{p} + Bo\tilde{\rho}\tilde{z}$ , where,  $\tilde{p}$  and  $Bo\tilde{\rho}\tilde{z}$  represent the mechanical and the hydrostatic pressures, respectively. Here, the Bond number  $Bo$  compares gravity to the surface tension force and is given by

$$Bo = \frac{\rho_d g R^2}{\gamma}, \quad (2.6)$$

and  $\tilde{z}$  is the distance away from the non-wetting substrate (see figure 2.2.1). Using this reduced pressure approach ensures an exact hydrostatic balance as described in [? ? ]. This formulation requires an additional singular body force at the interface such that  $\tilde{\mathbf{f}}$  takes the form [? ],

$$\tilde{\mathbf{f}} \approx \left( \tilde{\kappa} + Bo \left( 1 - \frac{\rho_a}{\rho_d} \right) \tilde{z} \right) \tilde{\nabla} \Psi \quad (2.7)$$

where the first and second terms on the right-hand side are the local capillary and hydrostatic pressure jumps across the interface, respectively with  $\tilde{\kappa}$  the interfacial curvature calculated using the height-function approach [? ].

Figure 2.2.1 shows the axi-symmetric computational domain where we solve the equations discussed above. Initially, we assume that the drop is spherical and that it impacts with a dimensionless velocity,  $\tilde{V} = V/V_{\rho\gamma} = \sqrt{We}$ , where the impact Weber number

$$We = \frac{\rho_d R V^2}{\gamma} \quad (2.8)$$

is the ratio of the inertial pressure during impact to the capillary pressure. We refer the readers to § 1.B, and [? ? ? ? ? ] for details of the computational method employed in this work.

## 2.3 Bouncing inhibition

We investigate the behavior of drops impacting on non-wetting substrates by exploring the influence of the following dimensionless parameters: the Weber number  $We = \rho R V^2 / \gamma$ , the Bond number  $Bo = \rho_d g R^2 / \gamma$ , and the Ohnesorge number  $Oh_d = \eta_d / \sqrt{\rho_d \gamma R}$ . In Figure 2.3.1, we evidence the bouncing to non-bouncing transition in the parameter space spanned by the Ohnesorge and Bond numbers for several fixed Weber numbers. We extract several key pieces of information from this regime map.

- (i) The Weber number has a small influence on the transition between the bouncing and non-bouncing regime in the range probed in this study,  $We = 1 - 50$ , consistent with [? ] for the bouncing inhibition of viscous drops (also see appendix 2.B).

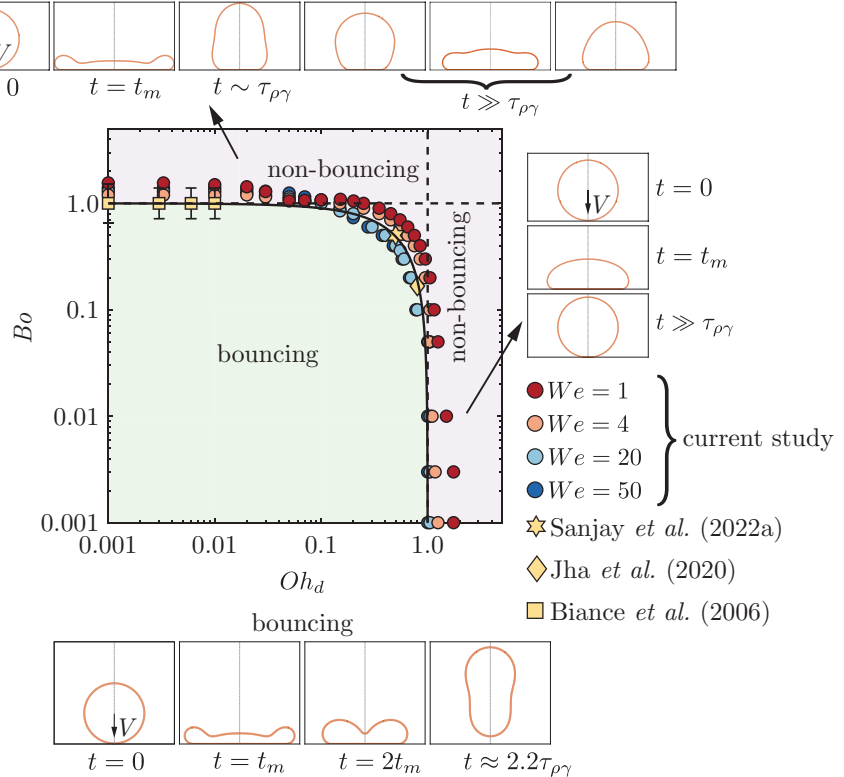


Figure 2.3.1: Regime map in terms of the Bond number  $Bo = \rho_d g R^2 / \gamma$  and the drop Ohnesorge number  $Oh_d = \eta_d / \sqrt{\rho_d \gamma R}$ , marking the bouncing and non-bouncing regimes identified in this work. The data points represent the transition between bouncing and non-bouncing regimes at different Weber numbers  $We$ , and the insets illustrate typical cases in these regimes. The yellow data points are extracted from the literature for comparison. The solid black line delineates the theoretical prediction of this transition (equation (2.14)). Lastly, the black dotted vertical and horizontal lines mark the limiting cases,  $Oh_{d,c} = 1$  and  $Bo_c = 1$ , respectively. See also supplementary movie 1.

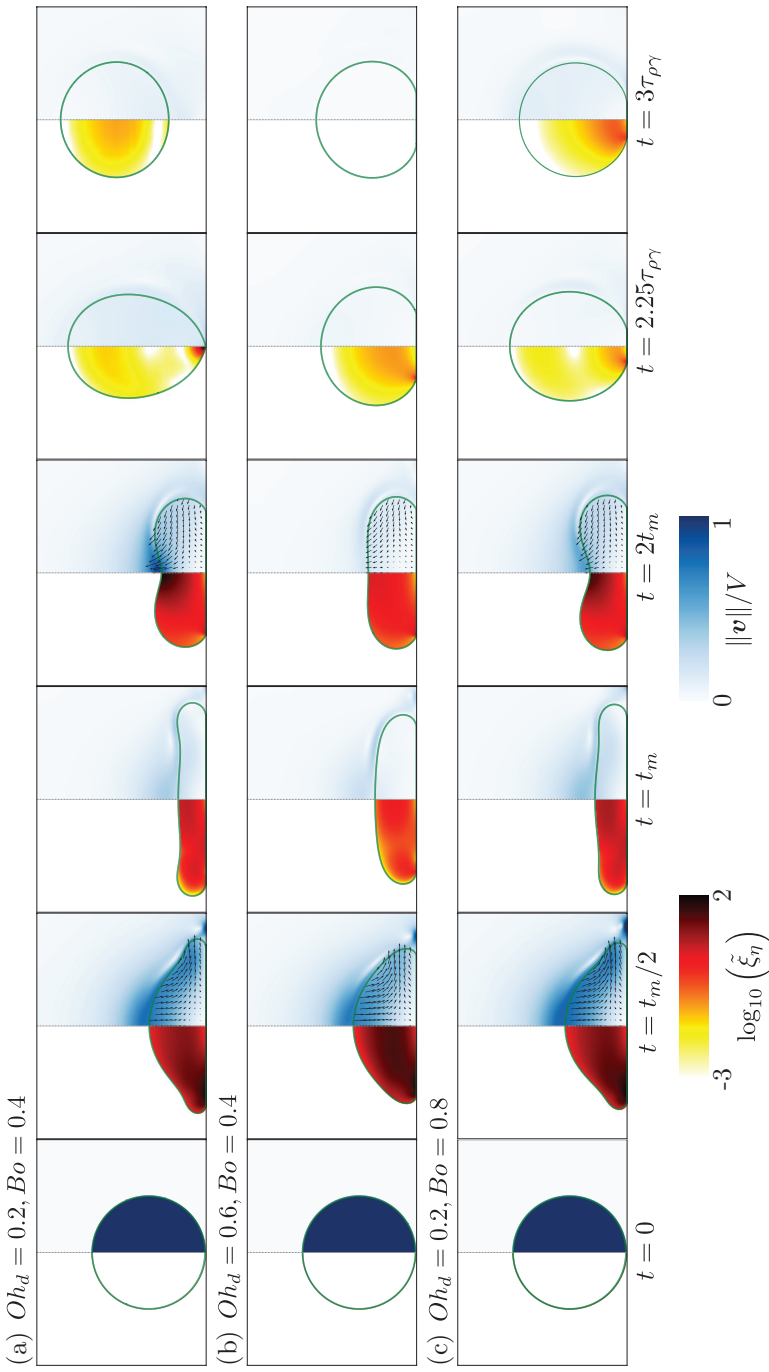


Figure 2.3.2: Three representative cases away from the two asymptotes: direct numerical simulations snapshots illustrating the drop impact dynamics for  $(Oh_d, Bo) = (0.2, 0.4)$  (a),  $= (0.6, 0.4)$  (b), and  $= (0.2, 0.8)$  (c). The left hand side of each numerical snapshot shows the dimensionless viscous dissipation function  $\tilde{\xi}_\eta = 2 Oh(\tilde{\mathcal{D}} : \tilde{\mathcal{D}})$  on a  $\log_{10}$  scale to identify regions of maximum dissipation (black). The right hand side shows the magnitude of the velocity field normalized by the initial impact velocity,  $V$ . The black velocity vectors are plotted in the center of mass reference frame of the drop to clearly show the internal flow. For all the cases shown here, the impact Weber number is  $We = 20$ . See also supplementary movie SM2.

- 2**
- (ii) We recover the two limiting cases of non–bouncing (see insets of figure 2.3.1): drops smaller than their visco-capillary length, (i.e.,  $R < \eta_d^2/\rho_d\gamma$ ) stop bouncing due to viscous dissipation [? ], while those larger than their gravito-capillary length, (i.e.,  $R > \sqrt{\gamma/\rho_d g}$ ) cannot bounce due to their weight [? ]. We elaborate on the mechanisms of rebound inhibition in these two non–bouncing regimes in § 2.4.
  - (iii) Experiments performed with millimeter–sized drops of water or silicone oil do not lie on either asymptote, suggesting that both the effect of viscosity and gravity need to be taken into account to predict the bouncing to non–bouncing transition.

In this section, we focus on situations where bouncing is prevented by both viscous and gravitational effects (i.e.,  $Bo < 1$  and  $Oh_d < 1$ ). Figure 2.3.2 shows snapshots illustrating three representative cases lying in this region of the parameter space for  $We = 20$ . Each snapshot displays three pieces of information: (i) the position of the liquid–air interface, (ii) the dimensionless rate of viscous dissipation per unit volume (i.e., the viscous dissipation function, left panel), and (iii) the magnitude of the velocity field normalized by the impact velocity (right panel). For  $Oh_d = 0.2$  and  $Bo = 0.4$  (figure 2.3.2a), the drop undergoes typical rebound dynamics. The liquid first spreads radially up to  $t = t_m$ , when the maximum extent is reached [? ? ? ? ]. This stage is followed by liquid retraction [? ], parallel to the substrate, until the drop contracts ( $t = 2t_m$ ) and the motion becomes vertical [? ? ]. Finally, the drop leaves the substrate at  $t = 2.25\tau_{\rho\gamma}$  [? ? ].

Surprisingly, increasing  $Oh_d$  to 0.6, below the critical value reported by [? ], while keeping  $Bo = 0.4$  (figure 2.3.2b) prevents the rebound. The motion is damped before the drop can bounce off the substrate. Similarly, increasing  $Bo$  to 0.8, below the critical value reported by [? ], while fixing  $Oh_d = 0.2$  (figure 2.3.2c), also inhibits bouncing. Yet, the deposited liquid undergoes multiple oscillation cycles on the substrate before coming to rest (see the last snapshot  $t = 3\tau_{\rho\gamma}$ ).

In all three cases, the impact dynamics and flow in the drop are qualitatively similar until the maximum extent is reached at  $t = t_m$ . At this instant, the absence of internal flow suggests that the initial kinetic energy has either been converted into surface energy or lost to viscous dissipation, which occurs throughout the drop volume owing to  $Oh_d \sim \mathcal{O}(0.1)$  [? ]. Close to the bouncing to non–bouncing transition, the rebound can thus be understood as a process which converts an initial surface energy into kinetic energy, disen-

tangling the later stages of the rebound from the initial impact dynamics.

This observation prompts us to introduce an analogy with coalescence-induced jumping, in which an excess surface energy, gained during coalescence, is converted into upward motion of the liquid [? ]. The spread drop, at rest at  $t = t_m$ , reduces its surface area through a Taylor-Culick type retraction [? ], converting excess surface energy into kinetic energy. The capillary force driving this radially inwards flow is

$$F_\gamma \sim \gamma R. \quad (2.9)$$

Similarly as in coalescence-induced jumping of two identical drops, a dissipative force  $F_\eta \sim \Omega \eta_d \nabla^2 v$ , where  $\Omega$  is the volume of the drop and  $v$  is a typical radial flow velocity, opposes the capillarity driven flow [? ? ]. Taking  $v$  as  $V_{\rho\gamma}$  at leading order, the resistive viscous force scales as

$$F_\eta \sim \eta V_{\rho\gamma} R, \quad (2.10)$$

and the effective momentum converging in the radial direction reads

$$P_r \sim \int (F_\gamma - F_\eta) dt. \quad (2.11)$$

The asymmetry stemming from the presence of the substrate enables the conversion of the radially inward momentum to the upwards direction (figure 2.3.2,  $t = 2t_m$ ). Following [? ? ], we assume that the vertical momentum scales with the radial one such that  $P_v \sim P_r$ , allowing us to determine a criterion for the bouncing transition by balancing the rate of change of vertical momentum with the drop's weight  $F_g$

$$\frac{dP_v}{dt} = F_g \sim \rho_d R^3 g. \quad (2.12)$$

Using equations (2.9) – (2.11), we obtain

$$\gamma R - \eta V_{\rho\gamma} R \sim \rho_d R^3 g. \quad (2.13)$$

Lastly, substituting  $V_{\rho\gamma} = \sqrt{\gamma/\rho_d R}$ , and rearranging, we arrive at a criterion to determine the bouncing to non-bouncing transition as

$$Oh_{d,c} + Bo_c = 1, \quad (2.14)$$

which is independent of the impact Weber number  $We$ . In equation (2.14) and throughout the manuscript, the subscript  $c$  stands for ‘critical’. Equation (2.14) is the main equation of this chapter. In principle, the derivation of this equation only suggests  $\sim 1$  on the right hand side of equation (2.14) and not  $= 1$ , but as we will see from the limiting cases treated in § 2.4, the equality sign is justified.

We test the criterion in equation (2.14) for the bouncing and non-bouncing transition against data extracted from our direct numerical simulations and experiments from [? ? ? ]. In figure 2.3.1, the solid black line representing equation (2.14) is in excellent quantitative agreement with the data when viscous and gravitational effects conspire to inhibit bouncing, as well as in the two limiting regimes,  $Oh_{d,c} = 1$  for  $Bo \ll 1$  [? ], and  $Bo = 1$  for  $Oh_d \ll 1$  [? ] (black dotted lines). In the next section, we focus on evidencing the physical mechanisms leading to bouncing suppression in each of the two limiting case.

## 2.4 Limiting cases

### 2.4.1 How does a viscous drop stop bouncing?

We first investigate how viscous dissipation prevents drops much smaller than their gravito-capillary length (*i.e.* with  $Bo \ll 1$ ) from bouncing. In this regime, the transition criterion, equation (2.14), reduces to

$$Oh_{d,c} = 1. \quad (2.15)$$

We sweep across this asymptote by setting  $Bo = 0$  and systematically varying the drop Ohnesorge number,  $Oh_d$ . We characterize the rebound behavior by measuring the apparent contact time between the drop and the substrate  $t_c$  and the coefficient of restitution  $\varepsilon$ , that we define as  $\varepsilon = v_{cm}(t_c)/V$ , where  $v_{cm}(t_c)$  is the center of mass velocity at take-off. The determination of  $t_c$  and  $\varepsilon$  from the DNS is detailed in appendix 2.A. In figure 2.4.1, we plot the coefficient of restitution  $\varepsilon$  and the normalized contact time  $t_c/\tau_{\rho\gamma}$  as a function of  $Oh_d$  for Weber numbers ranging from 1 to 50. The effect of  $Oh_d$  on  $t_c$  and  $\varepsilon$  is markedly different.

On the one hand, the coefficient of restitution monotonically decreases from its inviscid, Weber dependent value  $\varepsilon_0$  with increasing  $Oh_d$ , until a critical Ohnesorge number  $Oh_{d,c}$ , of order one, marking bouncing inhibition is

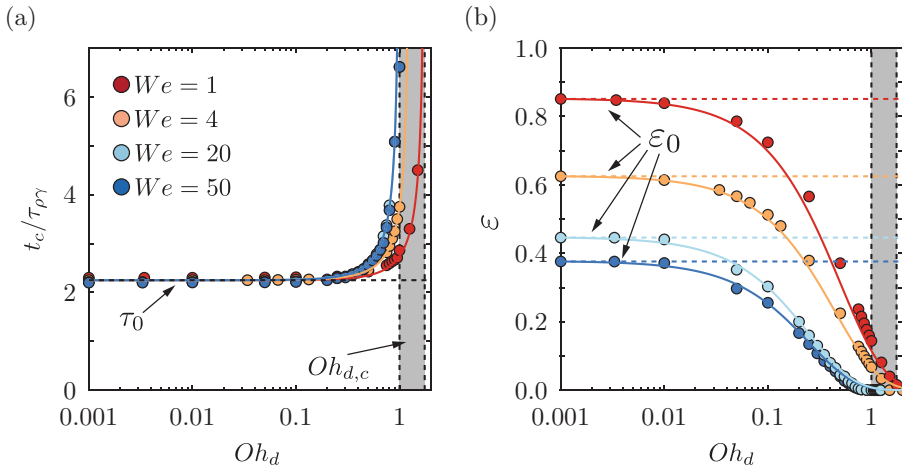


Figure 2.4.1: Light drop asymptote,  $Bo = 0$ : variation of the (a) contact time  $t_c$  normalized by the inertia-capillary timescale  $\tau_{\rho\gamma} = \sqrt{\rho_d R^3 / \gamma}$ , and (b) restitution coefficient  $\varepsilon$  with the drop Ohnesorge number  $Oh_d$  at different Weber numbers  $We$ . In both panels, the solid lines represent the theoretical predictions using a spring-mass-damper system [contact time, equation (2.20) and restitution coefficient, equation (2.21), ?]. The horizontal dotted lines represent the contact time and restitution coefficient values in the limit of inviscid drops ( $Oh_d \ll 1$ ). The limiting value of contact time  $\tau_0 = 2.25$  is independent of  $We$  while that of restitution coefficient  $\varepsilon_0$  depends on  $We$ . Lastly, the dotted black vertical lines and the gray shaded regions mark the critical Ohnesorge number  $Oh_{d,c} \sim \mathcal{O}(1)$  beyond which drops do not bounce.

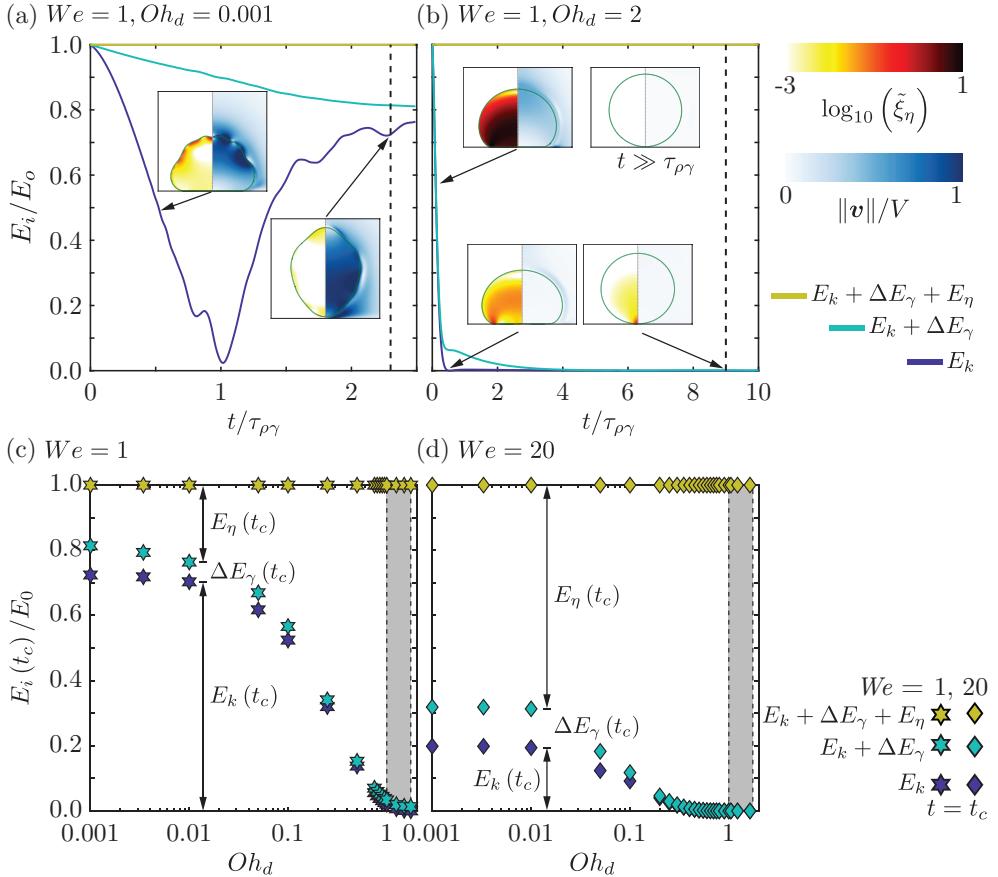


Figure 2.4.2: Details of the light drop asymptote,  $Bo = 0$ : energy budgets for typical drop impacts at  $We = 1$  for  $Oh_d = 0.001$  (a) and  $Oh_d = 2$  (b).  $E_k$  and  $E_\eta$  represent the kinetic energy and viscous dissipation, respectively.  $\Delta E_s$  denote the change in surface energy with its zero set at  $t = 0$ . The numerical snapshots in the insets illustrate the drop morphologies and the anatomy of flow inside them. Left hand side of each snapshot shows the dimensionless viscous dissipation function  $\tilde{\xi}_\eta = 2Oh(\tilde{\mathcal{D}} : \tilde{\mathcal{D}})$  on a  $\log_{10}$  scale to identify regions of maximum dissipation (black). The right hand side shows the magnitude of the velocity field normalized by the initial impact velocity,  $V$ . The black dotted lines in panels (a) and (b) mark the instant when the drop takes off and when the normal contact force between the drop and the substrate is minimum, respectively ( $t = t_c$ ). Energy distributions at  $t_c$  for  $We = 1$  (c) and  $We = 20$  (d) as a function of  $Oh_d$ . The black vertical lines and the gray shaded regions mark the critical Ohnesorge number  $Oh_{d,c} \sim \mathcal{O}(1)$  beyond which drops do not bounce. See also supplementary movie 3.

reached. On the other hand, even increasing  $Oh_d$  by over two orders of magnitude hardly affects  $t_c$  which keeps its inviscid, Weber independent value  $t_c = \tau_0 = 2.25\tau$ , expected from the inertio-capillary scaling [? ? ], until  $t_c$  diverges as  $Oh_{d,c}$  is reached. The value is also in good agreement with the fundamental mode of drop oscillation  $\pi/\sqrt{2}$  [? ]. Therefore, even as  $Oh_d$  is increased, the drop impact and bouncing behavior are still analogous to one complete drop oscillation cycle [? ].

To further investigate these behaviors, we seek to understand the different energy transfers by looking at the overall energy budgets in figure 2.4.2. The energy balance reads

$$\tilde{E}_0 = \tilde{E}_k(\tilde{t}) + \Delta\tilde{E}_\gamma(\tilde{t}) + \tilde{E}_\eta(\tilde{t}), \quad (2.16)$$

where the energies are normalized using the capillary energy scale ( $\gamma R^2$ ), and  $E_0$  is the initial kinetic energy of the drop, ( $\tilde{E}_0 = E_0/(\gamma R^2) = (2\pi/3)We$ ). At any time  $t$ ,  $E_k(t)$  and  $E_\gamma(t)$  are the kinetic and surface energy of the drop, with  $\Delta E_\gamma(t) = E_\gamma(t) - E_\gamma(t=0)$ . Finally,  $E_\eta(t)$  is the viscous dissipation until time  $t$ . Readers are referred to [? ? ? ? ] for details of energy budget calculations.

The initial kinetic energy is transferred into surface energy during the impact and spreading phases and back during the retraction and take-off stages. Throughout the process, viscous stresses dissipate energy, hampering the recovery of drop's kinetic energy. For low  $We$  and  $Oh_d$ , the drop recovers a large proportion of initial kinetic energy,  $E_k(t_c) \approx 0.75E_0$  (figure 2.4.2a and  $Oh_d \ll 1$  in figure 2.4.2c). It is noteworthy that despite having a small  $Oh_d$ , almost 20% of the initial kinetic energy still goes into viscous dissipation, which is restricted to the boundary layer at the drop-air interface and happens primarily due to the high-frequency capillary waves on the surface of the drop [see the insets of figure 2.4.2a and [? ? ]]. On the contrary, at high  $Oh_d$ , the viscous boundary layer is as large as the drop itself [? ] and consequently, dissipation happens throughout the drop (see figure 2.4.2b and its insets). Beyond the critical Ohnesorge number  $Oh_{d,c}$ , the drop impact process becomes over-damped as the drop loses all its energy by the time it reaches maximum compression, after which it slowly relaxes back to a spherical shape and stays on the substrate (figure 2.4.2b and  $Oh_d \sim \mathcal{O}(1)$  in figure 2.4.2c). We can predict this  $Oh_{d,c}$  by balancing the initial kinetic energy  $E_0 = (2\pi/3)\rho_d R^3 V^2$  with the viscous dissipation during drop impact given by,

$$E_\eta(t) = \int_0^t \int_{\Omega} \xi_\eta d\Omega dt = 2\eta_d \int_0^t \int_{\Omega} (\mathcal{D} : \mathcal{D}) d\Omega dt, \quad (2.17)$$

where  $\xi_\eta$  is the viscous dissipation function and  $d\Omega$  is the differential volume of the drop. Guided by our observation that dissipation occurs throughout the drop, we assume that  $\|\mathcal{D}\| \sim V/R$ ,  $\Omega \sim R^3$ , and we know that even as  $Oh_d$  approaches  $Oh_{d,c}$ , we can still approximate the contact time with the inertio-capillary timescale. Therefore, we get

$$E_\eta(\tau_{\rho\gamma}) \sim \eta_d \left( \frac{V}{R} \right)^2 R^3 \tau_{\rho\gamma}. \quad (2.18)$$

Balancing  $E_\eta(\tau_{\rho\gamma})$  with the initial kinetic energy  $E_0 \sim \rho_d R^3 V^2$  gives,

$$\rho_d R^3 V^2 \sim \eta_d \left( \frac{V}{R} \right)^2 R^3 \tau_{\rho\gamma}, \quad (2.19)$$

which on rearranging gives  $Oh_{d,c} \sim \mathcal{O}(1)$ , consistent with the  $Bo \rightarrow 0$  limit of equation (2.14), and agreeing well with the gray shaded regions in figure 2.4.1 and 2.4.2. Furthermore, at such high values of  $Oh_d$ , the drops become less deformable [?], diminishing the fraction of energy that goes to surface energy at take off (figures 2.4.2c,d).

To further rationalize these observations and predict the dependence of the rebound time and restitution coefficient on  $Oh_d$ , we compare our simulation results to the spring-mass-damper system that has been shown to capture these variations successfully [? ?]. In such a model, the time of apparent contact is given by

$$t_c = \tau_0 \left( \frac{1}{\sqrt{1 - (Oh_d/Oh_{d,c})^2}} \right), \quad (2.20)$$

and matches well with the simulation data (figure 2.4.1a). Here, the critical Ohnesorge number  $Oh_{d,c}$  at which bouncing stops is taken from simulations. By evaluating the drop's take-off velocity at this instant, [?] predicted the coefficient of restitution, written in our notations, as

$$\varepsilon = \varepsilon_0 \exp \left( \frac{-\beta Oh_d / Oh_{d,c}}{\sqrt{1 - (Oh_d / Oh_{d,c})^2}} \right), \quad (2.21)$$

where  $\varepsilon_0$  is the  $We$ -dependent coefficient of restitution in the inviscid drop limit (see appendix 2.B) and  $\beta = 4 \pm 0.25$  is a fitting parameter that best fits our data (notice the remarkable agreement in figure 2.4.1b). Note that [? ] further reduced equation (2.21) to  $\varepsilon \approx \varepsilon_0 \exp(-\alpha Oh_d)$  for  $Oh_d \ll Oh_{d,c}$ , where  $\alpha = \beta / Oh_{d,c} = 2.5 \pm 0.5$  best fits all their experimental datapoints, independent of the impact Weber number. The equivalent fitting parameter for our case is  $\alpha' = \beta' / Oh_{d,c} = 3 \pm 1$ , which is very close to [? ], despite a difference in  $Bo$  [0 here vs. 0.167 for [? ], also see § 2.4.2, and appendix 2.B].

Lastly, figure 2.4.1 also highlights that  $Oh_{d,c}$  varies weakly with  $We$ ,  $Oh_{d,c} = 1.75, 1.5, 1, 1$  at  $We = 1, 4, 20, 50$ , respectively, as evidenced by the narrow grey shaded region, and in agreement with the limit predicted from equation (2.14). We stress that the variation of the coefficient of restitution in the shaded region, where  $\varepsilon < 0.1$ , is weak and would not be noticed in typical side view experiments. Indeed,  $\varepsilon = 0.1$  corresponds to a center of mass rebound height of 0.01 times the initial impact height that sets  $We$ . For  $We = 1$ , this gives a rebound height of 10  $\mu\text{m}$  which is too small to be experimentally measurable.

The primary influence of  $We$  is to decrease the inviscid limit restitution  $\varepsilon_0$ . To understand this behavior, we also plot the energy distribution at take-off for  $We = 20$  in figure 2.4.2(d). We clearly observe that irrespective of the drop Ohnesorge number, the viscous dissipation is higher for  $We = 20$  as compared to that of  $We = 1$  (figure 2.4.2c). Even more strikingly, the fraction of energy lost to viscous dissipation amounts to almost 70% of the initial energy, even in the inviscid drop limit for  $We = 20$ . This increase in dissipation can be attributed to more deformable drops at higher  $We$  and flow enhancement during retraction owing to a strong radially inward flow field (see the inertial regime of chapter 1). The dissipation is not only restricted to the boundary layers at the drop-air free-surface but also at the axis of drop when the retraction phase ends (see figure 1.2 which has the same  $We$  based on the radius of the drop). Consequently,  $\varepsilon$  decreases with increasing  $We$ . We further elaborate on this variation in appendix 2.B.

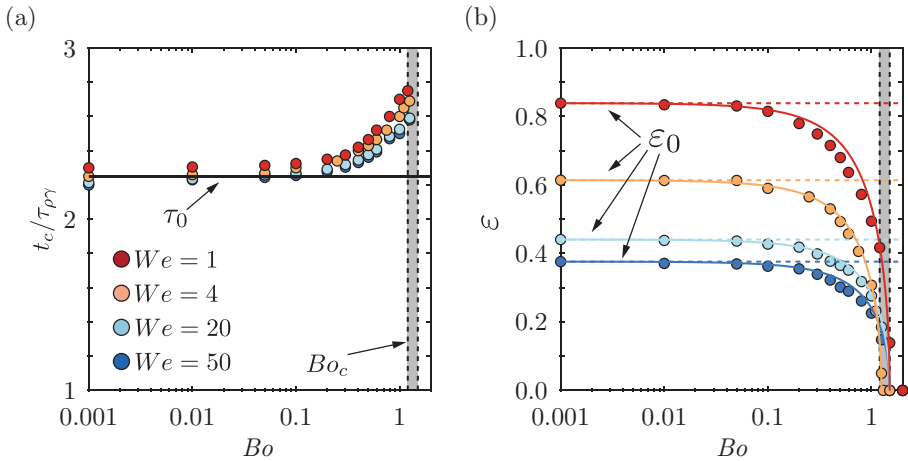


Figure 2.4.3: Inviscid drop asymptote ( $Oh_d = 0.01 \ll 1$ ): variation of the (a) contact time  $t_c$  normalized by the inertia-capillary timescale  $\tau_{\rho\gamma} = \sqrt{\rho_d R^3 / \gamma}$ , and (b) restitution coefficient  $\varepsilon$  with the Bond number  $Bo$  at different Weber numbers  $We$ . In both panels, the solid lines represent the theoretical predictions from a spring-mass analogy [equation 2.24, ? ]. The horizontal dotted line in panel (b) represents the restitution coefficient values in the limit of zero Bond number ( $Bo \rightarrow 0$ ). This limiting value of restitution coefficient  $\varepsilon_0$  depends on  $We$ . Notice that although the restitution coefficients match with the predictions from the model, the contact time show slight deviations from the prediction of a constant contact time,  $\tau_0 = 2.25$ , when  $Bo_c$  is approached. Lastly, the dotted black vertical lines and the gray shaded regions mark the critical Bond number  $Bo_c \sim \mathcal{O}(1)$  beyond which drops do not bounce.

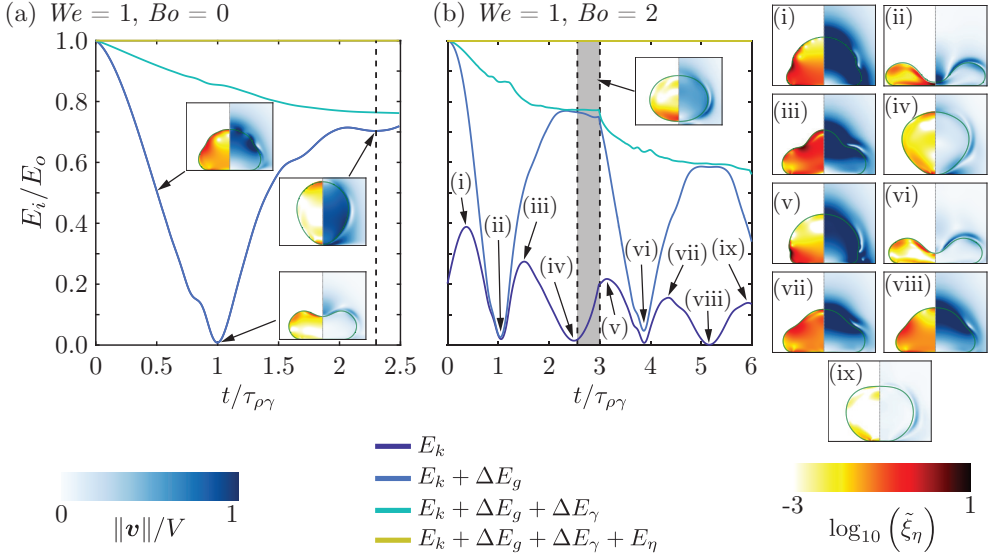


Figure 2.4.4: Details of the inviscid drop asymptote ( $Oh_d = 0.01 \ll 1$ ): energy budgets for typical drop impacts at  $We = 1$  for  $Bo = 0$  (a) and  $Bo = 2$  (b) in the limit of inviscid drops.  $E_k$  and  $E_\eta$  represent the kinetic energy and viscous dissipation, respectively.  $\Delta E_g$  and  $\Delta E_s$  denote the change in gravitational potential energy and surface energy, respectively with their zeroes set at the instant of maximum spreading of the impacting drop, and at  $t = 0$ , respectively. The numerical snapshots in the insets illustrate the drop morphologies and the anatomy of flow inside them. Left hand side of each snapshot shows the dimensionless viscous dissipation function  $\tilde{\xi}_\eta = 2Oh(\tilde{\mathcal{D}} : \tilde{\mathcal{D}})$  on a  $\log_{10}$  scale to identify regions of maximum dissipation (black). The right hand side shows the magnitude of the velocity field normalized by the initial impact velocity  $V$ . The black dotted line in panel (a) marks the instant when the drop takes off, setting  $t_c = 2.3\tau_{\rho\gamma}$ . In panel (b), the black vertical lines and the gray shaded regions bound the time interval when the normal contact force between the drop and the substrate is zero. See also supplementary movie 4.

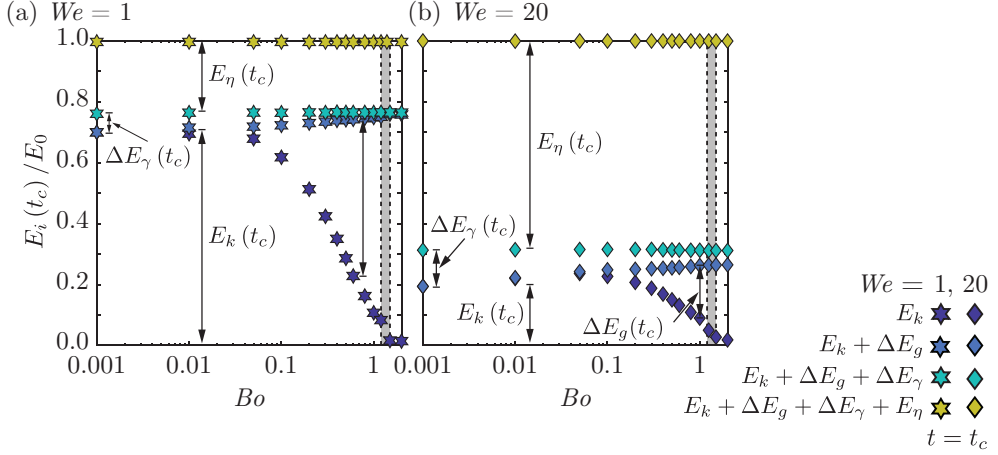


Figure 2.4.5: Details of the inviscid drop asymptote ( $Oh_d = 0.01 \ll 1$ ): energy distributions at  $t_c$  for  $We = 1$  (a) and  $We = 20$  (b) as a function of  $Bo$ . For non-bouncing cases,  $t_c$  represents the end of first drop oscillation cycle, for example  $t_c = 2.5\tau_{\rho\gamma}$  in figure 2.4.4(b). The black vertical lines and the gray shaded regions in each panel mark the critical Bond number  $Bo_c \sim \mathcal{O}(1)$  beyond which drops do not bounce.

#### 2.4.2 How does a heavy drop stop bouncing?

For drops much larger than their visco-capillary lengths (drop Ohnesorge number  $Oh_d \ll 1$ ), the criterion for bouncing inhibition (equation (2.14)) reduces to

$$Bo_c = 1. \quad (2.22)$$

In this section, we sweep across this asymptote by setting  $Oh_d = 0.01 \ll 1$  and systematically varying the Bond number,  $Bo$ . The choice of  $Oh_d$  stems from the constancy of  $\varepsilon$  and viscous dissipation as shown in figures 2.4.1 and 2.4.2 for  $Oh_d \lesssim 0.01$ , and discussed later in this section.

At this asymptote, increase in  $Bo$  hardly influences the drop contact time. This behavior is similar to the  $Oh_d$  sweep at the  $Bo = 0$  asymptote (§ 2.4.1). However, in contrast to that asymptote, even as we approach  $Bo_c$ , beyond which the drop cannot leave the substrate, the contact time is only marginally higher than  $\tau_0$  (its value at  $Bo = 0$ , figure 2.4.3a). Of course, for  $Bo > Bo_c$ , the contact time  $t_c$  is undefined. Similarly, as  $Bo = Bo_c$  is reached, the restitution coefficient decreases sharply to zero. However, in the intermediate range,  $0 < Bo < Bo_c$ , the restitution coefficient deviates only slowly from

$\varepsilon_0$ , its  $We$ -dependent value at zero Bond number (figure 2.4.3b). Finally, yet another similarity to the previous asymptote is the influence of increasing the impact Weber number,  $We$  which does not change the contact time but decreases the restitution coefficient monotonically (figure 2.4.3b). Moreover,  $We$  only weakly influences the critical Bond number  $Bo_c$  (gray shaded region in figure 2.4.3).

To further investigate these behaviors, we seek to understand the different energy transfers by looking at the overall energy budgets in figure 2.4.4. The energy balance (equation (2.16)) now has an additional contribution due to gravitational potential energy,  $\Delta E_g$ , whose zero is set at the instant of maximum drop compression. The modified energy balance reads

$$\tilde{E}_0 = \tilde{E}_k(\tilde{t}) + \Delta\tilde{E}_g + \Delta\tilde{E}_\gamma(\tilde{t}) + \tilde{E}_\eta(\tilde{t}), \quad (2.23)$$

where the initial energy also includes gravity,  $\tilde{E}_0 = (4\pi/3)(We/2 + Bo(1 - \mathcal{H}))$ , where  $\mathcal{H}$  is the center of mass height of the drop at maximum compression.

Figure 2.4.4(a) illustrates the energy budget for  $(We, Oh, Bo) = (1, 0.01, 0)$ . Comparing it with the case shown in figure 2.4.2(a) (where  $Oh = 0.001$ ), surprisingly, we encounter many similarities. They follow similar temporal dynamics, and the fraction of kinetic energy recovered at take-off and the viscous dissipation until this instant are the same, even though  $Oh$  differs by an order of magnitude. Although a higher  $Oh_d$  increases the viscous boundary layer and the dissipation is spread throughout the drop, it attenuates most of the high-frequency capillary waves, decreasing the local viscous dissipation function (*c.f.*, insets of figures 2.4.2a and 2.4.4a). Consequently, the total dissipation is the same and explains the constancy of  $\varepsilon$ .

We now look at a case where  $Bo > Bo_c$ , see figure 2.4.4(b). Just before impact, the drop has a higher initial energy owing to the contribution from gravitational potential. As a result, upon impact with the substrate, the drop accelerates until the inertial shock propagates throughout the drop [see figure 2.4.4b-i and ? ? ], after which the kinetic energy decreases as the drop then reaches maximum compression (figure 2.4.4b-ii). The maximum spreading time ( $t_m \approx \tau_{p\gamma}$ ) is same for both cases even though the drop undergoes more deformation at a higher  $Bo$ . This higher deformation coupled with an accelerated flow owing to gravity, enhances the absolute viscous dissipation but, coincidentally, the ratio of this dissipation to the initial energy is still similar to the case of  $Bo = 0$ . During the retraction stage, the kinetic energy of the drop increases (figure 2.4.4b-ii to 2.4.4b-iii) until the motion goes from being

dominantly in the radial direction to being dominantly in the axial direction [figure 2.4.4b-iii,  $t \approx 1.5\tau_{\rho\gamma}$ , see ? ? ]. Beyond this instant, gravity opposes the upward motion of the drop as its kinetic energy decreases and eventually at  $t \approx 2.5\tau_{\rho\gamma}$  (figure 2.4.4b-iv) the center of mass of the drop starts moving in the downward direction. By this time, only  $\approx 20\%$  of drop's initial energy goes to viscous dissipation, identical to the case of  $Bo = 0$ . Interestingly, the drop can still detach from the substrate owing to capillary oscillations (see the gray shaded region in figure 2.4.4b and the corresponding inset), but the center of mass velocity is always in the downward direction and we categorize this case as non-bouncing. Subsequently, the drop undergoes several capillary oscillations at the substrate with a time period of  $\approx 2.5\tau_{\rho\gamma}$  (figure 2.4.4b-v to 2.4.4b-ix) until all its energy is lost to viscous dissipation [? ].

In summary, as  $Bo$  increases, the fraction of initial energy that goes into viscous dissipation is constant. However, the gravitational potential energy increases, leading to a decrease in both the surface and kinetic energy of the drop at take-off, which eventually stops bouncing at  $Bo_c$  (figure 2.4.5a,b). To further rationalize these observations and predict the dependence of  $\varepsilon$  on  $Bo$ , guided by our simulation results, we used the simplest non-dissipative spring-mass model that incorporates gravity, developed by ? ], written in our notation as

$$\varepsilon = \varepsilon_0 \sqrt{\left(1 - \frac{Bo}{Bo_c}\right) \left(1 + \frac{1}{3} \frac{Bo}{Bo_c}\right)}. \quad (2.24)$$

This expression perfectly reproduces the variation of  $\varepsilon$  across the entire range of  $Bo$  (figure 2.4.3b). Here, we extract  $Bo_c$  from our simulation data.

## 2.5 Conclusions and outlook

Drops smaller than their visco-capillary length, i.e.,  $Oh_d > 1$  stop bouncing due to viscous dissipation, while those larger than their gravito-capillary length, i.e.,  $Bo > 1$  cannot bounce due to their weight. In this contribution, we have addressed the bouncing inhibition for drops of intermediate sizes (i.e.,  $\eta_d^2/\rho_d\gamma < R < \sqrt{\gamma/\rho_d g}$ ). Particularly, we investigated how viscous stresses and gravity conspire against capillarity to inhibit drop bouncing off non-wetting substrates. Drawing an analogy with the case of coalescence-induced jumping of two identical drops [? ? ? ], we proposed the criterion,

$Oh_{d,c} + Bo = 1$ , for this bouncing to non-bouncing transition. Through a series of direct numerical simulations, we showed the validity of this criterion over a wide range of  $We$  in the  $Bo$ - $Oh_d$  phase space. We also studied the two limiting cases and elucidated how the drops stop bouncing by exploring the drop morphology and flow anatomy. These two asymptotes show several distinguishing features.

For drops much smaller than their gravito-capillary lengths ( $Bo \ll 1$ ), as the  $Oh_d$  increases, the drop impact and bouncing behavior are still analogous to one complete drop oscillation cycle. The time of contact hardly changes from its inviscid limit even when  $Oh_d$  is increased over two orders of magnitude until a critical Ohnesorge number  $Oh_{d,c} \sim \mathcal{O}(1)$  is reached at which the contact time diverges. On the other hand, the restitution coefficient decays exponentially with increasing  $Oh_d$ , owing to increased viscous dissipation. These observations are consistent with previous studies and the spring-mass-damper theoretical model developed by [?]. Beyond the critical Ohnesorge number, the process becomes over-damped as the drop loses all its energy by the time it reaches maximum compression, after which it slowly relaxes back to a spherical shape and stays on the substrate.

For drops much larger than their visco-capillary lengths ( $Oh_d \ll 1$ ), similar to the above asymptote, an increase in  $Bo$  hardly influences the drop contact time. Even as we approach the critical Bond number  $Bo_c \sim \mathcal{O}(1)$ , beyond which the drop cannot leave the substrate, the contact time is only marginally higher than its value at  $Bo \rightarrow 0$ . Moreover, the restitution coefficient deviates slowly from  $\varepsilon_0$ , its  $We$ -dependent value at zero Bond number, until  $Bo_c$  is reached, decreasing sharply to zero. We used the simplest non-dissipative spring-mass model that incorporates gravity, developed by [?], to study this behavior which matches perfectly with our simulation results in the inviscid drop limit. Indeed, an increase in  $Bo$  does not change the fraction of the initial energy of the drop that goes into viscous dissipation during the drop impact and retraction process. Beyond  $Bo_c$ , the drop stops bouncing because the flow generated during the retraction phase is insufficient to lift the drop owing to its weight. Lastly, contrary to the viscous limit, even when the drop cannot leave the substrate, it has sufficient surface and kinetic energies to undergo several oscillation cycles at the substrate.

We further emphasize that both the bouncing inhibition and drop contact time are reasonably insensitive to an increase in impact Weber number ( $We$ ), which only manifests as a decrease in the restitution coefficient owing to higher viscous dissipation provided, of course, that  $We$  is not too small ( $We \ll 1$ ) or

not too large ( $We \gtrsim 100$ ), so that axial symmetry would be broken.

We emphasize here that this work deciphers the theoretical upper bound of the bouncing to non-bouncing transition on an ideal non-wetting substrate. Indeed, the water drops can cease bouncing due to substrate pinning on non-ideal superhydrophobic substrates [? ]. We further make idealization regarding the surrounding medium by keeping its Ohnesorge number small ( $Oh_a = 10^{-5}$ ) so that it does not influence the impact process, and the dissipation is primarily inside the drop. The surrounding medium might play a role in the impact of microdroplets if  $Oh_a$  is comparable to  $Oh_d$  [? ? ]. Lastly, we solely focus on drops impacting with velocities exceeding or equal to their inertio-capillary velocity ( $We \geq 1$ ). It will be interesting to extend this work for  $We \ll 1$  where the drops only deform weakly, and the velocity field inside them is still significant at the instant of maximum spreading. One can either use a quasi-static model of bouncing drops [?] or an analogy with non-linear springs [?] to probe that regime. Another extension would be to the case of very large  $We$  so that the axial symmetry is lost and full three-dimensional simulations must be calculated, but this regime is beyond the scope of the present work.

## Acknowledgments

We thank Aditya Jha for sharing data. We also thank Uddalok Sen, Maziyar Jalaal, Andrea Prosperetti, David Quéré, and Jacco Snoeijer for stimulating discussions. We acknowledge Srinath Lakshman for preliminary experiments that made us numerically and theoretically explore the effect of gravity in viscous drop bouncing.

# Appendix

## 2.A Measuring the restitution coefficient

Throughout this chapter, we have used the time of contact and restitution coefficient to study the drop impact dynamics. In this appendix, we describe how to consistently measure this restitution coefficient which is the ratio of take-off velocity  $v_{\text{cm}}(t_c)$  to the impact velocity  $V$ ,

$$\varepsilon = \frac{v_{\text{cm}}(t_c)}{V}, \quad (2.25)$$

where  $t_c$  denotes the contact time when the drop leaves the substrate. Note that for our simulations, we assume an ideal non-wetting substrate by ensuring that a thin air layer (with a minimum thickness of  $\Delta = R/1024$ , where  $\Delta$  is the minimum grid size employed in the simulations), is always present between the drop and the substrate [also see ? ]. Inspired by chapter 1, we define the end of contact as the instant when the normal reaction force  $F(t)$  between the substrate and the drop is zero [for calculation details, see equation (1.1) and ? ], as shown in figure 2.A.1(a). Subsequently, we read out the center of mass velocity (figure 2.A.1b) at this instant. If this center of mass velocity is not in the upward direction (i.e., it is zero or negative), we categorize the case as non-bouncing. For the representative case in figure 2.A.1,  $\varepsilon = 0.47$ .

## 2.B Influence of Weber number

This work shows that the bouncing inhibition and drop contact time are fairly insensitive to an increase in the impact Weber number (in the range  $1 \leq We \leq 50$ ) while the restitution coefficient decreases monotonically due to higher viscous dissipation. To further investigate this dependence, figure 2.B.1

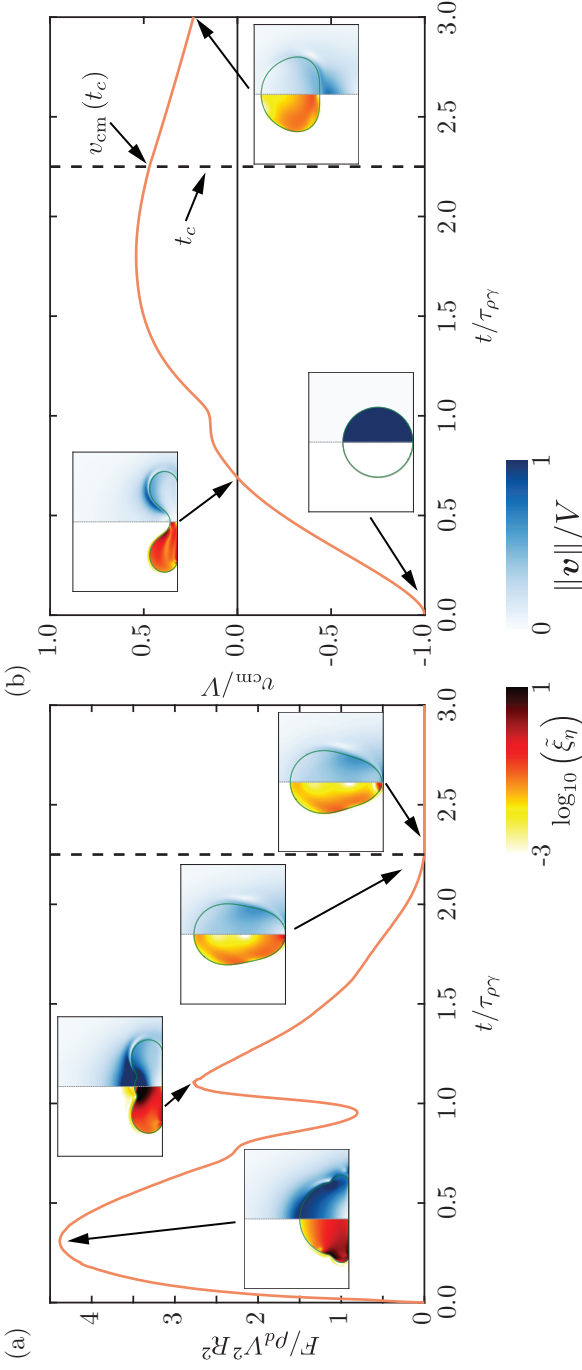


Figure 2.A.1: A representative temporal variation of (a) the normal reaction force  $F$  on the drop and (b) its center of mass velocity  $v_{cm}$ . Time is normalized using the inertia-capillary timescale  $\tau_{\rho\gamma}$ . Insets illustrate the different stages of drop impact process. The background shows the magnitude of the rate of viscous dissipation per unit volume ( $\tilde{\xi}_\eta = 2O\!h(\tilde{\mathcal{D}} : \tilde{\mathcal{D}})$ ) on the left and the magnitude of velocity field normalized by the impact velocity on the right. The vertical dashed black line represents the contact time calculated using the criterion,  $F = 0$  marking the end of contact between the drop and the substrate. Here,  $(We, Oh_d, Bo) = (4, 0.034, 0.5)$ , the contact time  $t_c = 2.25\tau_{\rho\gamma}$ , and the coefficient of restitution  $\varepsilon = 0.47$ .

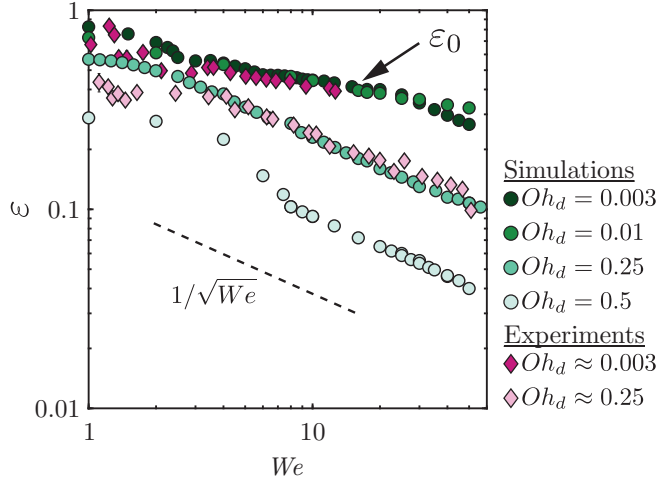


Figure 2.B.1: Variation of restitution coefficient with the impact Weber number ( $We$ ) at different drop Ohnesorge number ( $Oh_d$ ). The simulations (circle data points) match perfectly with the experimental results (diamond data points) of [? ] without any fitting parameters.  $\varepsilon_0$  is the restitution coefficient in the inviscid drop limit. The black dotted line represents  $1/\sqrt{We}$ . Here, the Bond number  $Bo = 0.167$ .

illustrates this variation of restitution coefficient with  $We$ . In the inviscid drop limit ( $Oh_d \lesssim 0.1$ ),  $\varepsilon_0$  marks the restitution coefficient which we use to scale the theoretical models used in § 2.4 [also see ? ? ]. For this range of impact Weber number  $1 \leq We \leq 50$ ,  $\varepsilon_0$  does not follow the  $1/\sqrt{We}$  scaling relation developed by [? ]. Interestingly, the restitution coefficient for viscous drop impacts ( $Oh_d \gtrsim 0.1$ ) seems to follow this scaling relation, implying that the take-off velocity scales with the Taylor-Culick velocity ( $v_{cm}(t_c) \sim \sqrt{\gamma/\rho_d R}$ ), and is independent of the impact velocity  $V$ , consistent with our assumption that the retraction and take-off stages are independent of the Weber number and disentangled from the initial impact dynamics. We caution here that the range of  $We$  is too small to claim these scaling relations convincingly. Lastly, notice the remarkable agreement between our simulations and the experimental data points from [? ] for two different drop Ohnesorge numbers, which differ by over two orders of magnitude.

## 2.C Code availability

The codes used in the present article are permanently available at [? ].

chapter 2: when does a drop stop bouncing?



source code



supplemental movies

## 2.D Supplemental movies

These supplemental movies are available at [? \].](#)

In all these videos, the left hand side of each snapshot shows the dimensionless viscous dissipation function  $\tilde{\xi}_\eta = 2Oh \left( \tilde{\mathcal{D}} : \tilde{\mathcal{D}} \right)$  on a  $\log_{10}$  scale to identify regions of maximum dissipation (black). The right hand side shows the magnitude of the velocity field normalized by the initial impact velocity,  $V$ .

- SM1: Typical bouncing (left) and non-bouncing drop cases that we study in this work. Also see figure 2.3.1.
- SM2: Three representative cases away from the two asymptotes: direct numerical simulations snapshots illustrating the drop impact dynamics. Also see figure 2.3.2.
- SM3: To study the details of the light drop asymptote,  $Bo = 0$ , here we show two typical cases to show inhibition of bouncing owing to enervation of internal momentum by viscous dissipation.
- SM4: To study the details of the inviscid drop asymptote,  $Oh_d = 0.01 \ll 1$ , here we show two typical cases to show how gravity ceases the bouncing of a drop by pulling it down. Note that even though the case with  $Bo = 2$  manages to leave the substrate, its center of mass velocity vector points downwards throughout the duration when it is levitating over the substrate.

## Chapter 3

# Drop impact on viscous liquid films<sup>o</sup>

When a liquid drop falls on a solid substrate, an air layer is trapped between them, delaying the occurrence of liquid–solid contact. For impacts on smooth substrates, such an air film can prevent wetting, allowing the drop to bounce off with dynamics identical to that observed for impacts on superamphiphobic materials. In this chapter, we investigate similar bouncing phenomena, occurring on viscous liquid films, that mimic atomically smooth substrates, with the goal to probe their repellent properties. In the case of highly viscous or very thin films, the impact dynamics are not affected by the presence of the viscous film. Within this substrate–independent limit, repellency is suppressed once the drop viscosity exceeds a critical value as on superamphiphobic substrates. For thicker or less viscous films, both the drop and film properties influence the rebound dynamics and conspire to inhibit bouncing above a critical film thickness. This substrate–dependent regime also admits a limit, for low viscosity drops, in which the film properties alone determine the limits of repellency. We elucidate the mechanisms associated to the bouncing to floating transition using experiments, simulations, and a minimal model that predicts the main characteristics of drop impact, the contact time and coefficient of restitution.

---

<sup>o</sup>Submitted as: **Vatsal Sanjay**, Srinath Lakshman, Pierre Chantelot, Jacco H. Snoeijer, and Detlef Lohse, *Drop impact on viscous liquid films*, J. Fluid Mech. Simulations are done by Sanjay; experiments by Lakshman; writing and analysis by Sanjay, Lakshman, and Chantelot; and supervision by Snoeijer and Lohse. Proofread by everyone.

### 3.1 Introduction

Liquid drop impact on solids and liquids abound in nature [? ] and are essential for several industrial applications, such as inkjet printing [? ] and criminal forensics [? ]. Consequently, drop impact has garnered extensive attention [? ? ? ? ? ] ever since the seminal work of [? ]. Impacts can result in either contact or levitation (bouncing/floating) outcomes, depending on whether the air layer trapped between the drop and the substrate drains completely during impact.

For low impact velocities, the buildup of the lubrication pressure in the draining air layer prevents the drop from contacting with the underlying surface, leading to drop bouncing/floating on this layer [? ? ? ? ? ]. Drops that bounce/float in such a scenario are realized in several configurations, for example on solid surfaces [? ? ], liquid films [? ? ? ? ], stationary [? ? ? ] or vibrating liquid pools [? ? ], or even soap films [? ]. Interfacial processes such as Marangoni flow [? ] or the generation of vapor below a drop deposited on a superheated substrate [the Leidenfrost effect where the liquid levitates on a cushion of its own vapor, ? ? ? ? ] can further stabilize the sandwiched air/vapor layer to facilitate levitation, even for the dynamic case of drop impact [? ? ? ]. Drops can also defy gravity and levitate thanks to the so-called inverse Leidenfrost effect [? ? ? ], or electromagnetic forces [? ? ].

At higher impact velocities, the air layer ruptures, leading to contact. The rupture occurs due to a strong van der Waals attractive force between the droplet and the substrate, which comes into play as the thickness of the gas layer reduces below a thickness of the order of  $10 - 100\text{ nm}$  [see appendix 3.A, and [? ? ? ]]. Additionally, surface asperities that are of the order of the minimum gas layer thickness can also cause rupture, binding the drop to the surface [? ? ? ].

In this work, we perform experiments and direct numerical simulations (DNS) to investigate drop rebound on viscous liquid films. In the limit of thin enough viscous coatings, the substrate mimics an atomically smooth solid and displays a superamphiphobic-like repellent behavior [? ? ]. This substrate-independent bouncing [? ? ? ? ] can be compared with that observed on superhydrophobic substrates whereby the apparent contact time is given by the oscillation time of a drop [? ], owing to the drop impact-oscillation analogy [? ]. However, unlike ideal Rayleigh oscillations, the collisions are partially inelastic due to viscous dissipation [? ]. The elasticity of such impacts can be

increased by reducing the viscosity of the drop [? ? ]. As a result, such an impacting drop can be modeled using quasi-ideal spring with stiffness given by the surface tension coefficient [? ]. In addition, when the drop viscosity increases and viscous dissipation becomes significant, this spring couples with a linear damper whose strength is proportional to the drop's viscosity [see appendix 3.B, and ? ]. The adoption of such a spring-mass-damper system has led to several successful predictions of the drop impact dynamics in a variety of configurations such as viscous bouncing [? ? ], spontaneous levitation [? ], fast bouncing [? ], and walking drops [? ].

In the opposing limit of thick liquid films (pools), drops can also bounce/float [? ? ]. However, unlike solids and very thin films, these pools deform on impact and can absorb a part of the impact kinetic energy in the form of (i) interfacial deformation, (ii) internal kinetic energy, and (iii) viscous dissipation [? ]. Consequently, the impact outcomes also include a substrate-dependent regime which culminates in the transition from bouncing to floating, where the drop cannot take off from the liquid surface which loses its repellent property. ? ] studied the transition from the substrate-independent to substrate-dependent bouncing for water drops and reported that the critical film thickness marking this transition depends on the film viscosity and the impact velocity of the drops.

Here, we aim to understand how the thickness and viscosity of liquid coatings influence the rebound characteristics, culminating in the loss of repellency, that is the transition from bouncing to floating. We seek to disentangle how the initial kinetic energy of an impacting drop can be absorbed through dissipation and energy transfers in the drop and the liquid film.

The chapter is organized as follows: § 3.2 describes the experimental and numerical methods followed by § 3.3, where we discuss the phenomenology of the drop impact dynamics on viscous liquid films. Guided by our experimental and numerical observations, we develop a phenomenological model in § 3.4, extending on the spring-mass-damper analogy by considering the coating as an additional source of dissipation. In § 3.5, we test the validity and applicability of this model by comparing the predicted values of the coefficient of restitution with our observations when varying both the drop and film properties. We also delineate the various regimes observed in this work by measuring the critical film thicknesses at which the substrate-independent to substrate-dependent and bouncing to floating transitions occur and compare their observed values with the model predictions. Further, § 3.6 delves into the cases where our phenomenological model fails to predict the observed dynamics. The chapter

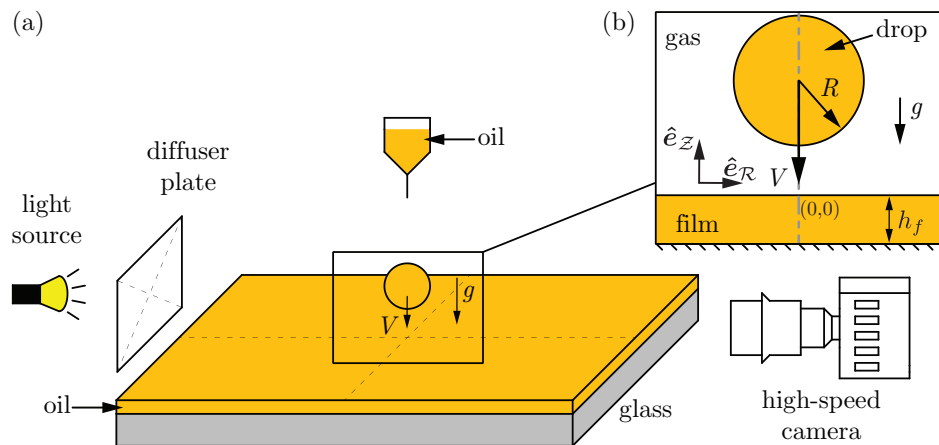


Figure 3.1.1: (a) Schematic (not to scale) of the experimental setup. (b) Side view visualization of the drop impact process as viewed using the high-speed camera. This inset also shows the axi-symmetric domain used in the direct numerical simulations.

ends with a conclusion and outlook in § 3.7.

# 3

## 3.2 Methods

### 3.2.1 Experimental details

Our experiments, outlined in figure 3.1.1, consist of silicone oil droplets, with radius  $R$ , density  $\rho_d$ , and viscosity  $\eta_d$ , impacting on silicone oil films with thickness  $h_f$ , density  $\rho_f$ , and viscosity  $\eta_f$ . We choose silicone oil as a working fluid as its viscosity can be varied over a wide range, here from 0.8 mPa.s to 96 mPa.s, while keeping its density and surface tension coefficient ( $\gamma$ ) nearly constant, as evidenced in table 3.2.1. Droplets with radius  $R = 1.0 \pm 0.1$  mm are released from a calibrated needle tip whose height can be varied to adjust the impact velocity  $V$  from 0.1 m/s to 0.5 m/s. The rupture of the air layer, mediating the interaction between the drop and the film, determines the upper bound of the bouncing regime and sets the maximal impact velocity, here Weber number (i.e., ratio of inertial to capillary stresses)  $We \equiv \rho_d RV^2/\gamma \lesssim \mathcal{O}(10)$  [see appendix 3.A and ? ? ]. We further fix the impact velocity at  $V = 0.3 \pm 0.03$  m/s, corresponding to  $We = 4$ , and focus on the influence of the material properties of the drop and the film on the impact process (see § 3.2.2). Indeed, this process is fairly independent of  $We$  in the narrow range

Silicone oil	$\rho$ (kg/m <sup>3</sup> )	$\eta$ (mPa.s)	$\gamma$ (mN/m)
SE 1	818	0.8	17
AK 5	920	4.6	19
AK 10	930	9.3	20
AK 20	950	19	21
AK 35	960	34	21
AK 50	960	48	21
AK 100	960	96	21

Table 3.2.1: Properties of liquids used in the experiments.  $\gamma$  is the liquid-air surface tension coefficient. The silicone oil manufacturers are Shin Etsu (SE) and Wacker Chemie AG (AK).

of  $We$  in which bouncing occurs without air layer rupture (see appendices 3.A and 3.C).

Films of controlled thickness, varying from 0.01 mm to 1 mm, are prepared by spincoating the liquid for  $h_f < 0.03$  mm, or by depositing a known volume of silicone oil on a glass slide and allowing it to spread when  $h_f > 0.03$  mm. We measure the thickness of spincoated films using reflectometry [? ], with an uncertainty of  $\pm 0.1$   $\mu$ m, while the thicker films obtained from the deposition method are characterized from side-view imaging, using a procedure detailed in appendix 3.D, with an uncertainty of  $\pm 30$   $\mu$ m. We record the impact dynamics using a high-speed side-view imaging at 10,000 frames per second (Photron UX100).

### 3.2.2 Governing equations & Numerical framework

This section elucidates the direct numerical simulation (DNS) framework used to study the drop impact process with the free software program, Basilisk C [? ], using the volume of fluid (VoF, equation (3.1) for tracking the interface, ? ? ). In this work, we have three fluids, namely, the drop, film, and air, denoted by  $(d)$ ,  $(f)$ , and  $(a)$ , respectively (figure 3.1.1). In order to track the three fluids and employ the non-coalescence between the drop and the film, we use two VoF tracer fields,  $\Psi_1, \Psi_2$  [? ]

$$\left( \frac{\partial}{\partial t} + \mathbf{v} \cdot \nabla \right) \{ \Psi_1, \Psi_2 \} = 0, \quad (3.1)$$

where  $\mathbf{v}$  is the velocity field. The use of two VoF fields, followed by interface

reconstruction and implicit tagging of the air medium ( $= 1 - \Psi_1 - \Psi_2$ ), ensures that the two tracers never overlap [? ? ]. As a result, there is always a thin air layer between the two liquids. Our continuum-based simulations are thus not sufficient to predict the coalescence or non-coalescence of interfaces [? ]. We take this information from experiments (see appendix 3.A for details).

The adaptive mesh refinement (AMR) allows us to resolve all the length scales pertinent to the flow. The adaption is based on minimizing the error estimated using the wavelet algorithm [? ] in the volume of fluid tracers, interfacial curvatures, velocity field, vorticity field and rate of viscous dissipation with tolerances of  $10^{-3}$ ,  $10^{-4}$ ,  $10^{-2}$ ,  $10^{-2}$ , and  $10^{-3}$  [? ]. We ensure that at least 15–20 grid cells are present across the minimum liquid film thickness ( $\Gamma = h_f/R = 0.01$ ) studied in this work to resolve the velocity gradients in the film [? ? ]. The minimum thickness of the air layer is of the order of the minimum grid size  $\Delta = R/2048$ . Further note that this thickness can be greater than this minimum owing to flow characteristics. For example, the shear stress balance across the interface with high viscosity ratios delays the drainage of air layer [? ].

For an incompressible flow, the mass conservation requires the velocity field to be divergence-free. Furthermore, the momentum conservation reads (tildes denote dimensionless quantities)

$$\left( \frac{\partial}{\partial \tilde{t}} + \tilde{\mathbf{v}} \cdot \tilde{\nabla} \right) \tilde{\mathbf{v}} = \frac{1}{\tilde{\rho}} \left( -\tilde{\nabla} p + \tilde{\nabla} \cdot (2Oh\tilde{\mathcal{D}}) \right) - Bo \hat{\mathbf{e}}_{\mathbf{z}} + \tilde{\mathbf{f}}_{\gamma}, \quad (3.2)$$

where the coordinate dimensions, velocity field  $\mathbf{v}$ , and pressure  $p$  are normalized using the drop radius  $R$ , inertio-capillary velocity scale  $V_{\rho\gamma} = \sqrt{\gamma/\rho_d R}$  and capillary pressure  $P_\gamma = \gamma/R$ , respectively. The bracketed term on the left hand side of equation (3.2) is the material derivative. On the right hand side,  $\hat{\mathbf{e}}_{\mathbf{z}}$  is a unit vector in the vertically upward direction (see figure 3.1.1b) and the deformation tensor,  $\tilde{\mathcal{D}}$  is the symmetric part of the velocity gradient tensor  $\left( \tilde{\mathcal{D}} = \left( \tilde{\nabla} \tilde{\mathbf{v}} + (\tilde{\nabla} \tilde{\mathbf{v}})^T \right) / 2 \right)$ . Further, we employ one-fluid approximation [? ? ] to solve these equations whereby the material properties (such as dimensionless density  $\tilde{\rho} = \rho/\rho_d$  and dimensionless viscosity  $Oh$ ) change depending on which fluid is present at a given spatial location (equations (3.3)–(3.4)).

$$\tilde{\rho} = \Psi_1 + \Psi_2 \frac{\rho_f}{\rho_d} + (1 - \Psi_1 - \Psi_2) \frac{\rho_a}{\rho_d} \quad (3.3)$$

$$Oh = \Psi_1 Oh_d + \Psi_2 Oh_f + (1 - \Psi_1 - \Psi_2) Oh_a \quad (3.4)$$

where, the Ohnesorge number  $Oh$  is the ratio between the inertio-capillary to the visco-capillary time scales. It is defined for all the three phases: drop Ohnesorge number ( $Oh_d = \eta_d/\sqrt{\rho_d\gamma R}$ ), film Ohnesorge number ( $Oh_f = \eta_f/\sqrt{\rho_d\gamma R}$ ), and air Ohnesorge number ( $Oh_a = \eta_a/\sqrt{\rho_d\gamma R}$ ). Furthermore,  $\rho_f/\rho_d$  and  $\rho_a/\rho_d$  are the film-drop and air-drop density ratios. For simplification, we use  $\rho_f/\rho_d = 1$  (also see table 3.2.1). In order to keep the surrounding medium as air,  $\rho_a/\rho_d$  and  $Oh_a$  are fixed at  $10^{-3}$  and  $10^{-5}$ , respectively. The Bond number,  $Bo = \rho_d g R^2/\gamma = 0.5$  is the ratio of the gravitational to the capillary pressure which is also kept fixed during this study. The initial condition (figure 3.1.1b), is given by the normalized impact velocity,  $\tilde{V} = \sqrt{We}$ .

Lastly, a singular body force  $\tilde{\mathbf{f}}_\gamma$  is applied at the interfaces to respect the dynamic boundary condition across them. The approximate forms of these forces follow from [? ?] as

$$\tilde{\mathbf{f}}_\gamma \approx \tilde{\kappa}_1 \tilde{\nabla} \Psi_1 + \tilde{\kappa}_2 \tilde{\nabla} \Psi_2. \quad (3.5)$$

Here,  $\kappa_1$  and  $\kappa_2$  are the curvatures associated with  $\Psi_1$  and  $\Psi_2$ , respectively, calculated using the height-function method. During the simulations, the maximum time-step needs to be less than the oscillation period of the smallest wave-length capillary wave because the surface-tension scheme is explicit in time [? ?].

### 3.2.3 Domain description

Figure 3.1.1(b) represents the axi-symmetric computational domain. A tangential stress-free and non-penetrable boundary condition is applied on each of the domain boundaries. The pressure gradient is also set to zero at these boundaries. In the cases where a Worthington jet formed post-impact breaks into small droplets, boundary outflow is applied at the top boundary so that these drops do not interfere with the drop rebound process. Furthermore, the domain boundaries are far enough so that they do not influence the process. The cases with low  $Oh_f$  need extra care with the train of capillary waves formed post-impact as these waves can reflect back from the walls.

## 3.3 Phenomenology

In figure 3.3.1, we compare the behaviour of a typical silicone oil drop ( $R = 1.0\text{ mm}$ ,  $V = 0.35\text{ m/s}$  and  $\eta_d = 4.6\text{ mPa.s}$ ) impacting on films with a fixed viscosity  $\eta_f = 96\text{ mPa.s}$  but with contrasting thicknesses  $h_f = 0.01, 0.35$ , and

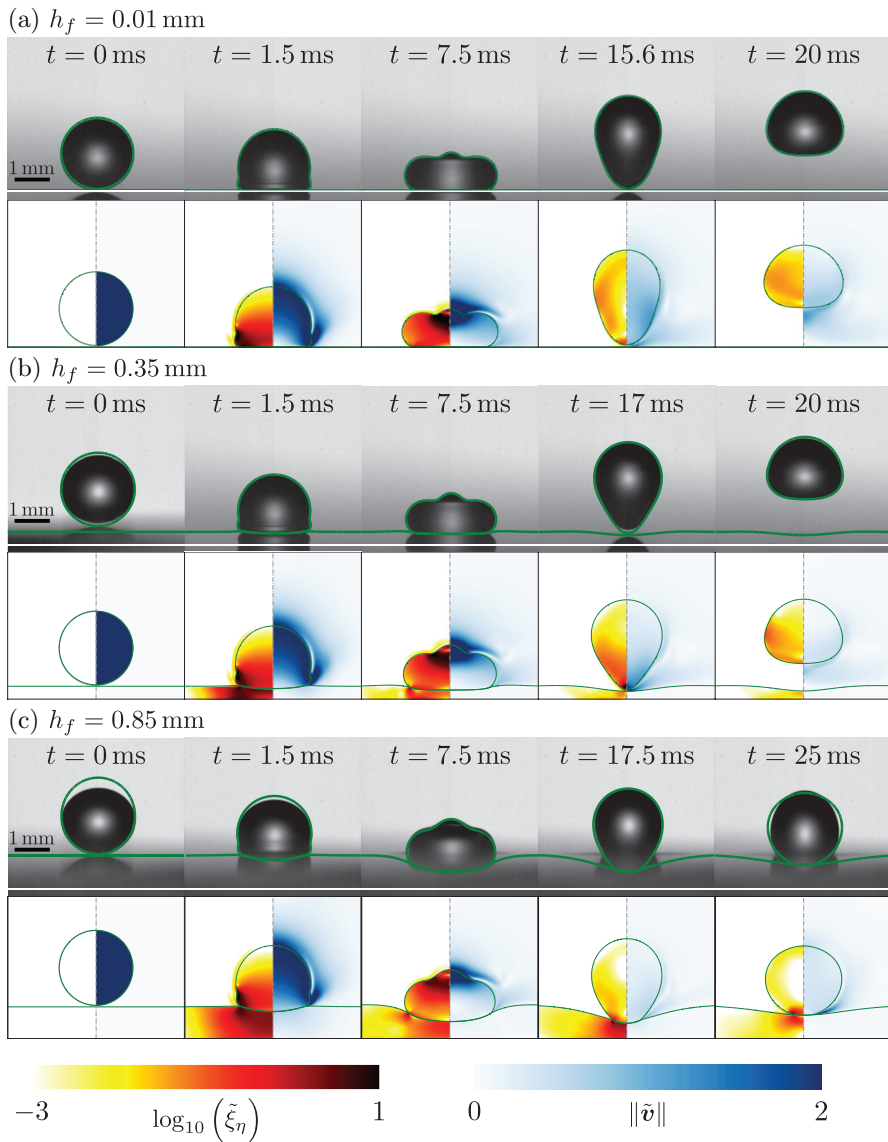


Figure 3.3.1: Effect of film thickness on the drop impact process: comparison of the experimental and DNS snapshots of the impact process on films with  $h_f$  = (a) 0.01 mm, (b) 0.35 mm, and (c) 0.85 mm. In each panel, the top row contains the experimental images with (green) interface outline from DNS, and the bottom row contains numerical snapshots showing the dimensionless rate of viscous dissipation per unit volume ( $\tilde{\xi}_\eta = 2Oh(\tilde{\mathcal{D}} : \tilde{\mathcal{D}})$ ) on the left and the magnitude of dimensionless velocity field ( $\tilde{v}$ ) on the right. We show  $\tilde{\xi}_\eta$  on a  $\log_{10}$  scale to identify regions of maximum dissipation (marked with black for  $\tilde{\xi}_\eta \geq 10$ ). For all the cases in this figure,  $R = 1$  mm,  $V = 0.3$  m/s,  $\eta_d = 4.6$  mPa.s and  $\eta_f = 96$  mPa.s, giving  $(We, Oh_d, Oh_f) = (4, 0.034, 0.67)$ . Also see supplementary videos SM1–SM3.

0.85 mm. We show a one-to-one comparison between experimental and DNS snapshots and display three pieces of information: the position of the liquid-air interfaces (green lines) that can be directly compared with experiments, the rate of viscous dissipation per unit volume (left panel of each snapshot), and the magnitude of the velocity field (right panel of each snapshot).

For the thinnest film ( $h_f = 0.01$  mm, figure 3.3.1a) and supplementary video SM1), the drop deforms as it comes in apparent contact with the film mediated by the air layer, an instant that we choose as the origin of time  $t = 0$ . The drop spreads until it reaches its maximal lateral extent, recoils and rebounds in an elongated shape after a time  $t_c = 15.6 \pm 0.1$  ms, called the contact time. Throughout the impact process, viscous stresses inside the drop dissipates energy (see  $t = 1.5$  and 7.5 ms). Consequently, after take off, the drop reaches a maximal center of mass height of  $H = 2.0 \pm 0.1$  mm relative to the undisturbed film surface, from which we deduce the restitution coefficient defined as  $\varepsilon = \sqrt{2g(H - R)}/V$ , here  $\varepsilon = 0.48$ . In the simulations, we measure the same value of the restitution coefficient using the method described in appendix 3.E. This behavior is in quantitative agreement with that reported for the impact of a viscous drop on a superhydrophobic surface by [?], suggesting that the presence of both the air and liquid film have a negligible influence on the macroscopic dynamics of the rebound, and that viscous dissipation in the drop determines the rebound height.

For  $h_f = 0.35$  mm (figure 3.3.1b) and supplementary video SM2), despite the noticeable deformation of the liquid film, the qualitative features of the bounce are similar. We further observe that as the drop takes off, the film free surface has not yet recovered its undisturbed position. We measure an increase of the contact time to  $t_c = 17 \pm 0.1$  ms and a decrease in the rebound elasticity, with  $H = 1.6 \pm 0.1$  mm leading to  $\varepsilon = 0.37$ . The DNS snapshots show that in this case, viscous dissipation occurs both in the drop and the underlying liquid. Qualitatively, the instantaneous rate of viscous dissipation in the drop is similar for  $h_f = 0.01$  mm and  $h_f = 0.30$  mm, suggesting that the decrease in rebound elasticity is primarily linked to the increased film dissipation.

Finally, for  $h_f = 0.85$  mm (figure 3.3.1c and supplementary video SM3), the film deformation increases and the substrate loses its repellent ability. The drop center of mass does not take off above  $H = R$ , the drop floats on top of the liquid film, a situation that corresponds to the inhibition of bouncing for which  $\varepsilon \approx 0$  and the contact time diverges. In this case, we notice that the experimental and numerical interface profiles differ at  $t = 0$  ms. This initial discrepancy, caused by drop oscillations upon detachment from the needle,

does not affect the subsequent impact dynamics and the impact outcome, as evidenced by the good agreement of the interface profiles at later instants.

We now systematically vary the film thickness  $h_f$  keeping the drop and film viscosity constant ( $\eta_d = 4.6 \text{ mPa.s}$  and  $\eta_f = 96 \text{ mPa.s}$ ) and plot, in figure 3.3.2(a) and (b), the contact time  $t_c$  and the coefficient of restitution  $\varepsilon$  extracted from experiments (circles) and DNS (hexagrams). Experiments and simulations are in excellent agreement when varying the film thickness by two orders of magnitude,  $h_f = 0.01 \text{ mm} - 1 \text{ mm}$ . The existence of two regimes is readily apparent. Firstly, for  $h_f \lesssim 0.1 \text{ mm}$ , both  $t_c$  and  $\varepsilon$  are independent of  $h_f$ . The value of the contact time in this regime,  $t_c = 15.6 \pm 0.5 \text{ ms}$ , corresponds to that expected from the inertio-capillary scaling [? ? ]. The contact time is proportional to  $\tau_{\rho\gamma} = \sqrt{\rho_d R^3 / \gamma}$  with a prefactor  $2.2 \pm 0.1$ , in good agreement with that calculated by [?] for the fundamental mode of drop oscillation  $\pi / \sqrt{2}$ . Similarly, the plateau value of the coefficient of restitution  $\varepsilon = 0.47 \pm 0.04$  is in reasonable agreement with that reported for the impact of water drops on superhydrophobic substrates for similar drop Ohnesorge number  $Oh_d$  and impact Weber number  $We$  [? ]. We therefore refer to this regime as substrate-independent rebound (see also appendix 3.B).

### 3

Secondly, for  $h_f \gtrsim 0.1 \text{ mm}$ , the contact time and coefficient of restitution are influenced by the film thickness. We observe that  $t_c$  increases (figure 3.3.2a) and  $\varepsilon$  decreases (figure 3.3.2b,c) with increasing  $h_f$  until  $t_c$  diverges and bouncing ceases ( $\varepsilon = 0$ ) for  $h_f \approx 0.75 \text{ mm}$ . This critical thickness marks the threshold of the rebound behavior and the transition to the floating regime. Here, the rebound characteristics vary significantly with  $h_f$  and we therefore refer to this regime as substrate-dependent.

Finally, we characterize the transition from the substrate-independent to the substrate-dependent regime by introducing the thickness  $h_{f,1}$ , in dimensionless form  $\Gamma_1 = h_{f,1}/R$ , which marks the decrease of  $\varepsilon$  to 0.9 times its plateau value  $\varepsilon^*$ . Similarly, we define the critical thickness  $h_{f,2}$ , respectively  $\Gamma_2 = h_{f,2}/R$ , associated to the transition from the substrate-dependent to the floating regime as the smallest film thickness which results in  $\varepsilon = 0$ . The impact dynamics can be categorized into three distinct regimes: a substrate-independent regime for  $\Gamma = h_f/R \leq \Gamma_1$ , a substrate-dependent regime for  $\Gamma_1 < \Gamma < \Gamma_2$ , and a floating regime for  $\Gamma \geq \Gamma_2$ .

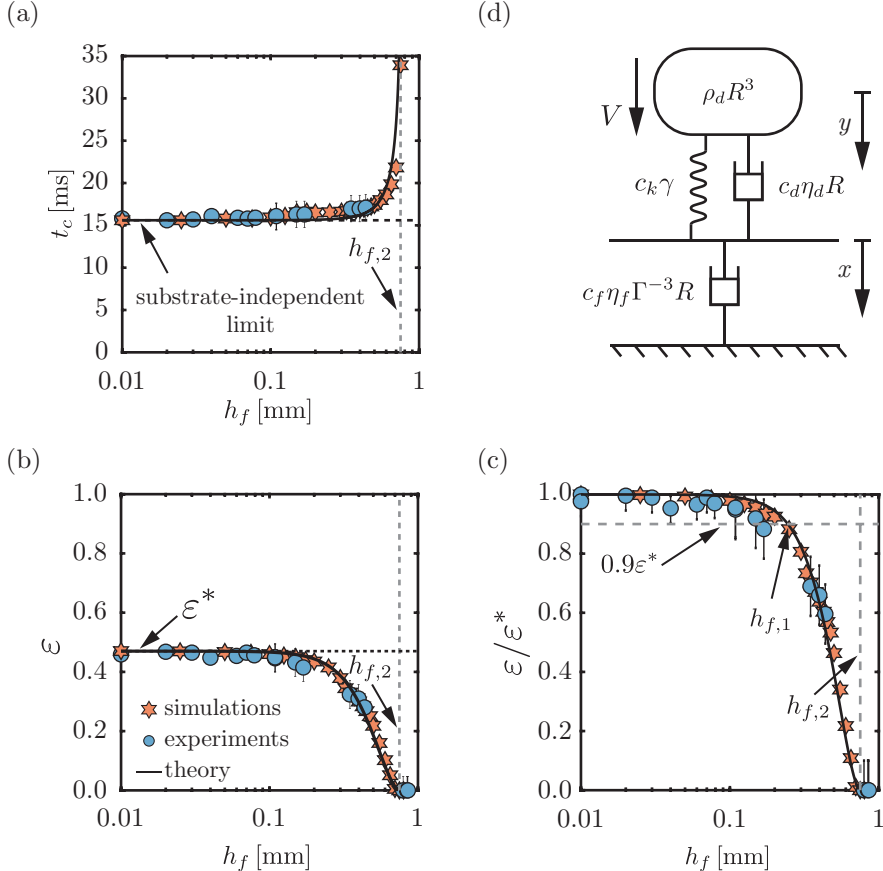


Figure 3.3.2: Effect of the film thickness on the rebound characteristics for  $R = 1$  mm,  $V = 0.3$  m/s,  $\eta_d = 4.6$  mPa.s and  $\eta_f = 96$  mPa.s, i.e.,  $(We, Oh_d, Oh_f) = (4, 0.034, 0.67)$ : (a) contact time  $t_c$ , (b) restitution coefficient  $\varepsilon$ , and (c) restitution coefficient normalized by its substrate independent value as a function of film thickness  $h_f$ . Circles and hexagrams represent experiments and DNS, respectively. In panels (a) and (b), the horizontal black dashed lines represent the substrate-independent limits of contact time and restitution coefficient, respectively, while the solid black line is from the phenomenological model with  $c_k, c_d = 2, 5.6$  (see § 3.4 and appendix 3.B). The least square fit performed on the data with equations (3.17)-(3.18) gives  $c_f = 0.46 \pm 0.1$ . Different critical thicknesses are also marked,  $h_{f,1}$  marks the substrate-independent to substrate-dependent transition ( $\varepsilon/\varepsilon^*(h_f = h_{f,1}) = 0.9$ ) and  $h_{f,2}$  marks the transition from bouncing to floating regimes. (d) Schematic diagram of the phenomenological model that describes the droplet impact process on a liquid film. The parameters:  $\rho R^3$ ,  $\eta_d R$ , and  $\gamma$  are associated to the drop properties and  $\eta_f \Gamma^{-3} R$  is associated with the film properties. The drop and the film displacements are denoted by  $y$  and  $x$ , respectively.

### 3.4 Phenomenological model

We now seek to rationalize the dependence of the rebound time and elasticity with the substrate and drop properties by constructing a minimal model, guided by our experimental and numerical observations. We build on the classical description of a drop as a liquid spring which reflects the balance of inertia and capillarity during a rebound [? ? ]. Here, we consider viscous drops and further add a damping term to the liquid spring, an approach which has been shown to successfully capture the variation of contact time and coefficient of restitution with over two orders of magnitude variation in liquid viscosities [? ]. Similarly, we interpret the film behavior through the liquid spring analogy. The film motion contrasts with that of the drop, while the latter displays a full cycle of oscillation during a rebound, the former never returns to its undisturbed position (see figure 3.3.1). This observation leads us to consider that the damping component dominates the behavior of the liquid film, and neglect the contributions of inertia and surface tension. We further discuss this assumption and its validity in § 3.6.

In figure 3.3.2(d), we present a sketch of the model, where we assume that the droplet and the film are connected in series during apparent contact, and show the scaling forms of the drop and film components. The scaling relations for the drop mass, stiffness and damping are taken from the work of ? ] as proportional to  $\rho R^3$ ,  $\gamma$ , and  $\eta_d R$ , respectively, with corresponding prefactors of 1,  $c_k$ , and  $c_d$ . We determine the values of  $c_k$  and  $c_d$  from results in the substrate-independent bouncing regime (see appendix 3.B). The scaling form of the film damping term is chosen as proportional to  $\eta_f \Gamma^{-3} R$ , where  $\Gamma = h_f/R$ , with corresponding prefactor of  $c_f$  (figure 3.3.2d). This is built on two key assumptions. First, we assume that the lubrication approximation holds in the film as, for sufficiently high film Ohnesorge numbers ( $Oh_f \gtrsim 0.1$ ), the slopes associated to the film deformations are small ( $\Gamma \ll 1$ ,  $Oh_f \sim \mathcal{O}(1)$ , see § 3.6 for limitations). And second, we choose to consider the drop as an impacting disk rather than a sphere [? ] owing to the rapid drop spreading upon impact [? ? ], which results in a damping term proportional to  $\Gamma^{-3}$  instead of  $\Gamma^{-1}$  [? ]. Lastly, we fit the prefactor  $c_f$  to our experiments and simulations, and discuss it throughout the chapter.

The equations of motion for the model system read

$$\rho R^3 \ddot{y} = -c_k \gamma (y - x) - c_d \eta_d R (\dot{y} - \dot{x}), \quad (3.6)$$

$$0 = +c_k \gamma (y - x) + c_d \eta_d R (\dot{y} - \dot{x}) - c_f \eta_f \Gamma^{-3} R \dot{x}, \quad (3.7)$$

where  $y$  and  $x$  are the displacements of the drop and the film relative to their initial position in the reference frame of the laboratory, and the dots denote time derivatives. We point out that by setting  $\dot{x} = x = 0$ , we recover the model proposed by [?], which extends the analogy between the drop impact process and a spring-mass system [? ?] by adding a damper to account for viscous dissipation in the drop. Here, we additionally consider viscous dissipation in the liquid coating and model the film as a damper without inertia.

Similarly as for the governing equations in DNS, we make equations (3.6) and (3.7) dimensionless using the length scale  $R$  and the time scale  $\tau_{\rho\gamma}$  and use tildes to identify dimensionless variables. Next, we obtain an equation of motion for the drop deformation  $\tilde{z} = \tilde{y} - \tilde{x}$ , namely

$$\left(1 + \frac{c_d Oh_d}{c_f Oh_f \Gamma^{-3}}\right) \ddot{\tilde{z}} + c_d Oh_d \left(1 + \frac{c_k}{c_d Oh_d \cdot c_f Oh_f \Gamma^{-3}}\right) \dot{\tilde{z}} + c_k \tilde{z} = 0, \quad (3.8)$$

which admits oscillatory solutions, that is drop rebound, under the condition

$$\omega^2 = 4c_k - \left(c_d Oh_d - \frac{c_k}{c_f Oh_f \Gamma^{-3}}\right)^2 > 0, \quad (3.9)$$

We note that  $\omega^2$  decreases with increasing  $\Gamma$  for fixed  $Oh_d$  and  $Oh_f$ , in qualitative agreement with the existence of a critical film height above which bouncing stops (figure 3.3.2b). Equation (3.9) allows us to determine the bounds of the bouncing regime in terms of a critical drop Ohnesorge number  $Oh_{d,c}$  and film thickness  $\Gamma_2$ . Discarding the two roots of the equation  $\omega^2 = 0$  that yield unphysical negative values of  $Oh_{d,c}$  and  $\Gamma_2$ , we obtain

$$Oh_{d,c} = \frac{1}{c_d} \left( 2\sqrt{c_k} + \frac{c_k}{c_f} \left( \Gamma_2 / Oh_f^{1/3} \right)^3 \right), \text{ and} \quad (3.10)$$

$$\Gamma_2 / Oh_f^{1/3} = \left( \frac{c_f}{c_k} (c_d Oh_d + 2\sqrt{c_k}) \right)^{1/3}. \quad (3.11)$$

Equations (3.9)–(3.11) evidence that the role of the film viscosity and height are intertwined as we find the combination  $\Gamma / Oh_f^{1/3}$ . Furthermore, the substrate-independent bouncing threshold is recovered when the film mobility,  $\Gamma / Oh_f^{1/3}$ , tends to 0, that is for very thin and/or very viscous films. Indeed, equations (3.10)–(3.11) become

$$Oh_{d,c} = \frac{2\sqrt{c_k}}{c_d}, \text{ and} \quad (3.12)$$

$$\Gamma_2/Oh_f^{1/3} = \left(2 \frac{c_f}{\sqrt{c_k}}\right)^{1/3}, \quad (3.13)$$

for the limiting cases of substrate-independent ( $\Gamma/Oh_f^{1/3} \rightarrow 0$ ), and inviscid drop ( $Oh_d \rightarrow 0$ ) asymptotes, respectively.

To go further, we solve equation (3.8) with the initial conditions  $\tilde{z} = 0$  and  $\dot{\tilde{z}} = \sqrt{We}$  at  $\tilde{t} = 0$ , yielding

$$\tilde{z}(\tilde{t}) = \frac{2\sqrt{We}}{\Omega} \exp\left(-\frac{\phi\tilde{t}}{2}\right) \sin\left(\frac{\Omega\tilde{t}}{2}\right), \quad (3.14)$$

$$\text{where } \phi = \frac{c_k + c_d Oh_d c_f Oh_f \Gamma^{-3}}{c_d Oh_d + c_f Oh_f \Gamma^{-3}} \quad (3.15)$$

$$\text{and } \Omega = \omega \left(1 + \frac{c_d Oh_d}{c_f Oh_f \Gamma^{-3}}\right)^{-1} \quad (3.16)$$

can be interpreted as an effective damper and angular frequency, respectively, by comparing the above expression to the one obtained by [? ] for  $\Gamma/Oh_f^{1/3} \rightarrow 0$ . We can deduce the expressions for both the contact time and the coefficient of restitution using these pieces of information. The contact time is taken as the instant at which the drop deformation  $\tilde{z}$  comes back to zero, which occurs at  $\Omega\tilde{t} = 2\pi$ , giving

$$\frac{t_c}{\tau_{\rho\gamma}} = \frac{2\pi}{\omega} \left( \frac{c_d Oh_d}{c_f Oh_f \Gamma^{-3}} + 1 \right). \quad (3.17)$$

Equation (3.17) is then used to compute the coefficient of restitution  $\varepsilon$  as the ratio of rebound velocity,  $\dot{\tilde{z}}(\tilde{t}_c)$ , to the impact velocity,  $\sqrt{We}$ . We immediately notice that this definition yields an expression for  $\varepsilon$  that does not depend on  $We$ , in contrast with the experimentally observed decrease of  $\varepsilon$  with  $We$ . Similarly as in [? ], we resolve this discrepancy by scaling the coefficient of restitution by  $\varepsilon_0$ , its  $We$ -dependent value in the substrate-independent limit for inviscid drops

$$\varepsilon = \varepsilon_0 \exp\left(-\frac{\pi}{\omega} \left(c_d Oh_d + \frac{c_k}{c_f Oh_f \Gamma^{-3}}\right)\right), \quad (3.18)$$

where the prefactor  $\varepsilon_0$  is obtained by fitting the substrate-independent experiments. We also recover the expressions for  $t_c$  and  $\varepsilon$  for viscous drop impact on non-wetting substrates [?], allowing us to determine  $c_k$  and  $c_d$  (see appendix 3.B).

We test the model predictions for the contact time and rebound elasticity in the substrate-dependent regime by comparing the data (symbols) presented in figures 3.3.2(a,b,c) to least-square fits of equations (3.17) and (3.18) with  $c_f$  as a free parameter (solid lines) and taking  $\varepsilon_0 = 0.58$  (see appendix 3.B). We find that the model accurately predicts the variation of  $t_c$  and  $\varepsilon$  with  $\Gamma$  for  $c_f = 0.46 \pm 0.1$ .

We now assess the predictive ability and the limits of this minimal model by experimentally and numerically varying the drop and film Ohnesorge numbers. We give particular attention to the value of the coefficient  $c_f$  necessary to fit the model to this data, and to the two asymptotes predicted by the model that bound the region of bouncing drops (equations (3.12)-(3.13)).

## 3.5 Influence of drop and film parameters

### 3.5.1 Influence of the film Ohnesorge number

We first vary the film Ohnesorge number  $Oh_f$  while keeping the drop and impact properties constant. In figure 3.5.1(a), we show the evolution of the coefficient of restitution  $\varepsilon$  for drops with  $Oh_d = 0.034$  as a function of the dimensionless film thickness  $\Gamma$  while exploring two decades in film viscosity,  $Oh_f = 0.01 - 2.0$ . On the one hand, as expected, the coefficient of restitution value is not affected in the substrate-independent limit. On the other hand, the substrate-dependent behavior shows the influence of  $Oh_f$  and we identify two regimes. For  $Oh_f \lesssim 0.1$ , the evolution of  $\varepsilon$  with  $\Gamma$  does not depend on  $Oh_f$ , as illustrated by the data collapse in figure 3.5.1(a). However, for  $Oh_f \gtrsim 0.1$ , increasing the film viscosity leads to a larger extent of the substrate-independent plateau and to an increase of the critical film thickness at which bouncing stops. This change in the  $Oh_f$  dependence can be tracked by monitoring the two dimensionless critical film thicknesses  $\Gamma_1 = h_{f,1}/R$ , and  $\Gamma_2 = h_{f,2}/R$ , which increase from 0.17 to 0.33 and 0.58 to 1.1, respectively, when  $Oh_f$  is increased from 0.1 to 2.0. We interpret the two behaviors observed in the substrate-dependent regime in the light of our minimal model, which predicts that the effective film mobility,  $\Gamma/Oh_f^{1/3}$ , controls dissipation in the substrate. In figure 3.5.1(b), we plot the coefficient of restitution data

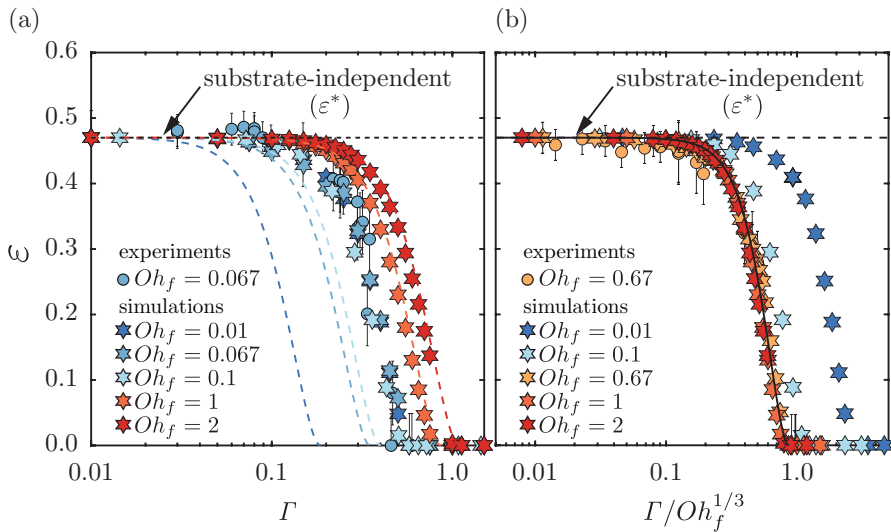


Figure 3.5.1: Influence of the film parameters on the impact characteristics: variation of the coefficient of restitution  $\varepsilon$  as a function of (a) the film thickness  $\Gamma$  and (b) the effective film mobility  $\Gamma/Oh_f^{1/3}$ . In panels (a) and (b), the circles and hexagrams correspond to the results from experiments and simulations, respectively. The colored dashed lines in panel (a) and the solid black line in panel (b) illustrate the results from the phenomenological model (equation (3.18)) with parameters  $c_k = 2$ ,  $c_d = 5.6$  and  $c_f = 0.46$ . Black dashed lines in panels (a) and (b) mark the substrate-independent limit of restitution coefficient  $\varepsilon^*$ . For all cases in this figure,  $Oh_d = 0.034$  and  $We = 4$ .

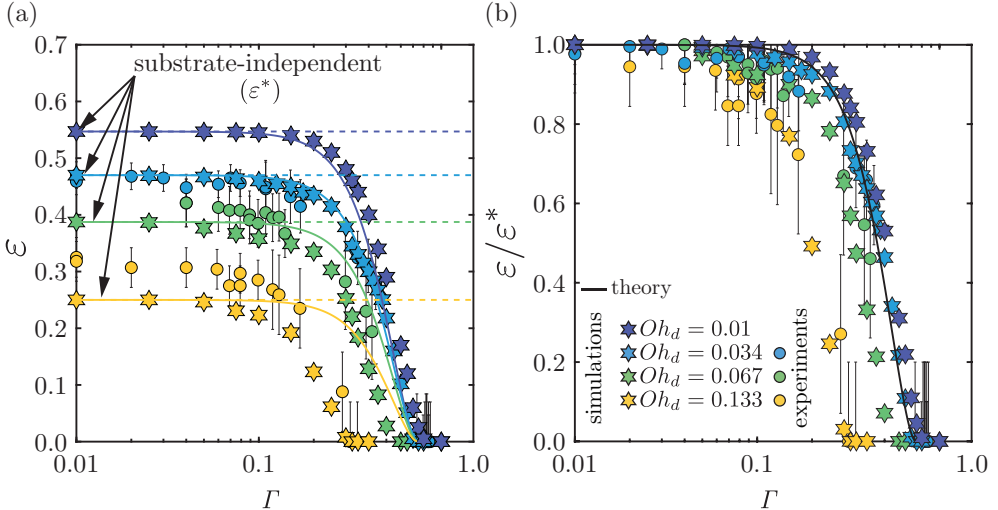


Figure 3.5.2: Influence of the drop parameters on the rebound elasticity: variation of (a) the coefficient of restitution  $\varepsilon$  and (b) the coefficient of restitution normalized with its substrate-independent value  $\varepsilon/\varepsilon^*$  as a function of film thickness  $\Gamma$ . The circles and hexagrams correspond to the results from the experiments and simulations, respectively. In panel (a), the dashed lines denote the plateau values of the restitution coefficient  $\varepsilon^*$  which depend on  $Oh_d$ . In panels (a) and (b), the solid lines represent the results from the phenomenological model (equation (3.18)) with parameters  $c_k = 2$ ,  $c_d = 5.6$  and  $c_f = 0.46$ . For all cases in this figure,  $Oh_f = 0.667$  and  $We = 4$ .

presented in (a) after rescaling the horizontal axis by  $Oh_f^{-1/3}$ . The data now collapse for  $Oh_f \gtrsim 0.1$ , indicating that the proposed approximations capture the large viscosity limit but breaks down for lower film Ohnesorge numbers. We further evidence the validity and failure of the minimal model by plotting the prediction of equation (3.18) with  $c_f = 0.46$  (solid black line).

### 3.5.2 Influence of the drop Ohnesorge number

In this section, we focus on the influence of the drop Ohnesorge number on the rebound elasticity. In figure 3.5.2(a), we plot the coefficient of restitution as a function of the dimensionless film thickness for a fixed  $Oh_f = 0.667$  and for varying  $Oh_d$  spanning the range 0.01–0.133. Increasing  $Oh_d$  affects  $\varepsilon$  across all film thicknesses. In the substrate-independent region, the coefficient of restitution decreases with increasing drop Ohnesorge number. In appendix 3.B, we show that the plateau values reported in figure 3.5.2(a) decay exponentially

with increasing  $Oh_d$  as predicted by [?]. To better illustrate the influence of  $Oh_d$  in substrate-dependent regime, we normalize the coefficient of restitution  $\varepsilon$  by its substrate-independent value  $\varepsilon^*$  (figure 3.5.2b). The data collapse only for small  $\Gamma$  indicating that the drop and film characteristics both conspire to determine the substrate-dependent behavior. We monitor the  $Oh_d$  dependence through the evolution of  $\Gamma_1$  and  $\Gamma_2$ , that both decrease with increasing Ohnesorge number.

### 3.5.3 Influence of $Oh_f$ and $Oh_d$ on the critical film thicknesses

We now characterize the influence of the drop and film Ohnesorge number by quantitatively reporting their effect on the critical thicknesses for substrate-independent to substrate-dependent ( $\Gamma_1$ ) and bouncing to floating ( $\Gamma_2$ ) transitions. Indeed, we have shown above that these two critical thicknesses are good proxies to characterize the continuous transition from substrate-independent bouncing to rebound inhibition. In figures 3.5.3(a,b), we show  $\Gamma_1$  and  $\Gamma_2$  as a function of the film Ohnesorge number for  $Oh_d$  in the range 0.01 – 0.133. This representation reflects the existence of the two distinct regimes reported in figure 3.5.1.

First, when  $Oh_f \lesssim 0.1$ ,  $\Gamma_1$  and  $\Gamma_2$  are independent of  $Oh_f$  and we write  $\Gamma_1 = \alpha_1(Oh_d)$  and  $\Gamma_2 = \alpha_2(Oh_d)$ . This observation is in contradiction with the expectations from our minimal model which predicts that  $Oh_f$  influences the values of  $\Gamma_1$  and  $\Gamma_2$ . Surprisingly, this  $Oh_f$ -independence of the critical thicknesses and the collapse observed in figure 3.5.1(a) suggest that the energy transfer to the film (in the form of kinetic and surface energies) and the film viscous dissipation are independent of film viscosity for  $Oh_f \lesssim 0.1$ . We will further elaborate on this regime in § 3.6.

Second, for larger film Ohnesorge numbers, the dissipation in the film is captured by the lubrication approximation ansatz. As a result, both critical thicknesses follow the relations  $\Gamma_1 = \beta_1(Oh_d)Oh_f^{1/3}$  and  $\Gamma_2 = \beta_2(Oh_d)Oh_f^{1/3}$ , as predicted by the model. Beyond this scaling relation, the accuracy of the minimal model is tied to its ability to predict the prefactors  $\beta_1$  and  $\beta_2$  when  $Oh_f \gtrsim 0.1$ . In figures 3.5.3(c,d), we plot  $\beta_1$  and  $\beta_2$  as a function of the drop Ohnesorge number. Both prefactors show a plateau for  $Oh_d \lesssim 0.03$  before decreasing monotonically with the drop Ohnesorge number. We compare the measured prefactors to the model predictions which we plot as a solid lines in figures 3.5.3(c,d).  $\beta_1$  is obtained by solving  $\varepsilon = 0.9\varepsilon^*$ , yielding

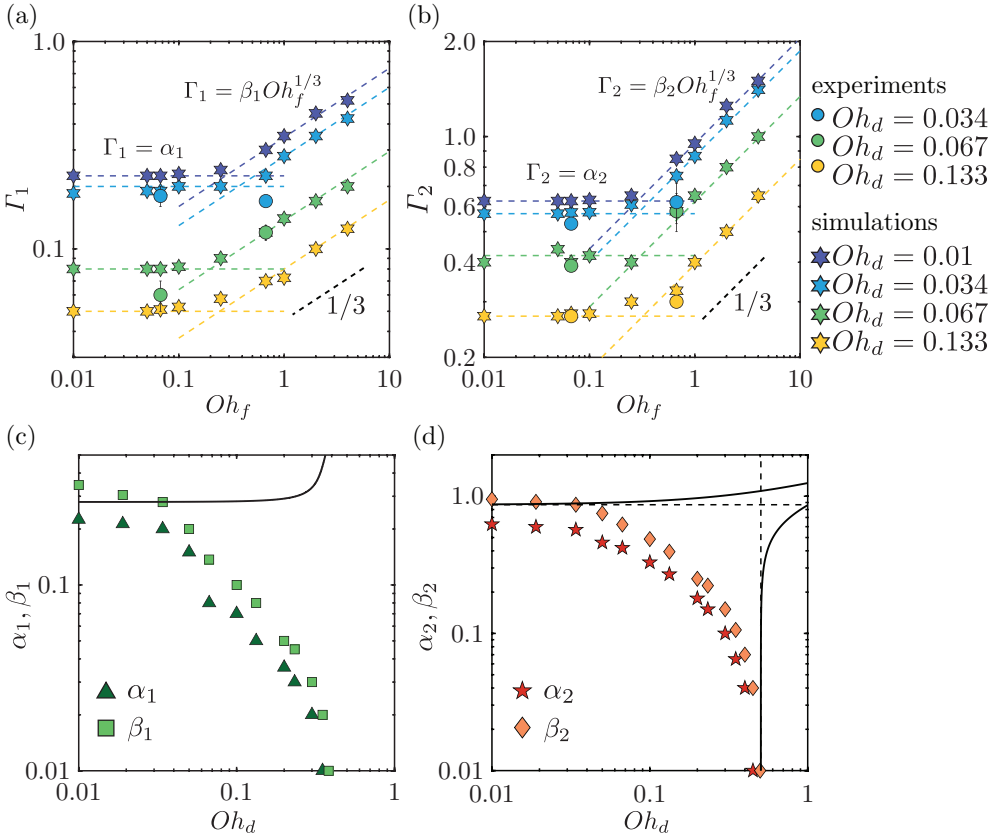


Figure 3.5.3: Critical film thickness marking the transition from (a) substrate-independent to substrate-dependent bouncing  $\Gamma_1$  and (b) bouncing to floating  $\Gamma_2$  as a function of  $Oh_f$  at different  $Oh_d$ . Prefactors (c)  $\alpha_1$  and  $\beta_1$ , and (d)  $\alpha_2$  and  $\beta_2$  as a function of  $Oh_d$ . The solid black line in panel (c) represents the model prediction for  $\beta_1$ , equation (3.19). The solid black lines in panel (d) represent the model predictions for  $\beta_2$  using equations (3.10)-(3.11), and the black dashed lines show the two asymptotes, equations (3.12)-(3.13).

$$\beta_1 = c_f^{1/3} \left[ \frac{-c_d Oh_d(1 - r^2) + 2r\sqrt{c_k(1 + r^2) - c_d^2 Oh_d^2}}{c_k(1 + r^2)} \right]^{1/3}, \quad (3.19)$$

$$\text{where, } r = \frac{c_d Oh_d}{\sqrt{4c_k - c_d^2 Oh_d^2}} - \frac{\ln(0.9)}{\pi}, \quad (3.20)$$

and  $\beta_2$  is given by equation (3.11). The model fails to capture both the decrease of  $\beta_1$  and  $\beta_2$  with  $Oh_d$ . Yet, we can interpret the evolution of these two prefactors along the inviscid and viscous drop limiting cases. Indeed, for inviscid drops (i.e., small  $Oh_d$ ), the model predictions for  $\beta_1$  and  $\beta_2$  show a plateau whose value is in good agreement with that reported in experiments. Conversely, for viscous drops (i.e., large  $Oh_d$ ),  $\beta_2$  decreases with  $Oh_d$  to match the asymptote associated to the substrate-independent bouncing inhibition occurring at  $Oh_{d,c} \approx 0.5$  (equation (3.10) and dotted line in figure 3.5.3d).

We stress that the model predictions shown in figures 3.5.3(c,d) consider a unique value of  $c_f = 0.46 \pm 0.1$ , determined from least-square fit in § 3.4. We attribute the failure of the model to predict the dependence on  $Oh_d$  away from the two asymptotes to its simplified representation of the drop-film interactions. While these minimal oscillator based models remarkably predict the global outcome of a rebound, that is, for example, the contact time, coefficient of restitution, and the bounds of bouncing, they fail at accurately representing the interaction, such as the drop or film deformations (equation (3.14)), and their dynamics. For example, the force associated to drop impact is maximal at early times when the drop shape is spherical, while the force exerted by a spring is proportional to deformation. More intriguingly, the minimal model also breaks down for  $Oh_f \lesssim 0.1$ , where we observe that the coefficient of restitution does not depend on the film Ohnesorge number. We demystify this behavior in the next section.

### 3.6 Bouncing inhibition on low Ohnesorge number films

We now investigate the independence of the rebound elasticity with the film Ohnesorge number, illustrated by the data collapse of figure 3.5.1(a), for low values of  $Oh_f$ ,  $Oh_f \lesssim 0.1$ . Figure 3.6.1(a) shows two typical impact scenarios in this regime, with  $Oh_f = 0.01$  (figure 3.6.1(a - i)) and 0.1 (figure 3.6.1(a - ii)), where bouncing is inhibited by the presence of the liquid film. Although these

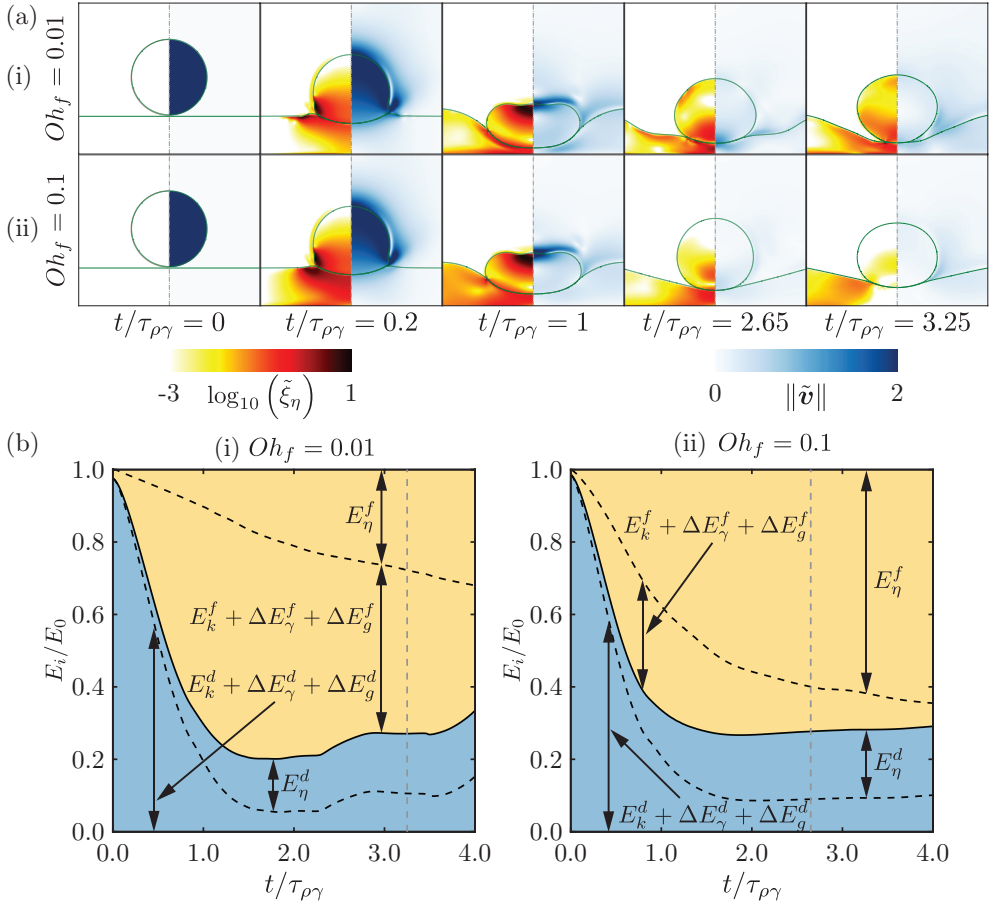


Figure 3.6.1:  $Oh_f$  independent inhibition of bouncing: (a) typical drop impact dynamics on low viscosity films. The snapshots show the dimensionless rate of viscous dissipation per unit volume ( $\tilde{\xi}_\eta = 2Oh(\tilde{\mathcal{D}} : \tilde{\mathcal{D}})$ ) on the left and the magnitude of dimensionless velocity field ( $\tilde{\mathbf{v}}$ ) on the right. We show  $\tilde{\xi}_\eta$  on a  $\log_{10}$  scale to identify regions of maximum dissipation (marked with black for  $\tilde{\xi}_\eta \geq 10$ ). and (b) Energy budgets for the two representative cases shown in panel (a), normalized by the available energy at the instant of impact. Here, the subscripts  $g$ ,  $k$ ,  $\gamma$ , and  $\eta$  denote gravitational potential, kinetic, surface, and viscous dissipation energies, respectively. The superscripts  $d$ ,  $f$ , and  $a$  represent drop, film and air, respectively. The grey dashed dotted line in each panel marks the instant when the normal reaction force between the drop and the film is minimum and represents the last time instant when the drop could have bounced off the film. In each panel,  $Oh_f =$  (i) 0.01 and (ii) 0.1. For all the cases,  $We, Oh_d, \Gamma = 4, 0.034, 1$ .

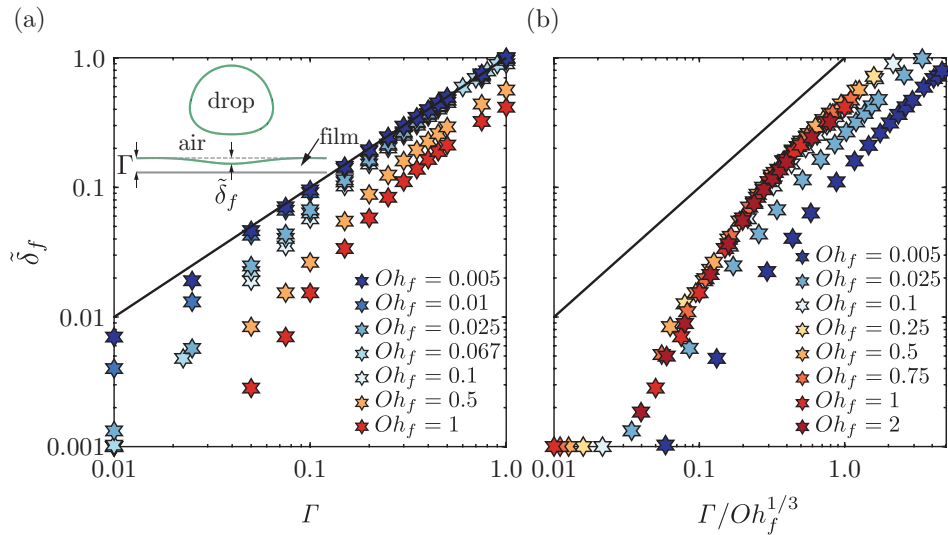


Figure 3.6.2: Variation of the maximum dimensionless film deflection  $\tilde{\delta}_f = \delta_f/R$  measured from the initial film free-surface as a function of (a) the film thickness  $\Gamma$  and (b) the effective film mobility  $\Gamma/Oh_f^{1/3}$  in the direct numerical simulations. The solid black line represents  $\delta_f/R = \Gamma$  and  $\delta_f/R = \Gamma/Oh_f^{1/3}$  in panels (a) and (b), respectively. The inset in panel (a) depicts the schematic representation of this film deflection  $\delta_f$ .

two representative cases differ by an order of magnitude in  $Oh_f$ , qualitatively, the drop shape and flow anatomy remain similar (figure 3.6.1a,  $t/\tau_{\rho\gamma} = 0.2, 1$ ), suggesting an equal loading on the film. Nonetheless, the film response varies. We observe capillary waves on the film-air interface for  $Oh_f = 0.01$ , which vanish for  $Oh_f = 0.1$  owing to increases viscous attenuation (figure 3.6.1a,  $t/\tau_{\rho\gamma} = 0.2, 2.65$ ).

To further elucidate the drop-film interaction, we compute the energy budgets associated to the two representative cases with  $Oh_f = 0.01$  (figure 3.6.1(b - i)) and 0.1 (figure 3.6.1(b - ii)). The overall energy budget reads

$$E_0 = \left( E_k^d + \Delta E_\gamma^d + \Delta E_g^d \right) + E_\eta^d + \left( E_k^f + \Delta E_\gamma^f + \Delta E_g^f \right) + E_\eta^f + E_t^a, \quad (3.21)$$

where  $E_0$  is the energy at impact (*i.e.* the sum of the drop's kinetic and gravitational potential energies). The subscripts  $g, k, \gamma$ , and  $\eta$  denote gravitational potential, kinetic, surface, and viscous dissipation energies, respectively. Moreover, the superscripts  $d, f$ , and  $a$  represent drop, film and air, respectively. Lastly, reference values to calculate  $\Delta E_g$  and  $\Delta E_\gamma$  are at minimum  $E_g$  and  $E_\gamma$  at  $t = 0$ , respectively. Note that the contribution of the total energy associated with air ( $E_t^a = E_k^a + E_\eta^a$ ) is negligible as compared to other energies ( $E_t^a(t/\tau_{\rho\gamma} = 4) \approx 0.01E_0$ ). Readers are referred to [3.6.1] for details of energy budget calculations.

In both cases, the magnitude of the drop energy (the sum of the drop's kinetic, gravitational and surface energies) at the end of the rebound cycle, that is for  $t = 3.25\tau_{\rho\gamma}$  when  $Oh_f = 0.01$  and  $t = 2.65\tau_{\rho\gamma}$  when  $Oh_f = 0.1$  (vertical grey dashed lines), is similar in the two representative cases of figure 3.6.1(b), as expected from the independence of  $\varepsilon$  with  $Oh_f$ . Note that the end of the cycle has been determined from the instant at which the reaction force between the drop and the film is minimum [see appendix 3.E and [3.6.1]]. Moreover, the energy budget evidences that the viscous dissipation in the drop during the rebound is similar, indicating that the magnitude of the energy transferred from the impacting drop to the film (the sum of the film's kinetic, gravitational and surface energies, and viscous dissipation) is not affected by the one order of magnitude change in  $Oh_f$ . Yet, the distribution of the film energy is dramatically different in the two cases we consider. For  $Oh_f = 0.1$ , the energy transferred to the film is mostly lost to viscous dissipation, while for  $Oh_f = 0.01$  the energy stored in the film's kinetic, surface and potential components dominates. We stress here that the  $Oh_f$ -independent behavior does not imply that dissipation is negligible. Indeed, the viscous

dissipation in the film accounts for approximately 40% and 85% of the total energy transferred to the film for  $Oh_f = 0.01$  and  $0.1$ , respectively. This difference in the film energy distribution hints at the failure of our assumptions to neglect the film's inertia and surface tension. The minimal model is relevant only when the energy transferred to the liquid film is predominantly lost to viscous dissipation.

Guided by the energy budget analysis in the above two extreme cases, we now evidence the minimal model failure through the break up of the effective film mobility analogy,  $\Gamma/Oh_f^{1/3}$ , which is intimately tied to the assumption of dominant viscous dissipation in the film. The maximum film deflection  $\delta_f$  controls its surface energy and velocity field (and hence the viscous dissipation). In figure 3.6.2, we report the normalized maximum film deflection  $\tilde{\delta}_f = \delta_f/R$  as a function of  $\Gamma$  (figure 3.6.2a) for  $Oh_f$  in the range  $0.01 - 2$  while keeping  $Oh_d$  constant. For  $Oh_f > 0.1$ , the deflection decreases with increasing  $Oh_f$ , and the data collapses once the horizontal axis is rescaled by  $Oh_f^{-1/3}$  (figure 3.6.2b), confirming the relevance of the proposed effective thickness. However, for lower film Ohnesorge numbers,  $\tilde{\delta}_f$  scales with  $\Gamma$  independent of  $Oh_f$  illustrating the limits of our hypotheses. Here, one might be tempted to replace the film damper in our model ( $c_f \eta_f \Gamma^{-3}$ ) with  $c_f \Gamma$  in this regime. However, such a replacement still fails to appropriately account for the kinetic and surface energies of the film. Indeed, low  $Oh_f$  films are associated to capillary waves, and the maximum deflection  $\delta_f$  might not be the correct length scale to mimic their behavior in a simplified model. As future work, it would be interesting to couple a linearized quasi-potential fluid model [? ? ] for the liquid pool/film with a spring-mass-damper system for the liquid drop to further investigate this regime.

### 3.7 Conclusions and outlook

In this work, we perform experiments and direct numerical simulations of the rebound of an oil drop impacting on a deformable oil film. We elucidate the role of the drop and film properties, the Ohnesorge numbers of the drop  $Oh_d$  and the film  $Oh_f$  and the film thickness  $\Gamma$ , on the impact process.

For films with a low Ohnesorge number (i.e.,  $Oh_f < 0.1$ ), figure 3.7.1 summarizes the different regimes identified in this work. For small film thicknesses, we recover the substrate-independent limit where bouncing is inhibited by the high viscous dissipation in the drop [ $Oh_{d,c} \sim \mathcal{O}(1)$ , ? ]. Increasing the film thickness reduces the drop Ohnesorge number marking the bounc-

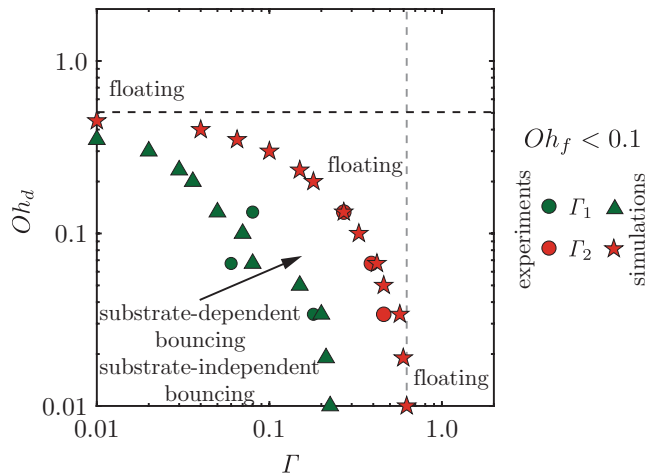


Figure 3.7.1: Regime map in terms of the drop Ohnesorge number  $Oh_d$  and dimensionless film thickness  $\Gamma$  for  $Oh_f < 0.1$ , showing the transitions between different regimes identified in this work.  $\Gamma_1$  marks the transition from substrate-independent bouncing to substrate-dependent bouncing whereas  $\Gamma_2$  marks the transition from bouncing to floating regimes. The black dotted line represents the substrate-independent asymptote for bouncing to floating transition (equation (3.12)), and the gray dotted line is drawn as a guide to the eye by using the numerical data and shows the inviscid drop asymptote for bouncing to floating transition.

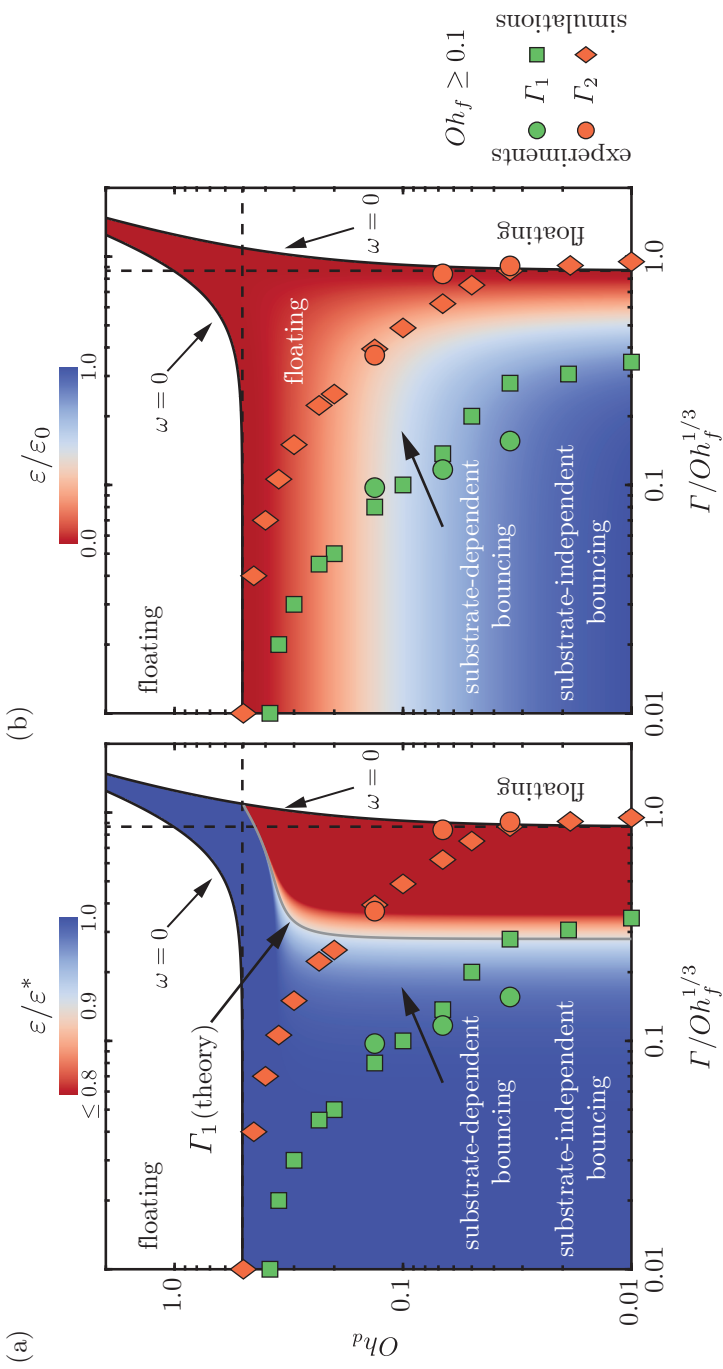


Figure 3.7.2: Regime map in terms of the drop Ohnesorge number  $Oh_d$  and modified dimensionless film thickness  $\Gamma/Oh_f^{1/3}$  for  $Oh_f \geq 0.1$  showing the transitions between different regimes identified in this work.  $\Gamma_1$  marks the transition from substrate-independent bouncing to substrate-dependent bouncing whereas  $\Gamma_2$  marks the transition from bouncing to floating regimes. The background contour illustrates the theoretical values of the coefficient of restitution  $\varepsilon$  (equation (3.18)) normalized with its (a) substrate-independent limit  $\varepsilon^* = \varepsilon\left(\Gamma/Oh_f^{1/3} \rightarrow 0\right)$ , equation (3.23) and (b) inviscid drop and substrate-independent limit  $\varepsilon_0 = \varepsilon^*(Oh_d \rightarrow 0)$ . The black solid lines shows the predicted bouncing to floating transition using the minimal phenomenological model ( $\omega = 0$ , equations (3.10)-(3.11)), and the black dashed lines show the two asymptotes (equations (3.12)-(3.13)) of bouncing to floating regimes. Lastly, the gray solid line shows the theoretical prediction of  $\Gamma_1$ .

ing to floating transition as additional energy is transferred to the film, and similarly influences the substrate-independent to substrate-dependent transition. In the inviscid drop limit, bouncing stops once a critical film thickness ( $\Gamma_2 \sim \mathcal{O}(1)$ ) is reached, independent of  $Oh_f$ . Here, the invariance of the energy transfer from the drop to the film with  $Oh_f$  remains to be explained and deserves further study.

For high Ohnesorge number films (i.e.,  $Oh_f > 0.1$ ), figure 3.7.2 summarizes the different regimes identified in this work. Similar to the low  $Oh_f$  case, increasing  $Oh_d$  and  $\Gamma$  inhibits bouncing. In contrast with the previous case, in the inviscid drop limit, the bouncing to floating transition occurs at critical film thicknesses that depend on the Ohnesorge number of the film as  $\Gamma_2 \sim Oh_f^{1/3}$ . We propose a minimal phenomenological model describing the key aspects of this process. The background colors in figures 3.7.2(a) and 3.7.2(b) illustrate the predicted values of the restitution coefficient  $\varepsilon$  (equation (3.18)) normalized with its substrate-independent  $\varepsilon^* = \varepsilon(\Gamma/Oh_f^{1/3} \rightarrow 0)$ , equation (3.23), and inviscid drop and substrate-independent  $\varepsilon_0 = \varepsilon^*(Oh_d \rightarrow 0)$  values, respectively. The model accurately predicts the substrate-independent and inviscid drop asymptotes corresponding to the bouncing to floating transition i.e.,  $\Gamma_2$ ). In the latter limit, the model also captures the substrate-independent to substrate-dependent transition (i.e.,  $\Gamma_1$ ). Away from these asymptotes, the minimal model fails to predict  $\Gamma_1$  and  $\Gamma_2$ . We attribute this shortcoming to the simplified representation of the drop-film interactions in the model. Nonetheless, notice that the predicted values of the restitution coefficient are very close to zero beyond the bouncing to floating transition observed in the simulations. We hypothesize that the model breakdown might be caused by the neglect of gravity which is known to inhibit bouncing [? ] and may prevent the take off of drops with small upward velocities. We refer the reader to [?] for a detailed study of the role of gravity in inhibiting the bouncing of viscous drops.

Finally, we stress that this study does not present an exhaustive exploration of all bouncing regimes. For example, [?] have shown that spherical hydrophobic solid spheres can bounce off deep low viscosity pools. Consequently, we hypothesize that the bouncing regime could resurrect at high  $Oh_d$ ,  $\Gamma$ , and low  $Oh_f$ , evidencing non-monotonic energy transfer. It will be interesting to probe such a regime in future work.



# Appendix

## 3.A Air layer rupture

We observe three distinct types of air layer collapse and describe their phenomenology in figure 3.A.1. Figure 3.A.1(a) illustrates the air layer break up at large Weber numbers. The air film fails during drop spreading as the intervening air layer drains below a critical thickness on the order of  $10 - 100$  nm, characteristic of the range of van der Waals forces [? ? ?].

Figure 3.A.1(b) evidences the influence of the drop Ohnesorge number  $Oh_d$  on the coalescence transition. Drops with low  $Oh_d$  show distinct pyramidal structures owing to the capillary waves after impact [? ]. The convergence of these capillary waves at the drop apex, during the retraction phase, can create an upward Worthington jet and an associated downward jet due to momentum conservation [? ? ? ]. This downward jet can puncture the air film and lead to coalescence during the drop retraction.

Lastly, the air layer can also break due to capillary waves propagating at the surface of the film owing to low  $Oh_f$  (see figure 3.A.1c).

In summary, figure 3.A.1 shows that the critical Weber number beyond which the air layer between the drop and the film ruptures is sensitive to the Ohnesorge numbers of both the drop as well as the film [? ? ]. Subsequently, the bouncing-coalescence transition can arrest the superamphiphobic-type rebounds discussed in this work. The analysis of this transition is beyond the scope of the present study and we refer the reader to [? ? ] for further discussion and review on this topic.

## 3.B Substrate independent bouncing

As the film thickness decreases or the film viscosity increases, the impact process becomes independent of the film properties. In this limit,  $\Gamma/Oh_f^{1/3} \rightarrow 0$ ,

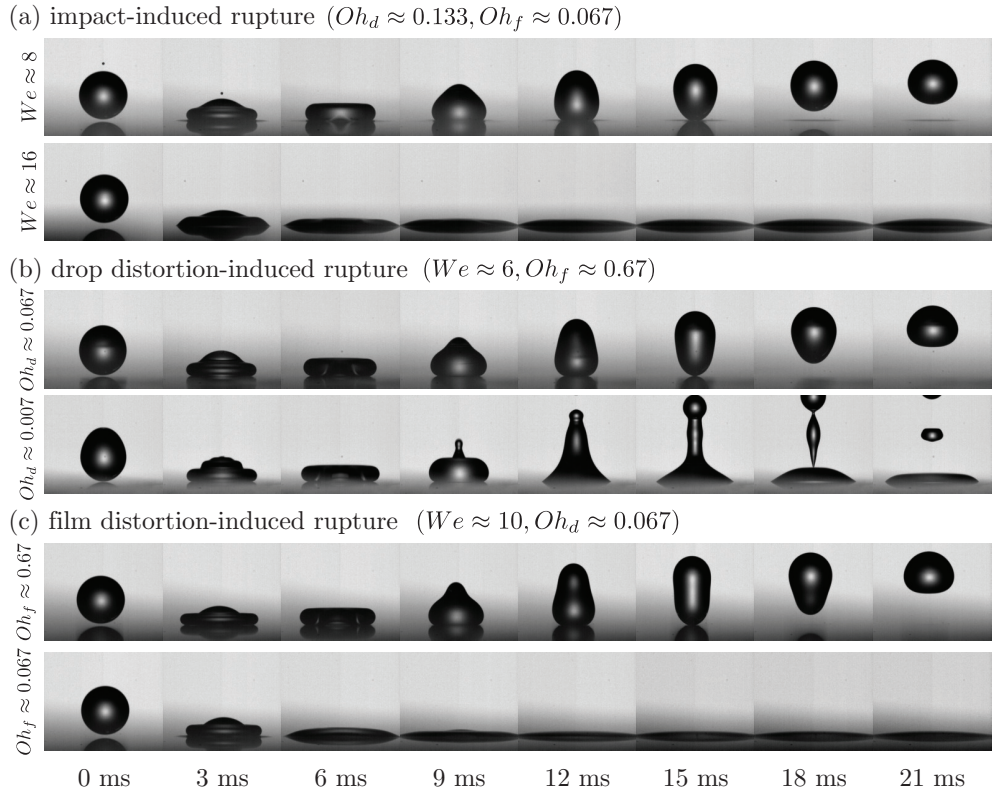


Figure 3.A.1: Rupture of the air layer and subsequent coalescence of impacting drop with the liquid coating. This rupture can occur due to: (a) impact as  $We$  increases, (b) pyramidal drop distortion and subsequent downward momentum jet as  $Oh_d$  decreases, and (c) film distortions due to capillary waves as  $Oh_f$  decreases. For panels (a) and (c),  $\Gamma = 0.03$ , and for panel (b)  $\Gamma = 0.01$  (dry-substrate limit). For all the cases,  $Bo \approx 0.5$ .

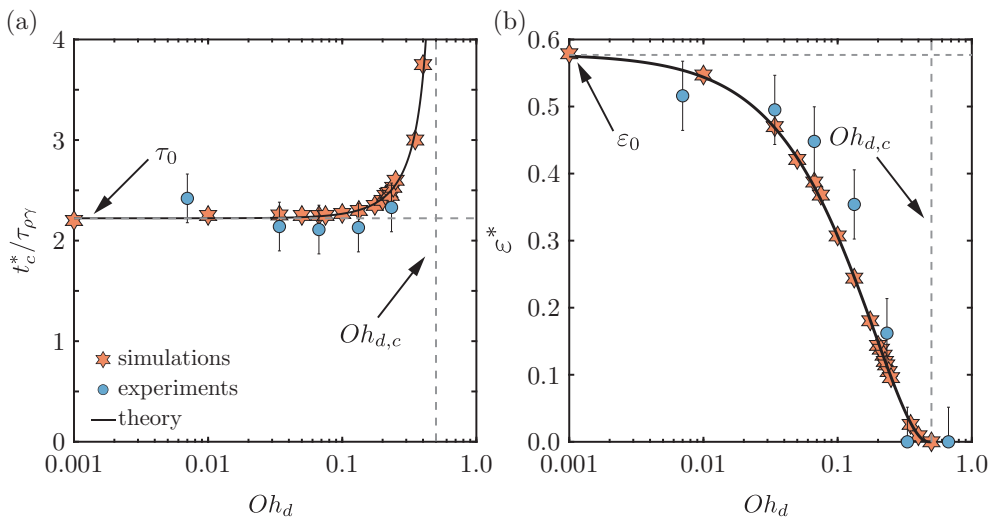


Figure 3.B.1: Substrate independent bouncing: (a) variation of contact time  $t_c^*$  normalized with inertia-capillary timescale  $\tau_{\rho\gamma}$ , and (b) coefficient of restitution  $\varepsilon^*$  with the drop Ohnesorge number  $Oh_d$ . The solid black lines represents the theoretical solutions, equations (3.22)-(3.23), in the substrate-independent limit which predicts an increase in contact time and an exponential decay in  $\varepsilon^*$  with  $Oh_d$ , and existence of a critical drop Ohnesorge number  $Oh_{d,c}$  (dashed vertical gray line). These predictions are consistent with [?], and set the prefactors  $c_k$  and  $c_d$  to  $2.0 \pm 0.1$  and  $5.6 \pm 0.1$ , respectively. Here,  $We = 4$  and  $Bo = 0.5$ .

the phenomenological model predictions for the contact time and restitution coefficient, equations (3.17) and (3.18), become

$$t_c^* = \tau_{\rho\gamma} \left( \frac{2\pi}{\sqrt{4c_k - c_d^2 Oh_d^2}} \right), \quad (3.22)$$

$$\varepsilon^* = \varepsilon_0 \exp \left( \frac{-\pi c_d Oh_d}{\sqrt{4c_k - c_d^2 Oh_d^2}} \right), \quad (3.23)$$

which is identical to the model developed by [? ]. Indeed, in the substrate independent limit, bouncing off an air layer is an idealization of bouncing off dry-superamphiphobic substrates [? ? ? ].

Reducing equation (3.22) to the case of low viscosity drops ( $Oh_d \rightarrow 0$ ), we get  $t_0/\tau_{\rho\gamma} = \pi/\sqrt{c_k}$ , as expected from the water-spring analogy [? ? ]. We thus determine the prefactor  $c_k$  by fitting the inviscid limit of our data ( $t_0 = 2.2\tau_{\rho\gamma}$ , figure 3.B.1a) yielding

$$c_k = \left( \frac{\pi}{t_0/\tau_{\rho\gamma}} \right)^2 \approx 2, \quad (3.24)$$

which is also consistent with the values of contact time reported earlier in the literature [? ] and agrees with the Rayleigh time period of drop oscillation [? ].

Furthermore, applying a least square fit to our experimental and numerical data for the coefficient of restitution, which decays exponentially with increasing  $Oh_d$  (figure 3.B.1b), allows us to fix  $c_d = 5.6 \pm 0.1$ . Lastly, the model predicts the existence of a critical Ohnesorge number  $Oh_{d,c} = 2\sqrt{c_k}/c_d \approx 0.5$  above which the drops do not bounce. This asymptote is in quantitative agreement with our data (see the dashed gray lines in figure 3.B.1).

Finally, we compare the above value of  $c_d$  to that obtained by [? ]. To do so, we note that [? ] further reduced equation (3.23) to  $\varepsilon^* \approx \varepsilon_0 \exp(-\alpha Oh_d)$ , where  $\alpha = 2.5 \pm 0.5$  fit all their experimental datapoints, independent of the impact Weber number. The equivalent fitting parameter in our case is  $\alpha = (\pi/2)c_d/\sqrt{c_k} \approx 6$ . This discrepancy can be attributed to the different values of the critical Ohnesorge number  $Oh_{d,c}$  which could stem from the Bond number variation between the two cases:  $(Oh_{d,c}, Bo) \approx (0.8, 0.2)$ , in [? ], and  $(0.5, 0.5)$  in this work. Exploring the influence of  $Bo$  is beyond the scope of this chapter and we refer the reader to chapter 2 for detailed discussions.

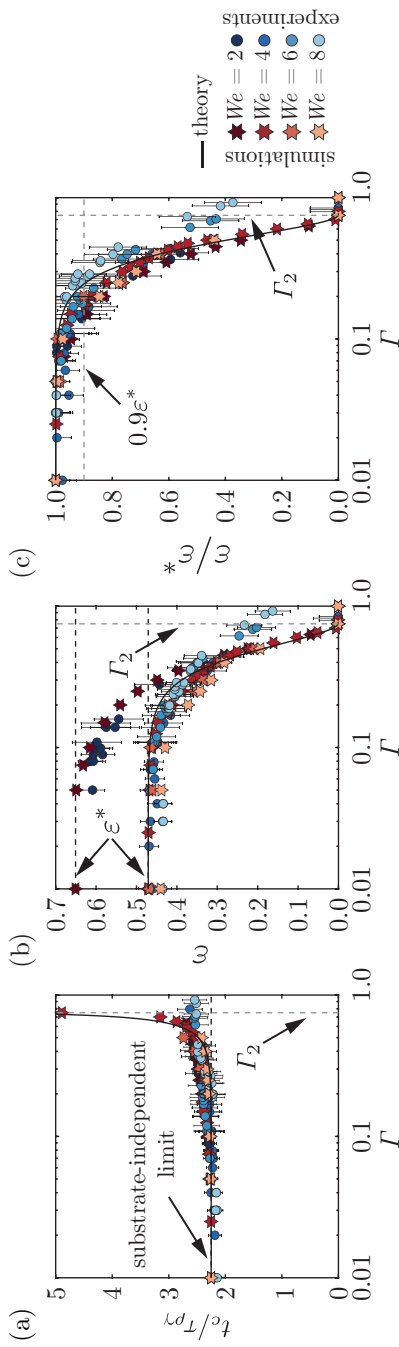


Figure 3.B.2: Influence of the impact Weber number on bouncing drops: variation of (a) time of contact  $t_c$  normalized with the inertio-capillary time scale  $\tau_{\rho\gamma}$ , (b) restitution coefficient, and (c) restitution coefficient normalized with its dry substrate value as a function of the dimensionless film thickness  $\Gamma$ . Here,  $(Oh_d, Oh_f) = (0.034, 0.67)$ . In each panel, solid black line represent the theoretical solution for  $(c_k, c_d, c_f) = (2, 5.6, 0.46)$  and the vertical dashed gray line indicate  $\Gamma_2$  above which drops do not bounce. In panels (a) and (b), black dashed lines show the dry substrate limit. Lastly, in panel (c), the horizontal dashed gray line denotes the  $0.9\varepsilon^*$  criterion used to determine the substrate-independent to substrate-dependent transition for bouncing drops.

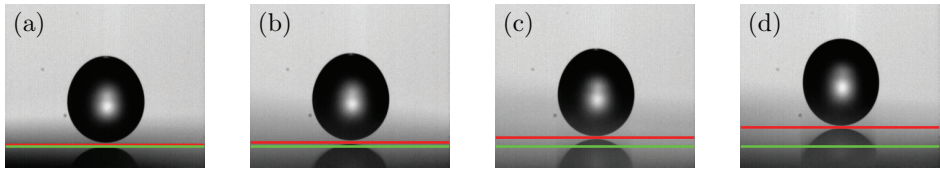


Figure 3.D.1: Side view snapshots of experiments at the instant of impact,  $t = 0$ . The images show the wall location denoted by a green horizontal line and the free-film interface denoted by a red horizontal line. The film thickness in each image is estimated from the vertical difference between the two lines which results in dimensionless film thickness of  $\Gamma = h_f/R =$  (a) 0.05 (b) 0.11 (c) 0.23, and (d) 0.48.

### 3.C Influence of the impact Weber number on bouncing drops

Figure 3.B.2 summarizes the influence of the Weber number  $We$  on the drop impact process for a representative case with  $Oh_d$  and  $Oh_f$  as 0.034 and 0.67, respectively. Notice that both the time of contact (figure 3.B.2a) as well as the coefficient of restitution (figure 3.B.2b) are fairly independent of  $We$  for  $We \geq 4$ . Surprisingly, small  $We$  shows a higher value of restitution coefficient, particularly in the substrate independent regime (see again figure 3.B.2b) owing to high capillary stresses that helps drops retain the spherical shape at take-off, increasing the efficiency of the bounce. Contrary to this scenario, more elongated shapes are observed for higher  $We$  (see figure 3.3.1a,b at take-off). Furthermore, normalizing  $\varepsilon$  with the  $We$ -dependent (at fixed  $Oh_d$ ) values in the dry substrate limit  $\varepsilon^*$ , we observe a collapse, similar to [?], insinuating that  $We$  only affects bouncing through this shape effect. Readers are referred to [?] for further discussions. Notice the discrepancy in determining  $\Gamma_2$  from experiments for higher  $We$  that we cannot explain at this point as the DNS do not match with experimentally obtained  $We$ -independent  $\Gamma_2$  in this regime.

### 3.D Measuring film thickness

Silicone oil films with thicknesses  $h_f < 30\text{ }\mu\text{m}$ , are prepared using spin coating and measured using reflectometry [?]. Thicker films ( $h_f > 30\text{ }\mu\text{m}$ ) are prepared by depositing a controlled volume of silicone oil on a glass slide. The film thickness is then measured using side view imaging by locating the vertical position of the glass slide wall (green line in figure 3.D.1) and of the film free surface (red line in figure 3.D.1). The uncertainty in the film thickness

measurement using this method is about  $\pm 30 \mu\text{m}$ , which corresponds to an uncertainty of about 3 pixels.

### 3.E Measuring the restitution coefficient

Throughout this chapter, we have used the coefficient of restitution to study the drop impact on thin films. In this appendix, we describe the procedure used to determine the restitution coefficient. In experiments, we measure the drop's maximum center of mass height relative to the undisturbed film surface to get the restitution coefficient as  $\varepsilon = \sqrt{2g(H - R)}/V$ , where  $V$  is the impact velocity. In simulations, we measure the coefficient of restitution as the ratio of the take-off velocity  $v_{\text{cm}}(t_c)$  to the impact velocity  $V$ ,

$$\varepsilon = \frac{v_{\text{cm}}(t_c)}{V} \quad (3.25)$$

where  $t_c$  denotes the contact time when the drop leaves the substrate film. The latter definition requires to precisely evaluate the contact time  $t_c$ . This is difficult as a thin film of air is always present between the drop and the film surface, we assume ideal non-coalescence between the drop and the film. In simulations, we automatize the detection of the end of apparent contact by taking  $t_c$  as the instant when the normal reaction force  $F(t)$  between the film and the drop is zero [for details on the force calculation, see chapter 1 and ? ]. Subsequently, we read out the center of mass velocity at this instant. If this center of mass velocity  $v_{\text{cm}}(t_c)$  is not in the upward direction (i.e., it is zero or negative), we categorize the case as non-bouncing.

### 3.F Code availability

The codes used in the present chapter are permanently available at ? ].

### 3.G Supplemental movies

These supplemental movies are available at ? ].

In all these videos, the left part of the numerical video shows the dimensionless local viscous dissipation rates on a  $\log_{10}$  scale, and the right part shows the velocity field magnitude normalized with the impact velocity. Also see figure 3.3.1.

chapter 3: drop impact on viscous liquid films



source code



supplemental movies

- SM1: Comparison of the experimental and DNS snapshots of the impact process on films with  $h_f = 0.01$  mm. In the experiment,  $R = 1$  mm,  $V = 0.3$  m/s,  $\eta_d = 4.6$  mPa.s and  $\eta_f = 96$  mPa.s, giving  $(We, Oh_d, Oh_f) = (4, 0.034, 0.67)$ .
- SM2: Comparison of the experimental and DNS snapshots of the impact process on films with  $h_f = 0.35$  mm. In the experiment,  $R = 1$  mm,  $V = 0.3$  m/s,  $\eta_d = 4.6$  mPa.s and  $\eta_f = 96$  mPa.s, giving  $(We, Oh_d, Oh_f) = (4, 0.034, 0.67)$ .
- SM3: Comparison of the experimental and DNS snapshots of the impact process on films with  $h_f = 0.85$  mm. In the experiment,  $R = 1$  mm,  $V = 0.3$  m/s,  $\eta_d = 4.6$  mPa.s and  $\eta_f = 96$  mPa.s, giving  $(We, Oh_d, Oh_f) = (4, 0.034, 0.67)$ .

## Chapter 4

# Lifting a sessile oil drop with an impacting one<sup>o</sup>

Colliding drops are widely encountered in everyday technologies and natural processes, from combustion engines and commercial sprays to raindrops and cloud formation. The outcome of a collision depends on many factors, including the impact velocity and the degree of head-on alignment, in addition to intrinsic properties like surface tension. Yet little is known about the dynamics of an oil drop impacting an identical sessile drop sitting on a low-wetting surface. We experimentally and numerically investigate such a binary impact dynamics of low surface tension oil drops on a superamphiphobic substrate. We observe five rebound scenarios, four of which do not involve coalescence. We describe two previously unexplored cases for sessile oil drop lift-off, resulting from a drop-on-drop impact event. The simulations quantitatively reproduce all rebound scenarios and enable quantification of the velocity profiles, the energy transfers, and the viscous dissipation. Our results illustrate how varying the offset from head-on alignment and the impact velocity results in controllable rebound dynamics for low surface tension drop collisions on superamphiphobic surfaces.

---

<sup>o</sup>Published as: Olinka Ramírez-Soto, **Vatsal Sanjay**, Detlef Lohse, Jonathan T. Pham, and Doris Vollmer. *Lifting a sessile oil drop with an impacting one*, Sci. Adv. **6**, eaba4330 (2020). Experiments are done by Ramírez-Soto; simulations by Sanjay; analysis by both; and supervision by Lohse, Pham, and Vollmer. Writing and proofread by everyone.

## 4.1 Introduction

When a liquid drop impacts a sessile one of an identical liquid, it is intuitively expected that both drops coalesce. This process is commonly observed in day-to-day examples, such as rain or drops from a leaky faucet. However, coalescence can be obstructed by a thin layer of air between the two drops [? ? ? ]. Insufficient thinning of this air layer during impact even enables water drops to bounce from perfectly hydrophilic surfaces, which they would otherwise wet [? ? ? ]. In the late 1800s, [?] noticed that water drops can glide over a pool because of this air layer. Analogously, a vapor layer also governs the Leidenfrost effect [? ? ? ? ? ? ], where a drop hovers over a superheated surface. As a result, drop bouncing, coalescence, and spreading can all be observed depending on the intrinsic properties of the liquid, as well as external parameters, such as the background pressure, collision velocity, and the impact parameter describing whether the collision is head-on or off-centered [? ? ? ? ]. Despite this progress in the experimental characterization of the impact dynamics, a quantitative modelling of the velocity fields and energy transfer is lacking, especially for non-aqueous liquids.

Drop impact on surfaces, and the outcome of the collision, is of practical importance for many situations. For example, in agriculture, it is essential to ensure that pesticides and other chemicals sprayed on wet leaves do not roll off and contaminate the surroundings [? ]. Surfactants are often added to lower or tune interfacial tensions. Impact of low interfacial tension drops are encountered in spray coating, inkjet printing, and additive manufacturing of low surface tension liquids [? ? ]. On the other hand, removal of drops is desirable for car windows [? ] and self-cleaning of surfaces. On super-hydrophobic surfaces, a water drop impacting another one can lead to drop removal after coalescence if sufficient energy is exchanged between them during impact without viscous dissipation [? ? ]. Alternatively, even without an impact, the coalescence of droplets can lead to jumping if the excess surface energy released is efficiently transferred to the kinetic energy [? ? ? ? ].

While several reports exist on understanding how a water drop impacts a sessile water drop on a surface [? ? ? ? ? ], the dynamics of a low surface tension oil drop impacting an oil drop on a non-wetting surface remains unexplored. A better understanding is, for example, desired in the emerging field of additive manufacturing. For example, in 3D printing, which is one of the widely used additive manufacturing techniques, the relative precision of the drop deposition and its shape evolution may decide the success or failure

of a printed device. It has been shown that the collisional dynamics of free-flying oil drops offer more diverse outcomes than those of water drops [? ? ]. Consequently, a number of questions arise. Do these collisions show rich dynamics also in the presence of a low-wetting surface? What are the outcomes of the drop-on-drop impact of oil on a superamphiphobic surface? How is energy transferred between the drops? Intuitively, the rebound of oil drops from a surface by impact with another oil drop seems more difficult than water for the following reasons. (i) The surface tension of most hydrocarbon oils ( $\approx 25 \text{ mN/m}$ ) is significantly lower than that of water ( $72 \text{ mN/m}$ ) which reduces the transfer of surface energy to kinetic energy during the coalescence. This transfer inefficiency implies that the drops have less energy to rebound. (ii) Sessile oil drops typically have a large contact size. On a flat surface, the receding contact angle is typically below  $60^\circ$  and often close to zero [? ]. Consequently, receding oil drops easily rupture before coming off the surface. (iii) On a superamphiphobic surface, oil drops display large apparent contact angles [? ? ]. However, the true liquid-solid contact angle is still small, leaving oil drops in a metastable state; that is, they can percolate into the surface [? ]. Moreover, pressure as low as a few hundred pascals is sufficient to transition the drop from the metastable Cassie state to a state where the drop wets the surface thoroughly [? ? ]. The energy threshold needed for this transition is related to the so-called impalement pressure that depends on details of the coating and the liquid under investigation [? ]. (iv) The low surface tension of oil means that the drop is easily deformable, which may give rise to enhanced viscous dissipation and energy loss upon impact. The drop can also locally impale the surface during impact [? ? ]

In this chapter, we experimentally and numerically investigate the dynamics of a low surface tension oil drop impacting a sessile drop of the same liquid, resting on a superamphiphobic surface (figure 4.2.1a). Indeed, we find that the impacting oil drop can lift the resting drop off the surface, without ever coalescing. Notably, we find four rebound scenarios without coalescence: (i) both drops rebound, (ii) two scenarios where the impacting drop rebounds while the sessile drop remains on the substrate, and (iii) the sessile drop rebounds while the impacting drop remains on the surface. We illustrate how these impact outcomes are governed by the Weber number ( $We$ , ratio of inertial to capillary stresses) and the extent of dimensionless offset from a head-on collision ( $\chi = d/(2R)$ , where  $R$  is the radius of each drop, and  $d$  is the distance between their centers of masses, see figure 4.2.1b). Direct numerical simulations provide a quantitative description of (i) the velocity of both drops

and of the surrounding vapor phase, (ii) how energy is transferred between the two drops during impact, and (iii) the viscous dissipation during impact and rebound. This allows for a quantitative comparison of experimental and numerical data of the rebound dynamics.

This chapter is organized as follows: § 4.2 briefly describes the experimental and numerical methods. We then explore the drop-on-drop impact by elucidating the experimental observations in § 4.3, followed by direct numerical simulations in § 4.4 where we reproduce the experimentally observed regimes and delve into the process dynamics using internal flow inside the two drops and the energy transfers between them. Lastly, the chapter ends with conclusion and outlook in § 4.5.

## 4.2 Method

In our experiments, a sessile oil drop is gently positioned on a superamphiphobic surface and then impacted with an identical second oil drop (figure 4.2.1a). The superamphiphobic surface is composed of a  $\sim 20\text{ }\mu\text{m}$  thick layer of templated candle-soot [? ? ]. Candle soot consists of a porous network of  $50 \pm 20\text{ nm}$  sized carbon nanobeads. Making use of chemical vapor deposition (CVD) of tetraethyl orthosilicate (TEOS) catalyzed by ammonia, a  $25\text{ nm}$  thick layer of silica is deposited over the porous nanostructures to increase the mechanical stability of the fragile network (figure 4.2.1a). The soot-templated silica network is fluorinated with trichloroperfluorooctylsilane to lower the surface energy, producing a superamphiphobic surface which repels water and most oils. As a model oil, we use hexadecane for its low surface tension, low volatility, homogeneous properties and Newtonian behavior. A drop of hexadecane (figure 4.2.1a-ii) exhibits an apparent contact static angle of  $\Theta^{\text{app}} = 164^\circ \pm 1^\circ$ . For further details of the drop-substrate contact angle, see appendix 4.A.

For our drop impact studies, a sessile drop of hexadecane is gently placed on this superamphiphobic surface with a needle connected to a syringe pump (dosing rate:  $2\text{ mL/h}$ ). When gravity exceeds the drop-needle adhesion, the drop releases from the needle; this results in a drop volume of  $V \approx 3\text{ }\mu\text{L}$  (figure 4.2.1a). This volume corresponds to a Bond number of  $0.3$  ( $Bo = \rho_l g R^2 / \gamma$ , ratio of gravitational to capillary stresses, where  $\rho_l$  is the density of the liquid,  $g$  is the gravitational acceleration, and  $R$  is the radius of a spherical droplet of identical volume). Note that a low Bond number implies that a spherical cap can describe the drop. However, it does not provide insight

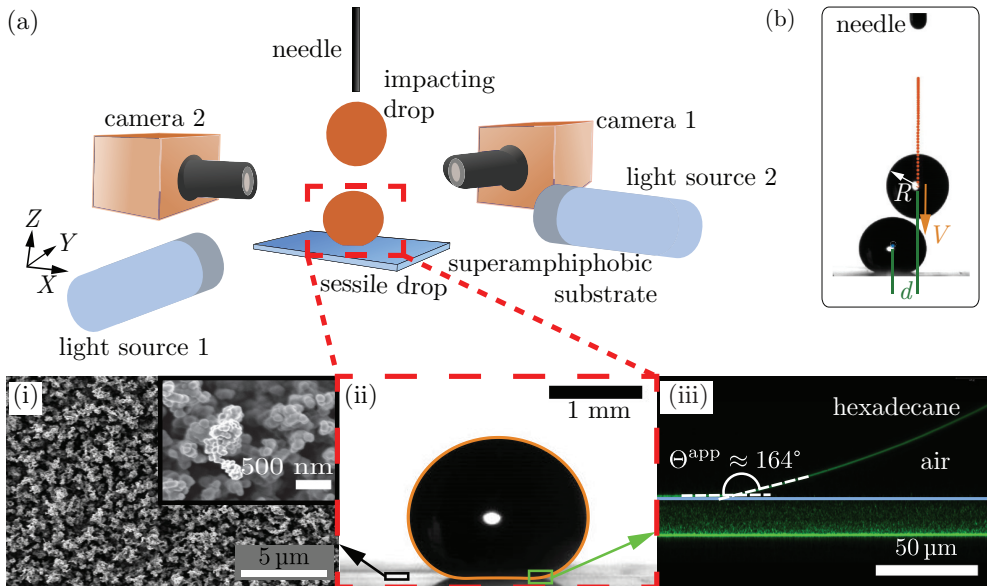


Figure 4.2.1: Experimental approach and the sessile drop: (a) Sketch of the experimental setup for binary drop impact on superamphiphobic surfaces. The needle is fixed to set the impacting height in the  $Z$  direction, and the relative distance between the sessile and impacting drops. The sessile drop is first centered along the  $YZ$  plane. Then the impacting drop is dispensed from the needle while the impact event is monitored with camera 2. Camera 1 is used to determine the relative positions of the drops in the  $X$  direction. The cameras and the light sources are aligned to observe the impact both in the  $XZ$  and  $YZ$  planes. Insets: (i) scanning electron micrograph (SEM) image of a soot-templated surface at two magnifications. (ii) hexadecane drop ( $V \approx 3 \mu\text{l}$ ) resting on the superamphiphobic surface. The orange contour is the solution of the Young-Laplace equation [? ] for a corresponding Bond number  $Bo = 0.3$ . (iii) confocal microscopy image showing a drop of hexadecane on the superamphiphobic surface (the blue line marks its approximate position). The image illustrates the apparent contact angle of the drop with the surface ( $\Theta^{\text{app}} \approx 164^\circ$ ). The image is taken in reflection mode, i.e., no dye was added to the hexadecane. Reflection of light results from the differences between the refractive indices of hexadecane (1.43), air (1.0), glass and silica ( $\approx 1.46$ ). The superamphiphobic layer consists mostly of air, and thus its refractive index is close to 1. Therefore, the horizontal glass-superamphiphobic layer and the hexadecane-superamphiphobic layer interfaces are clearly visible. The superamphiphobic layer itself is visible as a diffuse pattern, resulting from the reflection of light from the silica nanoparticles. (b) Image showing an off-center collision. The impact parameter is  $\chi = d/(2R)$ .

on whether the drop passes the Cassie-to-Wenzel transition. Nonetheless, the shape of the drop is important as it forms the initial condition for the numerical simulation. To calculate and confirm this shape numerically, we solve the Young – Laplace equation [? ]. The shape matches well with the experiments (see the orange contour in figure 4.2.1a-ii). The substrate is then translated laterally to position the sessile drop in the  $X$  and  $Y$  directions.

At an identical dosing rate, a second drop is released with an identical volume,  $\mathcal{V} \approx 3 \mu\text{L}$ , which impacts the sessile drop. The control parameters of the drop collision, determining the outcome, are the Weber number ( $We$ ), which is related to the impact velocity ( $V$ ), and the impact parameter ( $\chi$ ), which describes the offset from head-on alignment of the two colliding drops. The impact velocity  $V$  is controlled by varying the height of the dispensing needle from the substrate (figure 4.2.1a). The corresponding Weber number  $We = \rho_l V^2 R^2 / \gamma$  compares fluid inertia and surface tension, where  $\rho_l = 770 \text{ kg/m}^3$  is the density of the hexadecane and  $\gamma = 27.5 \text{ mN/m}$  is its surface tension coefficient. In our experiments, the Weber number ranges from 0.02 to 9. Two synchronized high-speed cameras are perpendicularly positioned to capture the dynamics of the drops in the  $X$ ,  $Y$ , and  $Z$  directions. The impact parameter of the two drops is given by the ratio  $\chi = d / (2R)$ , where  $d$  is the horizontal offset of the center of masses of the impacting drop and the sessile drop (figure 4.2.1b). Although we cannot exactly predict the impact parameter beforehand, the two camera system allows us to precisely measure the offset from head-on alignment by image analysis.  $\chi = 0$  describes a perfect head-on collision whereas  $\chi = 1$  corresponds to the situation when the two drops merely brush each-other ( $d = 2R$ ).

### 4.3 Experimental observations

When varying the offset from head-on alignment  $\chi$  and the Weber number  $We$  independently, six outcomes for the impact dynamics are observed, termed Cases I-VI (figure 4.3.1). The column A of images is taken just as the collision starts ( $t = 0 \text{ ms}$ ) and is used to quantify the impact parameter,  $\chi$ . Column B is at the point of maximum sessile drop compression, and column C demonstrates the shape of both drop just before they separate or coalesce. Column D illustrates the overall outcome of the collision event. We first consider the outcomes at  $We \approx 1.5$  while varying  $\chi$ . For a near zero  $\chi$ , Case I is observed, which is a head-on collision (figure 4.3.1-I, supplemental movies 1–3). During impact, both drops deform and spread radially, and as a result, show axial

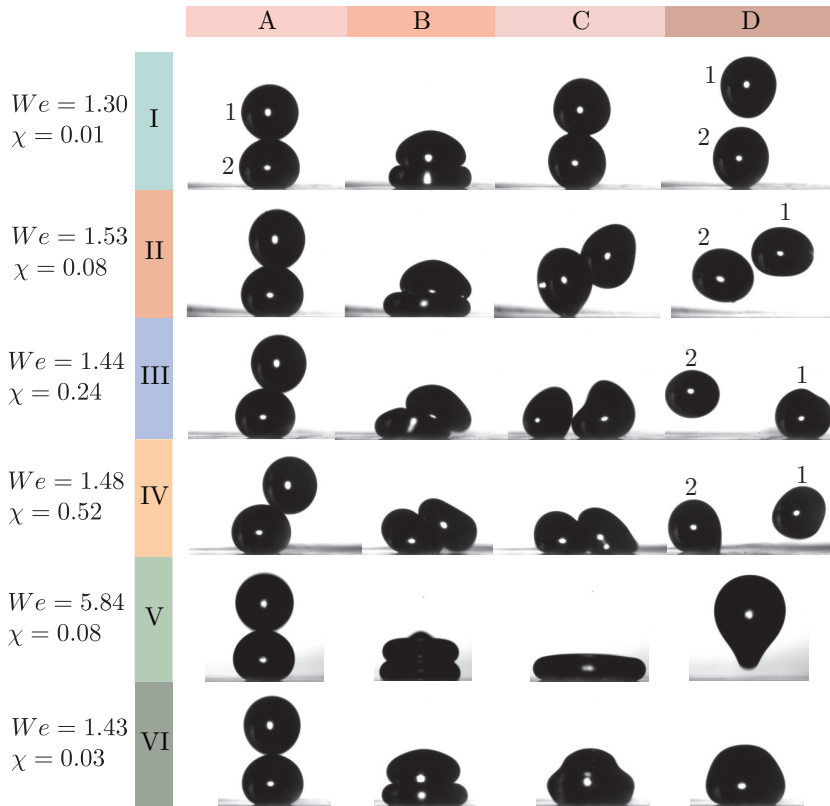


Figure 4.3.1: Snapshots of the impact dynamics: note that the drop labels 1 and 2 are for the impacting and sessile drop, respectively. Six outcomes (Cases I – VI) are observed when varying the impact parameter  $\chi$  and the Weber number  $We$  independently. The rows correspond to different impact parameter for I-VI. The columns show characteristic stages of the collision process. A: just at collision, B: sessile drop at maximum compression, C: droplet shape just before separation or coalescence. D: final outcome of the impact. Volume of both drops is  $3 \mu\text{L}$ . Case I,  $We = 1.30$  and  $\chi = 0.01$ : the time stamp for each frame is:  $t_A = 0 \text{ ms}$ ,  $t_B = 8 \text{ ms}$ ,  $t_C = 20 \text{ ms}$ ,  $t_D = 25 \text{ ms}$ . Case II,  $We = 1.53$ ,  $\chi = 0.08$ :  $t_A = 0 \text{ ms}$ ,  $t_B = 8 \text{ ms}$ ,  $t_C = 20 \text{ ms}$ ,  $t_D = 24 \text{ ms}$ . Case III,  $We = 1.44$ ,  $\chi = 0.24$ :  $t_A = 0 \text{ ms}$ ,  $t_B = 8 \text{ ms}$ ,  $t_C = 20 \text{ ms}$ ,  $t_D = 24 \text{ ms}$ . Case IV,  $We = 1.48$ ,  $\chi = 0.52$ :  $t_A = 0 \text{ ms}$ ,  $t_B = 5.5 \text{ ms}$ ,  $t_C = 7 \text{ ms}$ ,  $t_D = 21 \text{ ms}$ . Case V,  $We = 5.84$ ,  $\chi = 0.08$ :  $t_A = 0 \text{ ms}$ ,  $t_B = 3.75 \text{ ms}$ ,  $t_C = 8.5 \text{ ms}$ ,  $t_D = 25.5 \text{ ms}$ . Case VI,  $We = 1.43$ ,  $\chi = 0.03$ :  $t_A = 0 \text{ ms}$ ,  $t_B = 7.5 \text{ ms}$ ,  $t_C = 9 \text{ ms}$ ,  $t_D = 17 \text{ ms}$ .

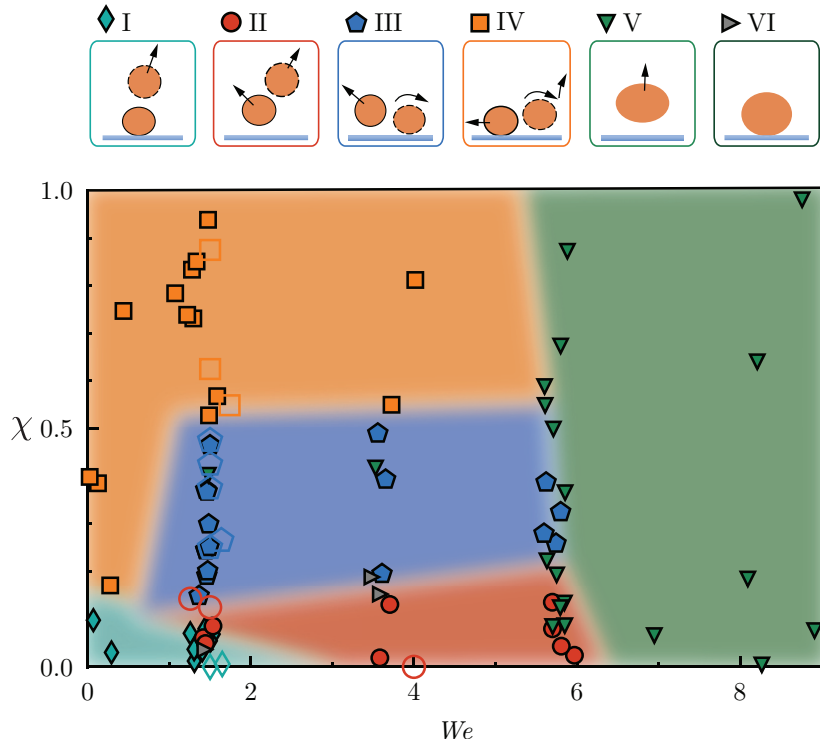


Figure 4.3.2: Regime map illustrating the observed cases as a function of the impact parameter  $\chi = d/(2R)$  and Weber number  $We$ . The top sketches with the respective Roman case number are the possible outcomes after the hexadecane drop impacted on the sessile hexadecane drop. In the image strip, the sessile drop is represented with the solid outline, and the impacting drop with the dotted outline. The arrows represent the direction of motion after impact for each drop. In case III, the impacting drop has a horizontal-curved arrow that represents the rolling of the drop over the sessile drop. In case IV, the impacting drop has two associated arrows. The horizontal-curved arrow represents rolling over the sessile drop and the vertical arrow denotes bouncing after the impact event. Each possible outcome is marked by a color and symbol for identification and corresponds to the sketched cases I-VI. Closed symbols correspond to experiments and open ones to numerical simulations. The transition zones between the different scenario regions are not sharp. The colors assigned to the different cases are meant as a guide to the eye.

compression. The kinetic energy of the system is transferred to the surface energies of both the deformed drops. Moving forward in time, both drops start to retract. The sessile drop transfers energy back to the impacting drop in the form of kinetic energy. Upon completion of the collision, the impacting drop bounces off while the sessile drop stays on the substrate. The sessile drop also oscillates, hinting that it retains a part of the energy gained during impact. For a slightly higher offset,  $\chi \lesssim 0.15$ , Case II is observed (figure 4.3.1-II, supplemental movies 4–6). The initial collision is similar to Case I in that the drops collide, followed by vertical compression and lateral spreading. However, unlike Case I, the deformations are no longer symmetric, and the sessile drop also lifts off the surface. The displacement for either drop with respect to the center of mass of the initial sessile drop is in opposing lateral directions. Further increasing of the offset from head-on alignment to  $\chi \lesssim 0.5$ , the impacting drop glides over the sessile drop and rolls on the substrate, as illustrated by Case III (figure 4.3.1-III,  $\chi = 0.24$ , supplemental movies 7–9). Unlike Cases I and II, no rebound of the impacting drop is observed. Surprisingly, the sessile instead drop lifts-off the surface. As the impact parameter is increased even further ( $\chi > 0.5$ , Case IV), the impacting drop still rolls over the sessile drop (figure 4.3.1-IV, supplemental movies 10–12). However, during retraction, the impacting drop rebounds from the surface while the sessile drop moves along the surface.

In the above Cases I–IV, the Weber numbers were kept constant at  $We \approx 1.5$  while the offset was varied. However, the outcome of the impact event also varies with the Weber number. To provide a better intuition on how both  $\chi$  and  $We$  affect the observed outcomes, we plot our data as a phase diagram (figure 4.3.2). For  $We \geq 6$ , regardless of the impact parameter  $\chi$ , we find coalescence of the two drops, as illustrated in Case V (figure 4.3.1-V, supplemental movie 13). In this regime, the air layer between the drops is unstable which results in direct contact and subsequent coalescence. The coalesced drop reaches a maximum spreading diameter during impact (column C in figure 4.3.1-V). During retraction, the drop elongates vertically and ultimately detaches from the surface. Occasionally, drops coalesce without subsequent bouncing (Case VI, figure 4.3.1-VI, supplemental movie 14). Although this outcome is rarely observed and likely caused by surface defects, we present this result for the sake of completeness to demonstrate all observed outcomes. Moreover, to consider the generality of the scenarios presented for oil-on-oil drop impact, we also tested water-on-water drop impact. Similar scenarios are observed, as illustrated in figure 4.B.1.

## 4.4 Direct numerical simulations

Although the experimental observations consistently illustrate how  $We$  and  $\chi$  dictate the observed impact outcomes, they lack detailed information on the velocity fields and how energy is transferred between the two drops. To access this information, we ran direct numerical simulations (DNS) and compared these results with our experimental data. For simulating non-coalescing droplets, we employ geometric Volume of Fluid (VoF) [? ?] method with two distinct VoF tracers (see § 4.C for detailed discussions and implementation). This formulation ensures that drops cannot coalesce, reflecting the experimental situation where a finite air layer between the drops is preserved throughout the process.

We first ran four simulations choosing  $We$  and  $\chi$  values within the regimes for Cases I-IV, as denoted by the open symbols in figure 4.3.2. The results are displayed in figure 4.4.1. The normalized times ( $\tilde{t} = t/\tau_{\rho\gamma}$ , where  $\tau_{\rho\gamma} = \sqrt{(\rho_l R^3)/\gamma}$  is the inertio-capillary time scale.) correspond to the stages of the process, as described by columns A – D in figure 4.3.1. As is evident from the top rows (orange drops), the simulations reproduce the general collision outcomes consistent with the snapshots of the impact dynamics (figure 4.3.2). Moreover, the direct numerical simulations allow for quantifying the velocity vector fields for each of the cases (figure 4.4.1, bottom rows). These vector fields, combined with a calculation of the energy budget, renders it possible to quantitatively explore the dynamics of the oil drop-on-drop collision process. To account for the kinetic energy  $E_k$ , gravitational potential energy  $E_g$ , surface energy  $E_\gamma$ , and viscous dissipation  $E_\eta$ , we numerically calculated the total energy of the system as

$$E = E_m + E_\gamma + E_\eta, \quad (4.1)$$

where the energies are calculated using a method similar to the one developed by ? ]. Note that  $E_k$  includes the kinetic energy of the center of mass as well as the oscillation and rotational energies obtained in the reference frame that is translating with the center of mass of the individual drops. The details of these calculations are provided in § 4.D.

While keeping the Weber number at  $We = 1$ , the cases appear in order from I to IV with increasing offset position from head-on alignment  $\chi$ . For all cases, the energy is initially contained in the mechanical energy of the impacting drop (i.e., its kinetic and potential energy) and the surface energy

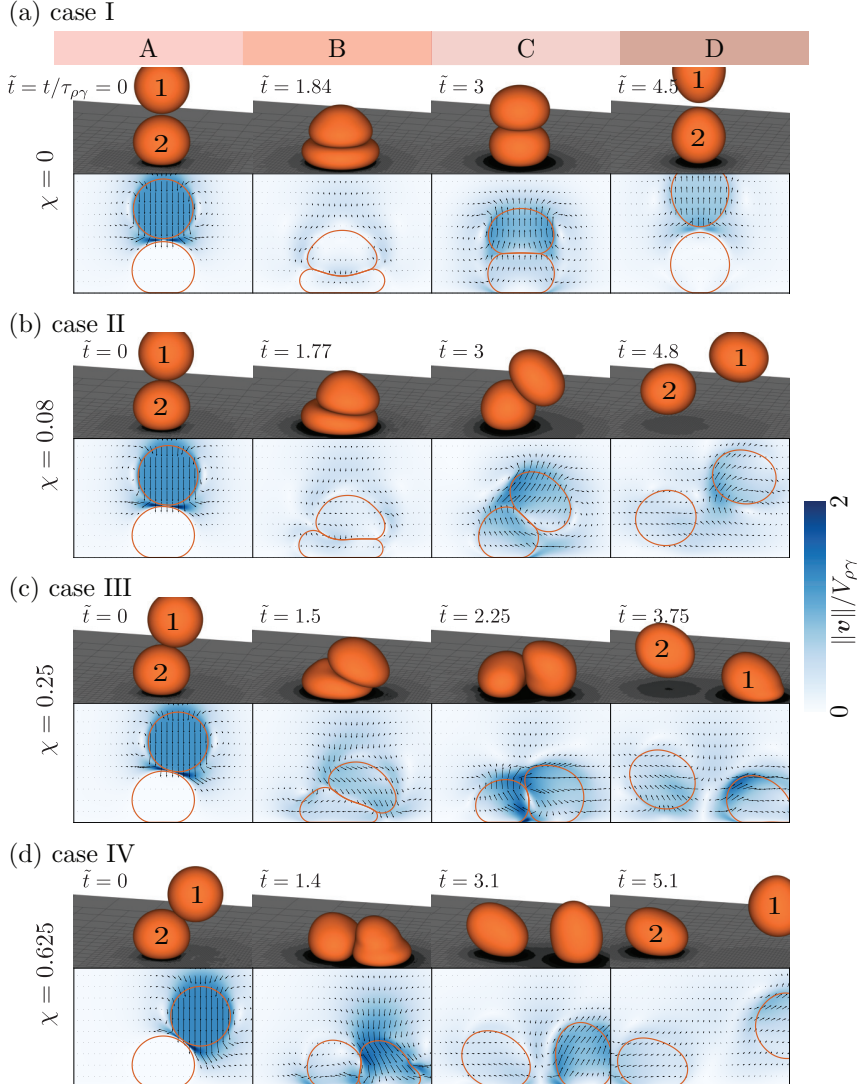


Figure 4.4.1: Snapshots from direct numerical simulations: illustration of different phases of drop-on-drop collisions and the subsequent outcomes. (a) Case I: ( $\chi = 0$ ) impacting drop bounces back and the sessile drops stays on the substrate, (b) Case II: ( $\chi = 0.08$ ) impacting drop bounces back and the sessile drop lifts-off from the substrate, (c) Case III: ( $\chi = 0.25$ ) impacting drop stays on the substrate and the sessile drop lifts-off, and (d) Case IV: ( $\chi = 0.625$ ) impacting drop bounces back and sessile drop stays on the substrate. For all these cases,  $We = 1.5$ . The drop labels 1 and 2 are for the impacting and sessile drops, respectively.  $\tilde{t}$  is the non-dimensionalized time used for the numerical simulations and is given by  $\tilde{t} = t/\tau_{\rho\gamma}$  where  $\tau_{\rho\gamma} = \sqrt{(\rho R^3)/\gamma}$  is the inertio-capillary time scale. The absolute values of the normalized velocities vary between zero (white) and twice the inertio-capillary velocity,  $V_{\rho\gamma} = \sqrt{\gamma/(\rho R)}$  (dark blue).

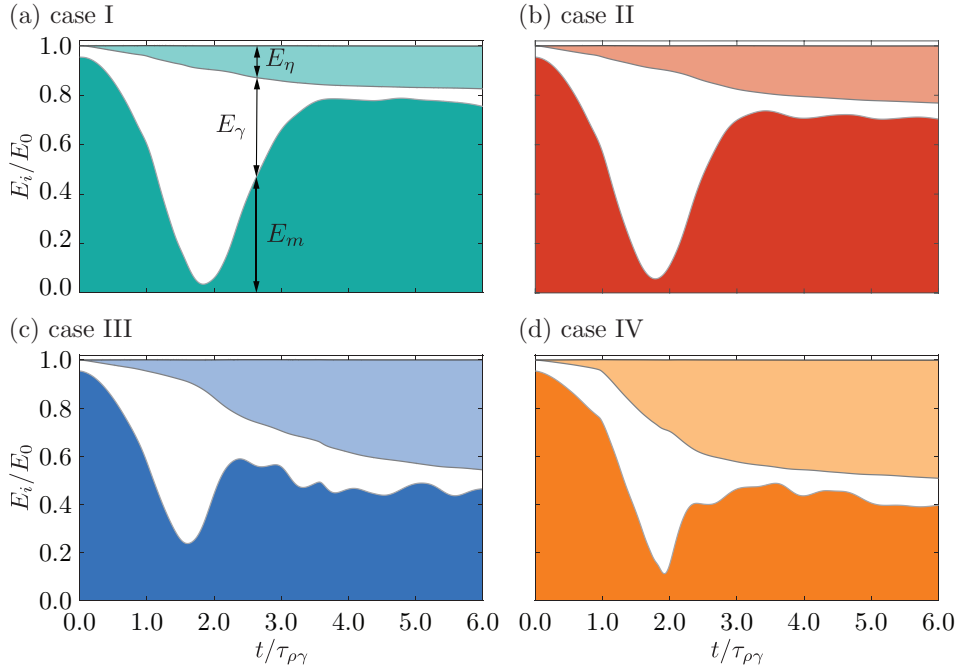


Figure 4.4.2: Energy budget: the temporal variation of energy transfer elucidates different stages of the drop-on-drop impact process at  $We = 1.5$ . Initially, all the energy is stored as the mechanical energy of the impacting drop and surface energy of the sessile drop ( $E_0$ ). Then, the mechanical energy of the system decreases, and is transferred into the surface energy of the drops. This transfer is followed by a recovery stage where surface energy is transferred back into the mechanical energy of the system. A part of the energy is lost as viscous dissipation. This viscous dissipation takes into account the combined energy dissipated both in the liquid drops and the surrounding air. This calculation includes the air-layers between the drops, and between the drops and the superamphiphobic substrate. (a) Case I:  $\chi = 0$ , (b) Case II:  $\chi = 0.08$ , (c) Case III:  $\chi = 0.25$ , and (d) Case IV:  $\chi = 0.625$ .  $E_m$  is the total mechanical energy of the system ( $E_m = E_k + E_g$ ),  $E_\gamma$  the surface energy of the two drops, and  $E_\eta$  the viscous dissipation in the system. Note that the total mechanical energy ( $E_m$ ) includes the energy of center of mass of the drops ( $E_m^{\text{CM}} = E_k^{\text{CM}} + E_g^{\text{CM}}$ ), where  $E_g^{\text{CM}}$  is the gravitational potential energy as well as the oscillation and rotational energies obtained in the reference frame that is translating with the center of mass of the individual drops.

of the sessile drop. To describe the system energy of the DNS results presented in figure 4.4.1, we plot the complete energy budget for each case in figure 4.4.2. For convenience of comparison, the energies in figure 4.4.2 are normalized with the initial energy of the system.

Let us consider first a head-on collision where  $\chi = 0$  (figure 4.4.1a, figure 4.4.2a, and supplementary videos 2–3, Case I), which is defined by a symmetric configuration. First, the momentum is transferred from the impacting drop to the sessile drop, as the sessile drop deforms. This transfer results in deceleration of the impacting drop. Moreover, the kinetic energy of the impacting drop transforms into the surface energy of the system. This transfer continues until  $\tilde{t} = 1.84$  (Fig. 4a: Column B) when the deformation in the two drops is maximum. Even at the moment of maximal deformation of both drops, the kinetic energy remains finite because of rotational flow within the drops (figure 4.4.1a: column B, velocity field) [? ]. The mechanical energy passes a minimum ( $\tilde{t} = 1.84$ ) when the surface energy is maximal. For  $\tilde{t} > 1.84$ , the surface energy of the two drops is converted back into kinetic energy. Retraction of the sessile drop is hindered by the impacting one (figure 4.4.1a: column C), directly sitting on top of it. As a result, the sessile drop cannot lift-off from the substrate, but it releases any extra energy by oscillations (supplementary videos 1–2). During impact, the drops lose approximately 20% of their initial energy through viscous dissipation (figure 4.4.2a). This dissipation occurs mainly during the initial stages of the process ( $\tilde{t} < 3$ ). It should be noted that the surface tension coefficient ( $\gamma$ ), viscosity ( $\eta$ ), and impact velocity ( $V$ ) all affect viscous dissipation (see chapter 2). These properties are related to the Ohnesorge number ( $Oh = \eta/\sqrt{\rho_l \gamma R} \approx 0.03$ ), which is the ratio of the inertio-capillary to inertio-viscous timescales, and the Weber number,  $We = \rho_l V^2 R / \gamma \sim \mathcal{O}(1)$  (see equation (4.15) and [? ? ]). The dissipation observed in our case is lower than that reported previously for a single drop impact at comparable  $Oh$  and  $We$  on non-wetting rigid substrates (see chapter 2). In the case of a single drop impact, the velocity of the drop goes to zero quickly as it approaches a rigid substrate [? ], leading to high dissipation close to the substrate. In the case of drop-on-drop impact, the sessile drop is deformable, decreasing the deceleration experienced by the impacting drop. As a result, the system retains almost 80% of its initial energy in the form of mechanical and surface energy of the drops.

For slightly off-center collisions, where  $\chi = 0.08$  (figure 4.4.1b, figure 4.4.2b, and supplementary videos 5–6, Case II), the initial collision is similar to Case I: the drops collide, followed by vertical compression and lateral spreading.

However, unlike Case I, the impacting and the sessile drops lift-off from the substrate. This feature results from the loss of axial symmetry of the velocity field for  $\chi > 0$ . During retraction, transfer of momentum from the compressed sessile drop back to the impacting drop occurs mainly along a vector pointing normal to the apparent contact zone. Moreover, the sessile drop attempts to regain its spherical shape (minimum surface energy state). As a result, the velocity field of the sessile drop is almost parallel to the contact zone, i.e., pointing to the upper left. These opposing orientations of the velocity fields cause the impacting drop to bounce off the sessile drop, and the sessile drop to lift-off from the substrate (see the velocity vector fields in figure 4.4.1b and supplementary video 6). Viscous dissipation increases as compared to a head-on-collision, but still is maximum during the initial stages of the process owing to the dissipation in the viscous boundary layer as the impacting drop slides over the sessile one ( $\tilde{t} < 3.5$ , figure 4.4.2b).

As the offset is further increased to  $\chi = 0.25$  (figure 4.4.1c, figure 4.4.2c, and supplementary videos 8–9, Case III), the impacting drop glides over the sessile drop (facilitated by the thin air layer), and sufficient energy is transferred to lift the sessile drop from the substrate. This can be understood from the interplay of the velocity field and the contact time (figure 4.4.1c and supplementary video 9). The relatively large offset from head-on alignment causes the averaged velocity field of the restoring impacting drop to point downwards, while the velocity field of the sessile drop is pointing upwards. The large deformations of both drops are reflected in the evolution of the surface energy (figure 4.4.2c). These large deformations also cause an increase in the viscous dissipation ( $E_\eta$ ): at the end of the process, almost 50% of the initial energy is lost.

Finally, if the offset from head-on alignment is increased even more to  $\chi = 0.625$  (figure 4.4.1d, figure 4.4.2d, and supplementary videos 11–12, Case IV), the time of contact is insufficient to transfer enough energy to the sessile drop for lift-off [? ]. Moreover, the vector normal to the drop-drop contact area is farthest from vertical as compared to the normal vectors in other cases. That is, it points nearly horizontal. As a result, the sessile drop rolls along the substrate and the impacting drop instead rebounds from the surface, resembling typical drop-surface impact. In this case, most of the energy is retained by the impacting drop, as illustrated in Fig. 5d. Similar to Case III, viscous dissipation accounts for almost 50% of the initial total energy. Although in Case I and IV the impacting drop rebounds while the sessile drop remains on the surface, we discriminate between both cases. For Case I, the vector

fields are symmetric around the  $X = Y = 0$  axis, whereas for Case IV the vector fields are highly asymmetric and the sessile drop rolls along the surface. Furthermore, in Case IV, the impacting drop bounces-off the substrate, as opposed to the sessile drop in Case I.

These results indicate that the DNS provide a quantitative description of the impact dynamics. At this point, we investigate whether there is a one-to-one match of the experimental data and numerical simulations; this is done by comparing the drop boundaries and experimentally-determined mechanical energies with the numerical predictions. Since we cannot exactly predict the impact parameter experimentally beforehand, we choose the control parameters for the numerical simulations by first analyzing the experimental data. Notably, we achieve a nearly quantitative agreement of the drop boundaries and experimental mechanical energies (figure 4.4.3). The different snapshots in figure 4.4.3(i-iv) refer to the following time steps: (i) at the instant of collision, (ii) sessile drop at maximum compression, (iii) droplet shape just before separation, and (iv) final outcome of the impact. We expect that slight deviations between the experimental and numerically determined drop boundaries result from marginal inaccuracies in the experimental determination of the off-set parameter. However, the agreement is remarkably good, keeping in mind that there are no fitting parameters.

In figure 4.4.3(a-v) and 4.4.3(b-v), we compare the measured experimental mechanical energies (data points) with those calculated using simulations (dotted lines). The calculated mechanical energies exceed the experimentally determined energies. To understand the origin of this discrepancy, one needs to consider that experimentally, we are only able to measure the vertical and horizontal displacements to approximate the mechanical energy of each drop. The images analysis did not offer an easy route to quantify the contribution of the rotational and oscillation energies that are included in the numerically calculated mechanical energy,  $E_m$ . Therefore, to test whether neglecting the rotational and oscillation energies in our experiments causes the discrepancy, we calculated the center of mass mechanical energies ( $E_m^{\text{CM}}$ ) for the two drops numerically (figure 4.4.3a-v and 4.4.3b-v, see § 4.D for details of calculation). The zero of the potential energy ( $E_g^{\text{CM}} = 0$ ) refers to the center of mass of the sessile drop at  $t = 0$ . This implies that  $E_g^{\text{CM}}$  of the sessile drop becomes negative during compression. The center of mass kinetic energy ( $E_k^{\text{CM}}$ ) is added to this value to get  $E_m^{\text{CM}}$ , i.e.,  $E_m^{\text{CM}} = E_k^{\text{CM}} + E_g^{\text{CM}}$ . As illustrated in figure 4.4.3(a-v) and 4.4.3(b-v), the numerical results (solid lines) now nearly overlay the experimental results (data points). This holds for both the tem-

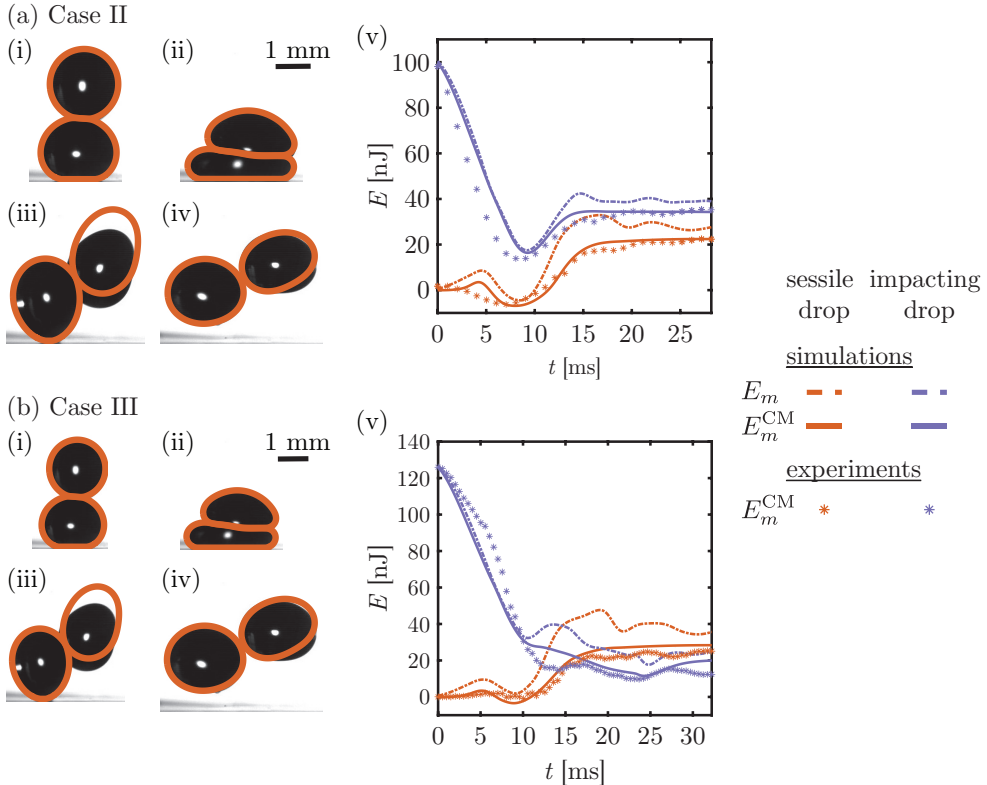


Figure 4.4.3: Validation of the numerical code: (a) Case II: both sessile and impacting drop lift-off ( $We = 1, \chi \approx 0.08$ ) for  $t =$  (i) 0 ms, (ii) 8 ms, (iii) 20 ms, (iv) 24 ms, and (b) Case III: sessile drop lifts-off and impacting drop rolls on the substrate ( $We = 1, \chi \approx 0.25$ ) for  $t =$  (i) 0 ms, (ii) 8 ms, (iii) 20 ms, (iv) 24 ms. In the subfigures (i) to (iv), overlay of experimental images and DNS results (orange contour) are shown. (v) The mechanical energy of the center of mass ( $E_m^{\text{CM}}$ ) calculated from experiments and simulations match within the experimental error. Note that in experiments, we could only keep track of the motion of the center of mass whereas in numerical simulations, the entire velocity field is known. Using this information, we can calculate the overall energy budgets. Here, the total mechanical energy of the drops ( $E_m$ ) is shown in solid lines for reference. Error estimated in the experimental data is approximately 20% of the total energy.

poral development of the energy for the sessile drop as well as the impacting drop. Supposedly, the small discrepancies may arise from finite adhesion of the sessile drop to the substrate in the experiments (which is not accounted for in the simulations). An additional source of error may arise from the selection of time  $t = 0$ . We choose  $t = 0$  based on the time instant when the sessile drop starts to feel the presence of the velocity field of the impacting drop, i.e., when the kinetic energy of the center of mass of the sessile drop becomes non-zero. Nevertheless, the remarkable agreement between the experimental and numerical results for the center of mass mechanical energies illustrate that the DNS are able to describe the oil drop-on-drop impact physics accurately. This allows for quantifying the contribution of the rotational and oscillatory energies. As future work, one can also estimate these contributions from experimentally obtained boundaries of the drops by employing the method described in [?].

## 4.5 Conclusions and outlook

By combining systematic experiments with numerical simulations, we illustrate how to predict and control the outcome of binary oil drop impacts on low adhesion surfaces. Four non-coalescing outcomes are attainable by varying the Weber number  $We$  and the offset from head-on alignment of the impacting drops  $\chi$ . One-to-one comparisons between the experimentally and numerically determined drop boundaries and center of mass mechanical energies illustrate the power of the direct numerical simulations for quantitatively predicting the dynamics of drop-on-drop impact. More specifically, our numerical simulations illustrate that these general outcomes are governed by the average direction of the flow velocity vectors during the retraction phase, which are associated with  $We$  and  $\chi$ . In addition, our results indicate that the ability to remove a sessile oil drop from the surface, as in Cases II and III, first requires sufficient energy transfer from the impacting drop and subsequently requires contrasting velocity vector directions of the two retracting drops. Interestingly, our results illustrate that different outcomes exist even when the total dissipative losses of the system are similar, i.e., the alignment of impact alone can be used to determine the recovered energy distribution between the two drops after impact.

## Acknowledgments

We would like to thank Hans-Jürgen Butt for fruitful discussions, Andrea Prospertti for insightful discussions on numerical simulations at different stages of the project, Pierre Chantelot for discussion on energy dissipation in single drop impact phenomenon, and Uddalok Sen for proof-reading this chapter. We would also like to thank Michael Kappl for help with the estimation of forces on the substrate, and Abhishek Khadiya for support with initial measurements.

# Appendix

## 4.A Contact angle measurements

A drop of hexadecane (figure 4.2.1a-ii) exhibits an apparent contact static angle of  $\Theta^{\text{app}} = 164^\circ \pm 1^\circ$ , an apparent receding contact angle of  $\Theta_r^{\text{app}} = 158^\circ \pm 3^\circ$ , and an apparent advancing contact angle  $\Theta_a^{\text{app}} \approx 180^\circ$  [? ], as determined by confocal microscopy (figure 4.2.1a-iii and 4.A.1). Low lateral adhesion of hexadecane is confirmed by measuring a low roll-off angle of  $3^\circ \pm 2^\circ$  [? ? ]. Roll-off angles measurements were performed using a goniometer OCA 35 for hexadecane drops of 5  $\mu\text{L}$ . The apparent contact angle was measured with a Leica TCS SP8 confocal microscope, equipped with an HCX PL APO 40x/0.85 dry objective, for a hexadecane drop of 10  $\mu\text{L}$ . The advancing and receding angles were measured while moving the hexadecane drop with a needle. The needle was supported on a micrometer stage next to the confocal microscope. All angles were measured at least three times and the results are shown in figure 4.A.1.

## 4.B Water-on-water drop impact

For comparison, we also performed head-on and off-center collisions for water drops of a similar diameter than for oil drops. To test the generality of our experiments, we used superamphiphobic textiles instead of soot templated surfaces. Superamphiphobic textiles show slightly worse wetting properties than soot template surfaces. This is reflected in higher roll-off angles. The roll-off angle of water with the surface varied between  $13^\circ - 20^\circ$  for the textile surfaces while the roll-off angles varied between  $2^\circ - 5^\circ$  on the soot-templated glass. On the other hand, the Cassie-to-Wenzel transition is less likely for water drops than for oil drops. When varying the Weber number  $We$  and the impact parameter  $\chi$ , the same six outcomes could be observed, same as the

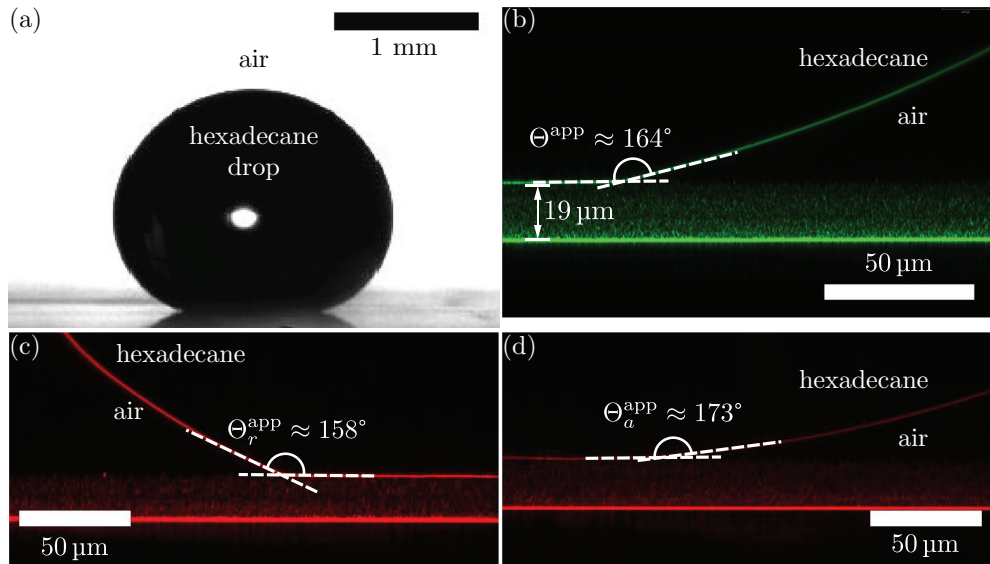


Figure 4.A.1: Sessile oil drop on a superamphiphobic substrate: (a) shadowgraph and (b-d) confocal images of a hexadecane drop on soot-templated glass slide. The shadowgraph image shows the typical shape of a sessile hexadecane drop during the experiments. The corresponding volumetric radius is 0.9 mm. The confocal microscopy image illustrates the apparent contact angle of the drop with the surface. The image was taken in reflection mode to allow measuring the contact angle with highest possible accuracy. The measured roll-off angle of a drop of 5  $\mu\text{L}$  is 3.2° (measured with a goniometer). The apparent contact angle  $\Theta^{\text{app}} \approx 164^\circ$ , the receding angle  $\Theta_r^{\text{app}} \approx 158^\circ$ , and the advancing angle  $\Theta_a^{\text{app}} \approx 173^\circ$ , were measured with a drop of 10  $\mu\text{L}$  volume. Ideally,  $\Theta_a^{\text{app}}$  should be 180°. The difference could be attributed to the limited optical contrast.

cases with hexadecane drops (figure 4.B.1)

## 4.C Simulation methodology

We use a finite volume method based partial differential equation solver, Basilisk C [? ] for numerical simulation of incompressible Navier-Stokes equations,

$$\nabla \cdot \mathbf{v} = 0, \quad (4.2)$$

$$\frac{\partial \tilde{\mathbf{v}}}{\partial \tilde{t}} + (\tilde{\mathbf{v}} \cdot \tilde{\nabla}) \tilde{\mathbf{v}} = \frac{1}{\tilde{\rho}} \left( -\tilde{\nabla} \tilde{p} + Oh \tilde{\nabla} \cdot (2\tilde{\eta} \tilde{\mathcal{D}}) + \tilde{\kappa} \tilde{\delta}_s \hat{\mathbf{n}} \right) - Bo \hat{\mathbf{Z}}, \quad (4.3)$$

where the velocity  $\mathbf{v}$  and pressure  $p$  fields are non-dimensionalized using the inertio-capillary velocity ( $V_{\rho\gamma} = \sqrt{\gamma / (\rho_l R)}$ ) and capillary pressure ( $P_\gamma = \gamma / R$ ), respectively. All length scales are normalized using the radius of the impacting drop ( $R$ ). In equation (4.3),  $\mathcal{D}$  is the deformation tensor (i.e., the symmetric part of the velocity gradient tensor,  $\tilde{\nabla} \tilde{\mathbf{v}}$ ) and  $\tilde{\kappa} \tilde{\delta}_s \hat{\mathbf{n}}$  represent the singular ( $\delta_s = 1$  at the interfaces and 0 otherwise) surface tension force, where  $\kappa$  and  $\hat{\mathbf{n}}$  are the interfacial curvature and normal, respectively. Since we do not vary the type of liquid during and the volume of drops in our experiments or simulations, Ohnesorge number ( $Oh = \eta_l / \sqrt{\rho_l \gamma R} = 0.0216$ ) and Bond number ( $Bo = \rho_l g R^2 / \gamma = 0.308$ ) remain constant. Lastly, in the simulations, the impact velocity is characterized by the impact Weber number ( $V = \sqrt{We}$ ).

We use the geometric volume of fluid (VoF) [? ? ] method for interface tracking. Consequently, one-fluid approximation [? ? ] is used in the solution of the Navier-Stokes momentum equation (equation (4.3)).

To impose the condition of non-coalescence of the drops, same as chapter 3, different VoF tracers are used for the two droplets (equation 4.4). The use of two different tracers, along with interface reconstruction, ensures that there is always a thin air layer (thickness  $\sim \Delta_1$ , where  $\Delta_1 = R/256$  is the size of smallest grid cell in the simulation domain). Additionally, in order to model the superamphiphobic substrate, it is assumed that there is a thin air layer (thickness  $\sim \Delta_2$ , where  $\Delta_2 = R/512$  is the smallest grid cell near the substrate) between the drops and the substrate. All other boundaries are assumed to have no flow and free slip condition. We ensure convergence by comparing the viscous dissipation of the system and have chosen  $\Delta$  such that the difference between consecutive simulations is small. The properties,

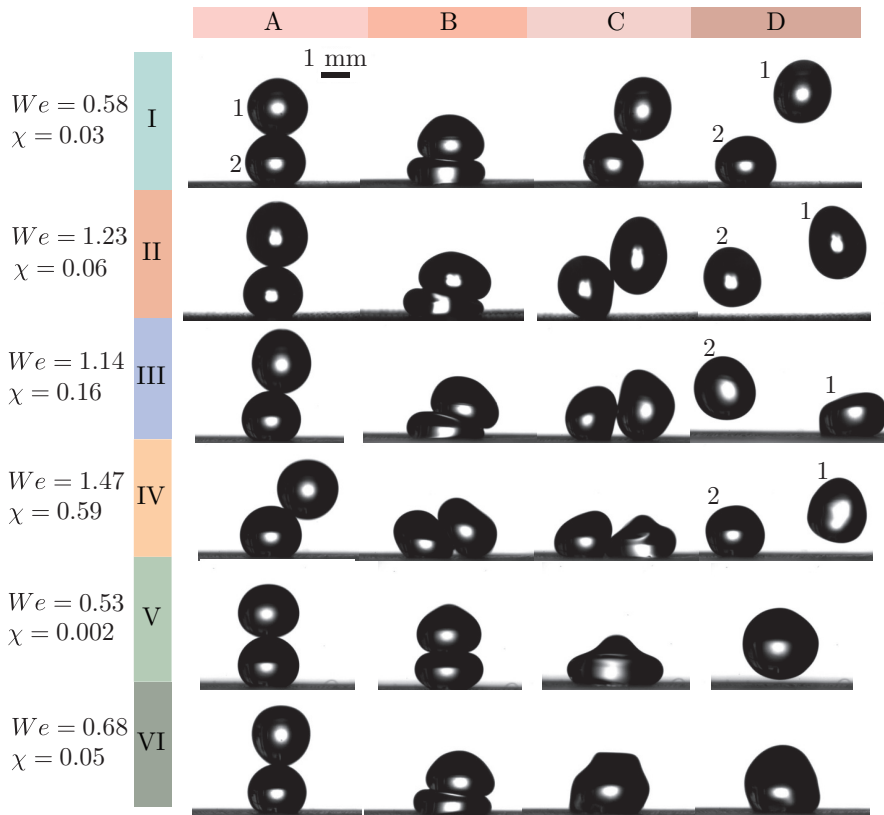


Figure 4.B.1: Snapshots of the impact dynamics of water drops: note that the drop labels 1 and 2 are for the impacting and sessile drop, respectively. Six outcomes (Cases I – VI) are observed when varying the impact parameter  $\chi$  and the Weber number  $We$  independently. The rows correspond to different impact parameter for I-VI. The columns show characteristic stages of the collision process. A: just at collision, B: sessile drop at maximum compression, C: droplet shape just before separation or coalescence. D: final outcome of the impact. Volume of both drops is 8  $\mu\text{L}$ . Case I,  $We = 0.58$  and  $\chi = 0.03$ : the time stamp for each frame is:  $t_A = 0 \text{ ms}$ ,  $t_B = 10.5 \text{ ms}$ ,  $t_C = 23 \text{ ms}$ ,  $t_D = 36 \text{ ms}$ . Case II,  $We = 1.23$ ,  $\chi = 0.06$ :  $t_A = 0 \text{ ms}$ ,  $t_B = 10.5 \text{ ms}$ ,  $t_C = 19 \text{ ms}$ ,  $t_D = 30.5 \text{ ms}$ . Case III,  $We = 1.14$ ,  $\chi = 0.16$ :  $t_A = 0 \text{ ms}$ ,  $t_B = 9 \text{ ms}$ ,  $t_C = 15 \text{ ms}$ ,  $t_D = 30 \text{ ms}$ . Case IV,  $We = 1.47$ ,  $\chi = 0.59$ :  $t_A = 0 \text{ ms}$ ,  $t_B = 5.5 \text{ ms}$ ,  $t_C = 9 \text{ ms}$ ,  $t_D = 24 \text{ ms}$ . Case V,  $We = 0.53$ ,  $\chi = 0.002$ :  $t_A = 0 \text{ ms}$ ,  $t_B = 4 \text{ ms}$ ,  $t_C = 14.5 \text{ ms}$ ,  $t_D = 36 \text{ ms}$ . Case VI,  $We = 0.68$ ,  $\chi = 0.05$ :  $t_A = 0 \text{ ms}$ ,  $t_B = 10 \text{ ms}$ ,  $t_C = 12.5 \text{ ms}$ ,  $t_D = 21 \text{ ms}$ .

such as density and viscosity are calculated using the VoF arithmetic property equations (equation 4.5, where  $A_{gl}$  is the ratio of properties of gas and liquid).

$$\left( \frac{\partial}{\partial t} + \mathbf{v} \cdot \nabla \right) \{ \Psi_1, \Psi_2 \} = 0, \quad (4.4)$$

$$\tilde{A} = A_{gl} + (1 - A_{gl}) (\Psi_1 + \Psi_2) \quad \forall A \in [\rho, \eta], \quad (4.5)$$

## 4.D Energy budget calculations

In this section, we discuss the different equations that we have used to calculate different energies non-dimensionalized by the capillary energy scale  $\tilde{E}_i = E_i / (\gamma R^2)$ . First, we discuss the calculation of energies of the center of mass of the drops ( $\tilde{E}_m^{\text{CM}}$ ),

$$\tilde{E}_m^{\text{CM}} = \tilde{E}_k^{\text{CM}} + \tilde{E}_g^{\text{CM}}, \quad (4.6)$$

where  $\tilde{E}_k^{\text{CM}}$  and  $\tilde{E}_g^{\text{CM}}$  are the center of mass kinetic energy and potential energy respectively. For these calculations, we first need to find the magnitude of velocity and position of the center of mass for each drop,

$$\tilde{\mathbf{v}}^{\text{CM}} = \frac{\int_{\tilde{\Omega}} \tilde{\mathbf{v}} d\tilde{\Omega}}{\tilde{\Omega}}, \quad (4.7)$$

$$\tilde{Z}^{\text{CM}} = \frac{\int_{\tilde{\Omega}} \tilde{Z} d\tilde{\Omega}}{\tilde{\Omega}} \quad (4.8)$$

where,  $d\Omega$  is the differential fluid volume. Further,  $E_k^{\text{CM}}$  and  $E_g^{\text{CM}}$  can be calculated,

$$\tilde{E}_k^{\text{CM}} = \frac{2}{3} \pi (\tilde{\mathbf{v}}^{\text{CM}} \cdot \tilde{\mathbf{v}}^{\text{CM}}), \quad (4.9)$$

$$\tilde{E}_g^{\text{CM}} = Bo \tilde{Z}^{\text{CM}}. \quad (4.10)$$

The overall energy budget consists of the total mechanical energy  $\tilde{E}_m = \tilde{E}_k + \tilde{E}_g$ , the surface energy  $\tilde{E}_\gamma$ , and the energy dissipation  $\tilde{E}_\eta$ , calculated as follows:

$$\tilde{E}_k = \int_{\tilde{\Omega}} \frac{1}{2} \tilde{\rho} (\tilde{\mathbf{v}} \cdot \tilde{\mathbf{v}}) d\tilde{\Omega}, \quad (4.11)$$

$$\tilde{E}_g = Bo \int_{\tilde{\Omega}} \tilde{\rho} \tilde{Z} d\tilde{\Omega}, \quad (4.12)$$

$$\tilde{E}_\gamma = \int_{\tilde{\mathcal{A}}} d\tilde{\mathcal{A}}, \quad (4.13)$$

$$\tilde{E}_\eta = \int_0^{\tilde{t}} \tilde{\xi}_\eta d\tilde{t} \quad (4.14)$$

In equations (4.11) and (4.12), energies of both the drops as well as the surrounding air medium are considered. Noticing that the density ratio of air to liquid,  $\rho_{gl} = 1/770 \ll 1$  and that the domain is fixed in volume, the change in gravitational potential energy of the air medium is negligible. This implies that  $E_g = E_g^{\text{CM}}$ . The contributions from the surrounding air to  $E_k$  and  $E_\eta$  are also very small but we include them here for completeness. In equation 4.13,  $d\mathcal{A}$  represents a differential surface. Lastly, equation 4.14 gives the total viscous dissipation in the system. In this equation,  $\xi_\eta$  denotes the viscous dissipation function given by

$$\tilde{E}_\eta = Oh \int_{\tilde{\Omega}} 2\tilde{\eta} (\tilde{\mathcal{D}} : \tilde{\mathcal{D}}) d\tilde{\Omega}. \quad (4.15)$$

## 4.E Code availability

All codes used in this chapter are permanently available at [? \].](#)

4

## 4.F Supplemental movies

These supplemental movies are available at [? \].](#)

SM1: ( $We \approx 1.30$  &  $\chi \approx 0.01$ ) Experimental video of Case I for hexadecane drops: bouncing of impacting drop.

SM2: ( $We = 1.50$  &  $\chi = 0$ ) Simulation video of Case I for hexadecane drops: bouncing of impacting drop.

- SM3: ( $We = 1.50 \& \chi = 0$ ) Simulation video showing velocity vectors of Case I for hexadecane drops: bouncing of impacting drop. The two-dimensional contour represents the slice  $Y = 0$ . Time is normalized by the capillary time scale,  $\tau_{\rho\gamma} = \sqrt{(\rho_l R_0^3) / \gamma}$ .
- SM4: ( $We \approx 1.53 \& \chi \approx 0.08$ ) Experimental video of Case II for hexadecane drops: bouncing of the impacting drop followed by lift-off of the sessile drop.
- SM5: ( $We = 1.50 \& \chi = 0.08$ ) Simulation video of Case II for hexadecane drops: bouncing of the impacting drop followed by lift-off of the sessile drop.
- SM6: ( $We = 1.50 \& \chi = 0.08$ ) Simulation video showing velocity vectors of Case II for hexadecane drops: bouncing of the impacting drop followed by lift-off of the sessile drop. The two-dimensional contour represents the slice  $Y = 0$ . Time is normalized by the capillary time scale,  $\tau_{\rho\gamma} = \sqrt{(\rho_l R_0^3) / \gamma}$ .
- SM7: ( $We = 1.50 \& \chi = 0.08$ ) Experimental video of Case III for hexadecane drops: sliding-off of the impacting drop on top of the sessile drop followed by lift-off of the sessile drop.
- SM8: ( $We = 1.50 \& \chi = 0.25$ ) Simulation video of Case III for hexadecane drops: sliding-off of the impacting drop on top of the sessile drop followed by lift-off of the sessile drop.
- SM9: ( $We = 1.50 \& \chi = 0.25$ ) Simulation video showing velocity vectors of Case III for hexadecane drops: sliding-off of the impacting drop on top of the sessile drop followed by lift-off of the sessile drop. The two-dimensional contour represents the slice  $Y = 0$ . Time is normalized by the capillary time scale,  $V_{\rho\gamma} = \sqrt{(\rho_l R_0^3) / \gamma}$ .
- SM10: ( $We = 1.50 \& \chi = 0.25$ ) Experimental video of Case IV for hexadecane drops: sliding-off of the impacting drop on top of the sessile drop followed by its lift-off. In this case, the sessile drop stays on the substrate .
- SM11: ( $We \approx 1.50 \& \chi \approx 0.625$ ) Simulation video of Case IV for hexadecane drops: sliding-off of the impacting drop on top of the sessile drop followed by its lift-off. In this case, the sessile drop stays on the substrate.

chapter 4: lifting a sessile oil drop with an impacting one



source code



supplemental movies

- SM12: ( $We \approx 1.50$  &  $\chi \approx 0.625$ ) Simulation video showing velocity vectors of Case IV for hexadecane drops: sliding-off of the impacting drop on top of the sessile drop followed by its lift-off. In this case, the sessile drop stays on the substrate. The two-dimensional contour represents the slice  $Y = 0$ . Time is normalized by the capillary time scale,  $\tau_{\rho\gamma} = \sqrt{(\rho_l R_0^3) / \gamma}$ .
- SM13: ( $We \approx 5.84$  &  $\chi \approx 0.08$ ) Experimental video of Case V for hexadecane drops: coalescence of drops and lift-off of coalesced drop.
- SM14: ( $We \approx 1.43$  &  $\chi \approx 0.03$ ) Experimental video of Case VI for hexadecane drops: coalescence of drops and coalesced drop remains on the substrate.